V/f Controlled Low Frequency High Voltage ac Transmission for the Grid Integration of Offshore Wind

by

Okechukwu C. Efobi

A thesis submitted to the Faculty of Graduate Studies of

The University of Manitoba

in partial fulfillment of the requirements for the degree of

Doctor of Philosophy

Department of Electrical and Computer Engineering

Faculty of Engineering

University of Manitoba

Winnipeg, Canada

Abstract

Low frequency high voltage alternating current (LF-HVac) transmission has been proposed as a bulk power transfer alternative to either the conventional 50/60 Hz HVac or the high voltage direct current (HVdc) transmission schemes. In LF-HVac transmission, the proposition is to use ac operating frequency values that would be fractional quantities of the nominal 50/60 Hz frequency used in the conventional HVac. In comparison to HVac, LF-HVac would considerably increase the power transfer capacity of a given transmission link, extend the power transmission distance (without compensation), reduce losses, and improve the voltage and the dynamic stability of the power transmission system. Grid integration of remote offshore wind farms has been identified as the most viable application of the LF-HVac transmission scheme. Unlike HVdc, it would only require one converter station, which would be conveniently sited onshore.

Wind, unlike conventional electricity sources such as hydro or thermal, is an intermittent and non-dispatchable energy resource. Thus, it would be logical that any power transmission scheme applied to a remote offshore wind facility is practical for the expected variability of its output. This thesis proposes and investigates the feasibility and the merits of V/f controlled LF-HVac transmission scheme for offshore wind. In submarine export cables, it was determined that voltage V is a more consequential quantity than frequency f in limiting the amount of useful power that could be delivered to the grid. With a defined V/f ratio, simultaneous adjustment of system V and f would allow for non-saturation operation of power transformers and reactors. The LF-HVac system would operate at the optimally selected V/f set for the rated output power.

However, for most of the times, when the wind output is below the rated power, the system would operate at the energy-output-level applicable, lower, V/f set, thereby maximizing energy delivery to the grid for that wind output level.

Investigations into the electrical characteristics and performance of high voltage cross-linked polyethylene (XLPE) export cables, with respect to the ac operating frequency, underscore the advantages of adopting LF-HVac in lieu of the conventional HVac. The results show that at lower nominal operating frequency, a given cable system would support greater current/power capacity while losses, per energy transferred, are reduced. With the developed frequency-dependent steady-state LF-HVac transmission model, analysis of the voltage, current, and power flow in the export cable show that for an intermittent energy resource like wind, the optimum operating V/f pair would be variable, dependent on the prevailing wind conditions and thus, the energy output.

Finally, the feasibility and the technical requirements of applying modular multilevel converter (MMC) technology in the frequency conversion of the V/f controlled LF-HVac transmission scheme is investigated. The results support the adoption of MMC as the frequency converter. Nevertheless, it is important to appropriately determine the energy storage requirement, i.e., the minimum capacitor sizing, of the MMC at each operating point, and for the applicable V/f pair. Failure to do so could result in dc overvoltage. Results from the detailed time domain simulations of the V/f controlled LF-HVac transmission system for offshore wind in PSCAD/EMTDC provide validation to the thesis theory and the analytically derived results of the offshore wind system.

Acknowledgements

I am especially grateful to Prof. Ani Gole, my advisor, for the PhD study opportunity with him. His support and patience throughout this protracted journey are immensely appreciated. I would also like to thank my advisory committee members, Prof. Shaahin Filizadeh and Prof. Pooneh Maghoul, for their periodic progress reviews and insightful feedback on my research.

In a special way, I extend my profound gratitude to Dr. Wei Li for the innumerable technical discussions, teachings and support during my research. In the same vein, I thank Dr. Mukesh Das for his technical support and guidance in my PhD work.

Of course, this story would not have been complete without the support of and collaboration with the administrative and technical staff of the Department of Electrical and Computer Engineering, my fellow graduate students, and postdoctoral researchers whom I have met and interacted with during my PhD study. I am grateful for all your suggestions and help!

Table of Contents

List of Figures

List of Tables

Chapter 1

Introduction

1.1. Background

High voltage alternating current (HVac) and high voltage direct current (HVdc) are well-established technologies used in bulk power transfer. Around the world, HVac dominates regional, national, and international energy grids. In North America, the mains electricity operates at 60 Hz nominal frequency while 50 Hz is the standard ac operating frequency in most countries on the other continents [1]. It is interesting to note that prior to 1891/92, there was no single ac operating frequency widely adopted by the nascent electric utility industry in North America [2], [3]. Frequencies ranged from $16\frac{2}{3}$ to $133\frac{1}{3}$ cycles per second. However, given the considerable growth in ac transmission and distribution networks, the need for interconnections became apparent. Thus, over several years, and by consensus, the industry moved towards the adoption of 60 Hz as the standard ac operating frequency in North America.

The story of how alternating current (ac) became dominant over direct current (dc) in the electric utility industry cannot be told without recognizing the impact the development of ac transformers had in ending the aptly named "war of the currents" [4]. Consider a basic point-to-point power transmission line with no transformers, as shown in Fig. 1-1. The apparent power S at the load distribution point is given by (1-1), where V is the voltage at the load distribution point and I is the transmission current. The line impedance Z is the sum of its resistance R and its inductive reactance $j\omega L$, i.e., $Z = R + j\omega L$, where ω is the ac angular frequency and L is the

line inductance. Note that some power losses, associated with the resistance of the transmission medium to current flow, is encountered during power transfer. This is given by (1-2).

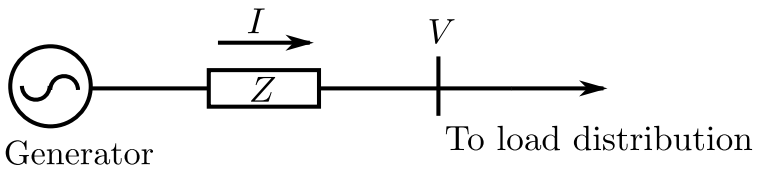

Fig. 1-1: Single line diagram of a point-to-point power transmission scheme.

$$S = VI \tag{1-1}$$

$$P_{loss} = I^2 R \tag{1-2}$$

Given that generator construction constraints put a cap on the voltage level at which it can be operated [5], (1-1) indicates that the only way to increase power supply from the generator to the load point in the system of Fig. 1-1 is by increasing I. However, as (1-2) shows, doing so would in turn lead to even higher power losses. Therefore, utility operators at the time had no choice but to favour either dc or ac, depending on their underlying motivations and/or affiliations [2], [3].

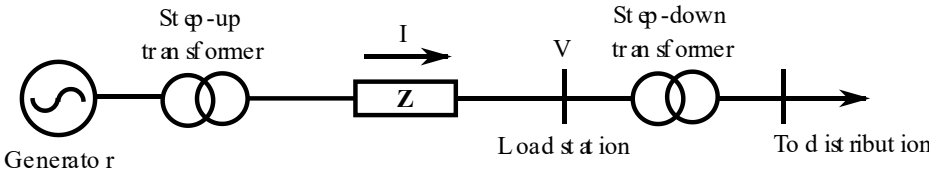

Fig. 1-2: Single line diagram of a point-to-point ac transmission scheme, with step-up and step-down transformers.

However, unlike dc characteristics, the inherent sinusoidal variation of ac quantities with time is integral in the operation of an ac transformer. This device conveniently allowed for step-up or step-down of ac voltage levels. Thus, the ac system represented in Fig. 1-1 could then be

reconfigured to Fig. 1-2 representation. This was a game changer, and it meant that, referring to (1-1), more ac power could then be transmitted at higher voltage levels than was previously achievable, while keeping transmission current low. Thus, referring to (1-2), transmission losses were significantly curtailed for ac power transfer in comparison to equivalent dc power transfer. Consequently, ac transmission achieved economies of scale over dc transmission through coverage of longer transmission distances with cheaper wires/cables, including the attendant markedly reduced power losses [6], [7]. This is the story of how ac came to dominate the electric utility industry, even till date.

Notwithstanding the early and sustained success of ac in power transmission, it has some inherent technical limitations. Consider the circuit representation of a short ac transmission line, as shown in Fig. 1-3. Note that the inductive reactance, $X = 2\pi fL$, where f is the ac frequency, is often much greater than the line resistance R [8], [5], [9]. Thus, (1-3), the simplified power transfer equation, is used to determine the power transferred to the receiving end, P_R, where V_S is the sending end voltage, V_R is the receiving end voltage, and δ is the power angle, i.e., the angle by which V_S leads V_R [9]. Equation (1-3) indicates that P_R is inversely proportional to X. Thus, without reactive compensation, the magnitude of X, which is proportional to both f and the line length l ($X = xl$, where x is the series inductive reactance per unit length per phase), limits either the maximum amount of power that can be transferred and/or the transmission distance. Furthermore, as indicated in (1-3), the magnitude of transferred ac power is also influenced by the power angle.

$$P_R = \frac{|V_S||V_R|}{|X|}\sin\delta \tag{1-3}$$

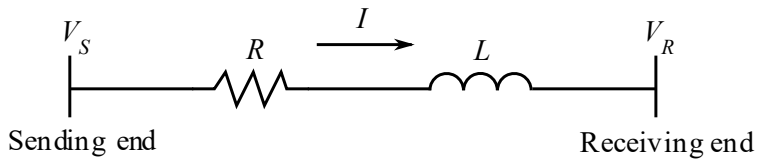

Fig. 1-3: Circuit representation of a short ac transmission line.

On the other hand, dc has a frequency of zero. So, theoretically there is no limit to the amount of power dc can transmit nor the transmission distance it can cover. (However, note that in practice ac generators are used to generate the transmitted power. Therefore, the characteristics of the converter and the impedance of the ac network do impose some limitation, after all). In addition, for two ac systems linked by a dc line, power angle is arbitrary and can be set to any value [10].

Therefore, with the tremendous progress made in the field of power electronics in recent decades, HVdc is now a robust bulk power transmission technology deployed to applications and scenarios where use of ac may be cost prohibitive or simply impractical [4]. It appears the war of the currents may not be over after all. For example, in transmission of large amounts of power over great distances ($\geq$ 600 km) via overhead lines, HVdc is often more cost competitive than HVac [5], [8]. As explained in the preceding paragraph, HVdc requires no reactive compensation of its lines, and even the converter stations costs are offset by the reduced construction costs of dc lines, in comparison to equivalent ac lines. Furthermore, the greatest limitation of HVac at the conventional 50/60 Hz is laid bare when power must be transmitted via underground or submarine cables. Charging current, given by (1-4), where C_{ab} is the capacitance of the line, and V_{ab} is the line voltage (assuming a single-phase circuit) [5], is the major limiting factor in the amount of active power conventional HVac could transfer via cables. Of course, shunt reactive compensation could be used to increase the power transfer capacity of ac cables. However, in most submarine situations this would be impractical or simply cost-prohibitive. Therefore, in the

absence of viable reactive compensation options between the terminals, HVac is usually limited to about 50-75 km for cable(s) interconnections [11], [12], [13], [14].

$$I_{chg} = j\omega C_{ab} V_{ab} \tag{1-4}$$

1.2. Problem Definition

Over the past two decades, wind power has burgeoned. From an installed capacity of 7.5 GW in 1997 to 733 GW in 2018, this translates to a ninety-eight-fold jump [15]. Presently, onshore wind has more installed capacity and investments than offshore wind [15], [16]. However, offshore wind presents immense potential, given that wind speeds are stronger and steadier out at sea [16], [17]. There is also the factor of likely less public opposition to remote offshore wind projects than to those sited onshore or close to the shore [18]. So, offshore wind energy demand is expected to enjoy rapid growth as countries move towards a net zero future [19]. Nevertheless, offshore wind projects are relatively expensive, and there are difficulties associated with their installation and maintenance [17]. So, research trends are toward reduction of their overall costs and in improving their capacity availability [18]. Note that any HVdc scheme used in grid integration of offshore wind must have a converter station sited offshore, close to the wind farm, in addition to the onshore converter (inverter) station. The harsh environment out at sea contributes a lot to the complexity, costs, both capital and recurrent, and the downtime of HVdc-connected remote offshore wind projects.

Consequently, Low Frequency High Voltage ac (LF-HVac) transmission has been proposed as a potential alternative to HVdc in the grid integration of remote offshore wind farms. Equations (1-3) and (1-4) have shown that power transmission limitations outlined for conventional HVac are frequency dependent. So, a direct method of reducing cable charging

current, which would in turn increase the real power transferability of ac-operated cables, is to reduce the frequency. In essence, LF-HVac aims to operate at a fraction of 50/60 Hz to improve ac power transfer capacity and/or the achievable transmission distance. Recall that the opening paragraph in the preceding section mentioned that ac transmission at frequencies below the conventional 50/60 Hz is not a modern concept. In fact, 25 Hz was the last contender to 60 Hz as the standard ac frequency in North America [2]. It was not until the late 1910s that advancements in manufacturing technologies enabled the performance of 60 Hz transmission lines to approach that of 25 Hz lines. So, electrical engineers have long known that ac operation at frequencies lower than conventional grid frequencies leads to lower line losses and better voltage regulation. However, modern power electronics and its adoption in flexible ac transmission systems (FACTS) and HVdc could revive the use of LF-HVac in today's power networks, albeit with a totally different frequency conversion technology.

Unlike HVdc-connected offshore wind power parks (OWPP), LF-HVac design topology for grid integration of OWPP would require only one converter station, which would be conveniently located onshore [20], [21], [22], [23], [24]. This feature means that LF-HVac has the potential of reducing the costs and difficulties associated with offshore wind installations. Presently, there is not an existing LF-HVac scheme for bulk power transfer. However, similar schemes, operating at $16\frac{2}{3}$ or 16.7 Hz, have been in use in some European railway networks for decades [20], [25]. However, these low frequency railway grids are mostly single-phase, in addition to having a mixture of rotary and static (power electronics-based) frequency converters at interfaces with the main electricity grids [25]. Given that the application of power electronics-based LF-HVac in grid integration of OWPP is still on the drawing board, it is essential that extensive supporting studies and research results be presented to convince power utilities to buy

into the program. Existing literature on the subject reveal that various design proposals, system studies, and technical considerations are being investigated by a growing number of researchers. The relevant studies will be reviewed in the subsequent chapter.

Nevertheless, more investigations are needed to improve the already proposed LF-HVac-based OWPP system designs and operational strategies. To realize the first practical LF-HVac transmission scheme for offshore wind, theoretical and feasible experimental studies must demonstrate that its technical and economic performance metrics are at least competitive to those of equivalent HVdc and conventional HVac schemes. So, proposed LF-HVac design and operational methods should explore solutions beyond what is obtainable in conventional HVac or HVdc schemes to improve LF-HVac competitiveness. For instance, most of the references already cited used either 20 Hz or 16.67 Hz as the frequency of the LF-HVac systems they studied. However, none or scanty information was provided to justify the choice of that nominal frequency value. Furthermore, given that the proposed LF-HVac-based OWPP scheme would incorporate power converters as part of the system, unlike traditional HVac, designing LF-HVac around a single nominal frequency may be limiting its capital and operational capabilities.

1.3. Motivation

In 2015, 196 parties adopted the Paris Agreement, which aims “to limit global warming to well below 2℃, preferably to 1.5℃, compared to pre-industrial levels” [26]. Consequently, countries around the world are now committed to reducing greenhouse gas (GHG) emissions associated with their economies. Offshore wind power is projected to be an important contributor in the global march to net zero emission [19]. Thus, developing feasible LF-HVac schemes for grid integration of OWPP could solve the present costs-related and capacity availability

problems encountered with offshore wind power installations [17]. Existing literature on LF-HVac have demonstrated, mainly theoretically, the technical and economic feasibility of the proposed transmission scheme [20], [21], [22], [23], [24], [27], [28], [29], [30]. However, since LF-HVac is expected to make use of commercially available HVac components and equipment, it is important to understand the performance characteristics of those devices when loaded with lower-than-designed-for ac frequency power. For instance, transformer voltage is frequency dependent. So, it has already been identified that for the same voltage level, the transformer used in a LF-HVac system would need to be proportionally larger, and consequently heavier, than its equivalent HVac system counterpart [18], [20], [22]. Therefore, the only way to use a commercially available HVac transformer in a LF-HVac system is to apply the applicable V/f derating.

However, frequency-dependent differences in the operational characteristics of ac power equipment are less apparent than in the case of transformers and other electromagnetic equipment. For instance, skin effect can noticeably affect the resistance of ac cables. However, in existing LF-HVac literature, some studies, [30], [18], have inaccurately used cable parameters specified at either 50/60 Hz in their LF-HVac studies. Therefore, a comprehensive review of essential HVac components and devices is necessary to determine if they exhibit any frequency-influenced characteristics. The results of such a study would add to the body of knowledge, thereby making the information accessible to researchers. So, in this thesis, it has motivated the investigation and the comprehensive review of the effects of ac frequency on cross-linked polyethylene (XLPE) cables used in offshore wind applications.

Furthermore, it may be beneficial to deviate from system design and operational methods typically adopted for nuclear, thermal, or hydro bulk power transmission systems. Unlike those

power installations, wind being an intermittent resource implies that LF-HVac-based OWPP installations would have comparably lower utilization factor. This feature should motivate the adoption of unconventional approaches in their design and operation. Studies presented in [31] demonstrate how variable transmission voltage operation of long HVac cables reduces its overall transmission losses. A LF-HVac frequency optimization study has shown that for minimal transmission losses, the system needs to adjust its frequency in line with varying reactive power requirements at the receiving end of the line [32]. So, both studies have inspired the primary objective of this thesis, which is to investigate the technical feasibility and the benefits of operating the proposed LF-HVac transmission scheme for OWPP using simultaneous voltage and frequency variation technique while maintaining a constant voltage/frequency (V/f) ratio for the transformers and reactors.

1.4. Thesis Statement and Research Objectives

The main goal of this thesis research is to investigate system level design and operational features for the proposed LF-HVac transmission scheme for grid integration of offshore wind. As a new technology that is still under consideration, it is important that several studies and design iterations are presented, and the performance metrics juxtaposed with those of HVdc and HVac schemes. Comparable or better performance results from a range of peer-reviewed LF-HVac studies are what would convince utility stakeholders to adopt the technology. In line with this objective, this thesis proposes and investigates the technical feasibility and the merits of employing V/f control method in the operation of LF-HVac offshore wind installations. This would go beyond the currently available studies, whereby the LF-HVac systems have been

mostly designed to operate at a single nominal frequency. The following enumerates the steps and objectives involved in achieving the outlined goals of this thesis:

1. Comprehensive study and review of XLPE cable performance, including its electrical characteristics, when operated at frequencies lower than the conventional 50/60 Hz. The investigation showcases the advantages of LF-HVac operation of export cables, in comparison to HVac operation, in terms of reduced ac resistance, reduced overall losses, and increase in the current carrying capacity of the cable system.
2. Steady state analysis and performance study of LF-HVac operated export cables. This study develops the steady-state model applied in the determination of the feasibility of the proposed V/f controlled LF-HVac transmission system for offshore wind.
3. Investigation of the technical feasibility of the proposed V/f control operation strategy in LF-HVac for optimum power transmission of the irregular offshore wind energy via the export cable system.
4. Investigation of the feasibility, and more especially the determination of the energy storage requirements, i.e., the submodules capacitor sizing, of the modular multilevel converter (MMC) when applied as the frequency converter technology of the proposed V/f controlled LF-HVac transmission scheme.
5. Time domain simulations of the detailed LF-HVac system for offshore wind model in the PSCAD/EMTDC software to validate the theoretical concept and the analytical study results. The choice of PSCAD/EMTDC software for electromagnetic transient (EMT) simulations is informed by its availability and the wealth of experience in its use within the author's research group.

1.5. Thesis Outline

This thesis is organized as follows:

Chapter 1 provides the background to the research presented in this thesis, in addition to the motivation, problem definition and research objectives of the thesis.

Chapter 2 provides a summary of LF-HVac transmission research investigations available in the literature. The discussions are centered on its feasibility studies, proposed frequency converter technologies, and the impact of LF-HVac transmission on electromagnetic power equipment, like the transformer.

Chapter 3 presents the study on power transmission cables and the effects of LF-HVac frequency values on their electrical characteristics and efficiency performance metrics.

Chapter 4 presents the analytical study on the steady state performance and power flow characteristics of export cables when operated under the proposed V/f controlled LF-HVac transmission scheme for offshore wind.

Chapter 5 presents the analytical study on the feasibility of, and the energy storage requirements (i.e., the minimum submodules capacitor sizing) of MMC when applied in the frequency conversion of the proposed V/f controlled LF-HVac transmission scheme for offshore wind.

Chapter 6 presents the EMT validation of the studies presented in Chapter 3 through Chapter 5 through detailed model simulations of the V/f controlled LF-HVac system for offshore wind.

Chapter 7 outlines the thesis contributions, conclusions, and the recommendations for future work.

Chapter 2

Literature Review and Thesis Research Questions

This chapter provides brief reviews of existing studies on the feasibility of LF-HVac transmission, the technical and economic advantages of the proposed bulk power transfer scheme, its suitability suggestions for interconnecting remote OWPPs, and discussions on candidate converter technologies that could power the system. These topics are important in understanding the state of the art for the budding LF-HVac transmission technology for offshore wind. However, more importantly, they highlight gaps requiring improvements in the transmission scheme. The identified gaps inspire the research questions this thesis addresses.

2.1. LF-HVac: A Brief History

As already mentioned in Chapter 1, 25 Hz was the last contender to 60 Hz as the standard ac operating frequency in North America. 25 Hz was preferred for bulk power transmission because it provided better efficiency and voltage regulation performance [2]. At the time, interconnections between ac systems of different nominal frequencies were implemented via rotary frequency converters (RFCs) [25]. Today, power electronics-based static frequency converters (SFCs) are available. They are cheaper and more efficient than RFCs. Consequently, the reintroduction of ac bulk power transmission scheme, which would operate at a frequency much smaller than the conventional 50/60 Hz has been proposed. Wang [27] first came up with this proposal in 1996. Originally termed Fractional Frequency Transmission System (FFTS), the study investigated the feasibility and the efficiency of using FFTS, which would operate at 16.67 Hz, to transmit hydro power from western China to load centres in the East and in the South of

the country. A HVdc option was considered too expensive at the time. The simulation results showed that a 550 kV FFTS, modelled with magnetic frequency changers (with the option of using power electronics converters also suggested), could transmit up to 1700 MW over 1200 km. In 2000, Funaki [28] studied the feasibility of using LF-HVac on XLPE cables as a means of circumventing the space charge accumulation problem encountered when the cables are energized with HVdc. Both the transient and the stability analyses calculations and simulations results showed performance outcomes comparable to those of HVdc. The frequency converter used in the latter study was a cycloconverter [28]. Since then, several research investigations on LF-HVac have been carried out, and the most relevant studies are presented in the subsequent sections.

2.2. Key Advantages of LF-HVac

The expected benefits, both technical and economic, in the proposed development of LF-HVac bulk power transfer scheme are outlined under the following two sub-headings.

2.2.1. Boost in Power Transfer Capacity

The study presented in [29] used a scaled hardware, represented schematically in Fig. 2-1, to experimentally demonstrate that a 1200 km, 500 kV, 16.67 Hz LF-HVac transmission line could export up to 2000 MW of active power. For an equivalent 50 Hz HVac line, real power transfer would have been limited to 800 MW. Therefore, reducing ac frequency value by a third could boost power transfer capacity by a factor of 2.5.

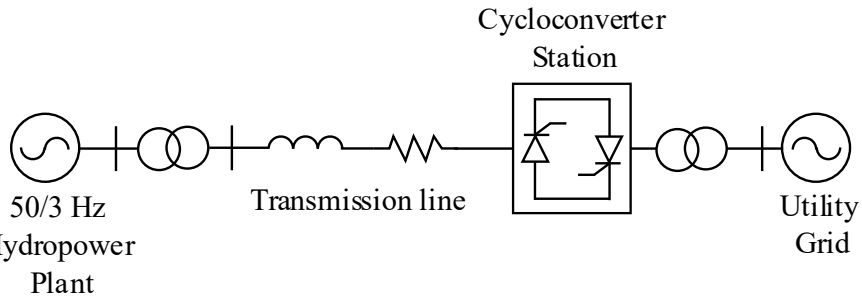

Fig. 2-1: Schematic representation of the experimental hardware used to investigate FFTS power transfer capacity in [29].

In a 3-phase ac cable transmission system, (2-1) gives the charging current per phase, I_c. Equation (2-2) gives the reactive power generated in the cables, Q_c, and (2-3) gives the useful power that can be conveyed to a delivery point via the cable system, P_R [18], [28], where C is the capacitance per unit length per phase, V is the rated line voltage, and S is the apparent power at the sending end. Symbols of the other variables in the equations have been previously defined. Note that in those equations, it has been assumed that the voltage and the current profiles are constant, i.e., they do not change along the length of the cable.

$$I_c = \frac{2\pi f C V}{\sqrt{3}} \times l \tag{2-1}$$

$$Q_c = \sqrt{3} V I_c \tag{2-2}$$

$$P_R = \sqrt{S^2 - Q_c^2} \tag{2-3}$$

Therefore, for a double circuit 3-core XLPE ac cable system, whose parameters are listed in Table 2-1, Fig. 2-2, generated by the author using (2-1)-(2-3), shows how much real power, including the applicable transmission distance, can be transferred through it when operated at different nominal frequency values. The curves in Fig. 2-2 show that for operation at the conventional 50/60 Hz, and with no reactive compensation applied, no useful power could be

Table 2-1: Parameters of a 275 kV 3-core XLPE submarine cable system [33].

Parameter	Value
Nominal voltage (kV)	275
Conductor cross-section (mm^2)	1000
Conductor material	Copper
Current rating (A)	825
Cable capacitance (μF/km, per phase)	0.18
Cable inductance (mH/km, per phase)	0.39
Rated MVA	750

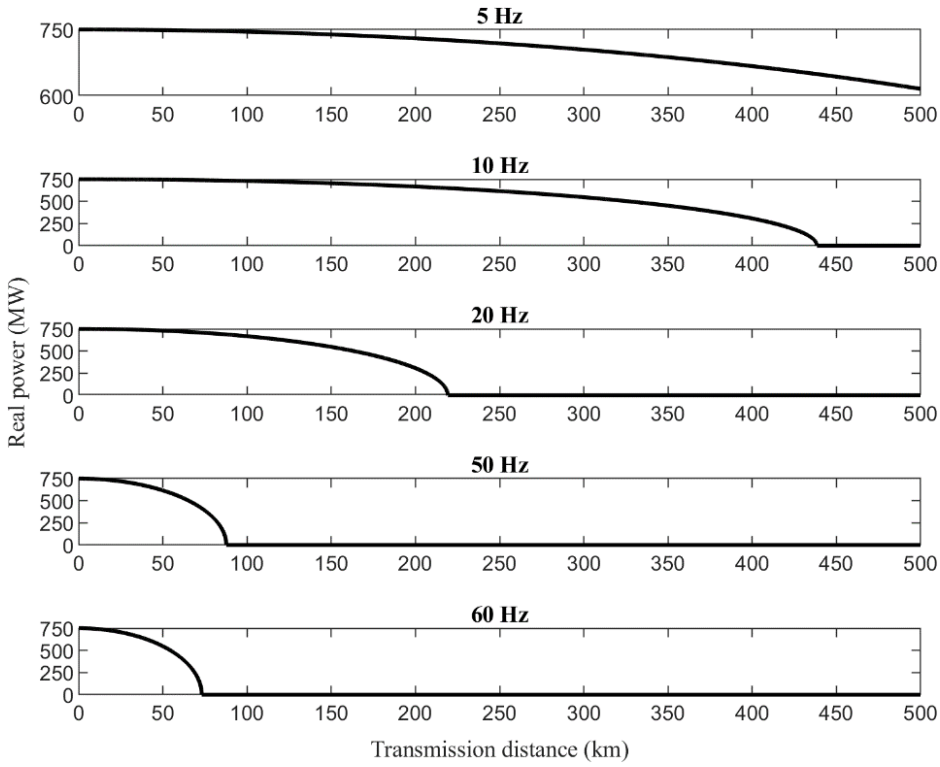

Fig. 2-2: Real power transfer vs. transmission distance plots (computed using (2-1)-(2-3)) in the double circuit 3-core XLPE cable system, whose parameters are listed in Table 2-1.

delivered beyond 90 km and 70 km from the source, respectively, for the ac system operation at 50 Hz and 60 Hz. On the other hand, if the same cable system, and still with no reactive compensation applied, is operated at 20 Hz, some useful power could be delivered to a load point located 200 km from the power source. The cable power transmission capacity and range would further increase as the operating frequency is further reduced, as shown for the 5 Hz and the 10 Hz ac operation power transfer curves.

2.2.2. Potential for Multiterminal Networks

The availability of natural zero current, which occurs twice in each cycle, allows ac circuit breakers (CBs) to interrupt fault currents [6], [34]. Therefore, in a large ac power network, faulted section(s) can be readily isolated without the whole system being shut down for repairs or even during scheduled maintenance. On the other hand, dc has no natural zero current. Consequently, dc fault current must be artificially forced to zero before its interruption can occur [6], [35], [36], [37]. Different kinds of dc CBs have been introduced over the years. Currently, hybrid HVdc CB is the more widely used technology for implementing dc fault current interruption and isolation [38], [39], [35], [36]. However, HVdc CB is still a growing technology, unlike the mature HVac CBs [37]. For perspective, the first HVdc grid anywhere in the world, incorporating the hybrid HVdc CB [38], [39], [36], was only commissioned in 2019 [40]. Located in China, the Zhangbei multiterminal HVdc network has four stations arranged in a ring.

On the other hand, LF-HVac could employ CBs with principles and operations like those used in the widely available HVac CBs. Consequently, LF-HVac has been proposed as a more, technically and economically, viable option when it comes to multiterminal power networks than

HVdc [28], [18], [37], [41]. However, it is worth mentioning that at lower than the conventional operating frequency, current interruption would take longer than what is obtainable in 50/60 Hz HVac systems. Therefore, CBs used in LF-HVac would need to have heavier duty valves compared to an equivalent HVac CB [28]. However, this challenge can be overcome, for example, by use of appropriately derated CBs originally designed for higher HVac voltage and power levels [41]. Thus, given LF-HVac's potential access to ac transformer and CB, devices which would be simpler than their HVdc counterparts, multiterminal LF-HVac could be more economically and technically feasible than multiterminal HVdc. For example, such an arrangement could be used to interconnect offshore wind submarine cable systems that were originally designed for operation at different voltage levels [41], thereby improving the availability of those wind capacities and the offshore wind installations.

2.3. Offshore Wind Power

Desire for more efficient wind farms has led the industry to embark on offshore wind power projects. Offshore, wind speeds are often faster and steadier than on land [17], [42]. So, larger turbines with higher capacity factors can be used to capture more energy, up to 50% more electricity, than on land [42]. Presently, there is no operational offshore wind farm in Canada, but projects of about 3.6 GW of installed capacity have been proposed [42]. On the other hand, Europe's geography, and its population density and distribution, especially along the coasts, have prompted successful takeoff of offshore wind power in that region [11], [42]. To keep temperature rises below 1.5℃, the European Commission projects that 240-450 GW of offshore wind power would be needed, in EU countries alone, by 2050 [43]. This would amount to about 30% of the region's future electricity demand. As at the end of 2020, Europe had a total installed

offshore wind capacity of 25 GW, with 2.9 GW added in that year alone [44]. Therefore, the offshore wind power industry is set to grow by double digits per annum over the coming decades.

2.3.1. Offshore Wind Farms: Industry Trends

Recently completed and still-in-planning offshore wind projects in Europe have seen a growth in individual turbine capacity, and in siting wind farms in deeper waters, farther away from the shore [44]. Europe is a trend setter in the industry because it presently accounts for 70% of all installed offshore wind capacity in the world [44], [45]. Since 2015, individual offshore wind turbine power rating has grown consistently by 16% [44]. Projects that are planned to come into operation after 2022 will have turbines with power ratings in the range of 10 to 13 MW [44]. Fig. 2-3 shows the yearly growth charts of rated capacity of offshore wind turbines, and the average size of offshore wind farms [44].

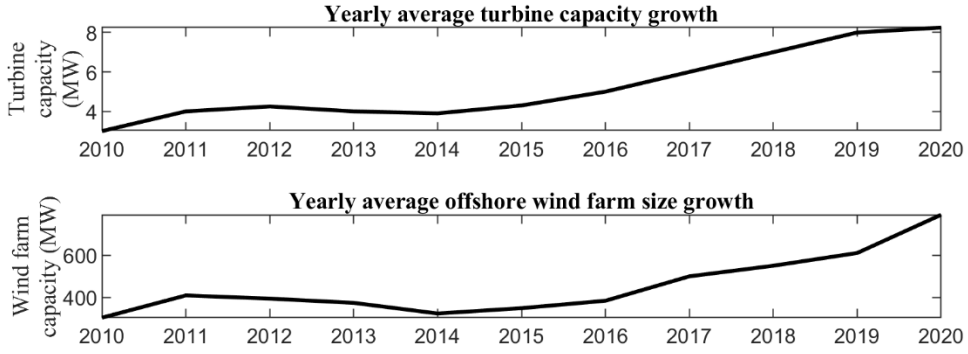

Fig. 2-3: Charts of yearly growth in the rated capacity of offshore wind turbines, and the average size of offshore wind farm projects [44].

In a bid to lower costs through economies of scale, the industry is now moving towards GW-scale wind farms [44]. The 1.2 GW Hornsea One in the UK is a good example of this.

Commissioned in 2019, it is the world's second largest offshore wind farm [44], [46], recently (in 2022) overtaken by its sister project, the 1.3 GW Hornsea Two [47]. Fig. 2-4 shows that offshore wind projects under construction and those still in the planning stages in Europe will be sited in deeper waters, up to 200 km from the coast [44]. Therefore, there will be increasing demand for efficient and cost-effective means of delivering offshore wind power to load centers onshore. For instance, the German and the Belgian transmission system operators (TSOs) consider clustering wind farms into a single offshore substation to be the most efficient way of integrating offshore wind power to their grids [44]. Therefore, there may be ample opportunity for LF-HVac to be introduced and adopted in solving these challenges in the future.

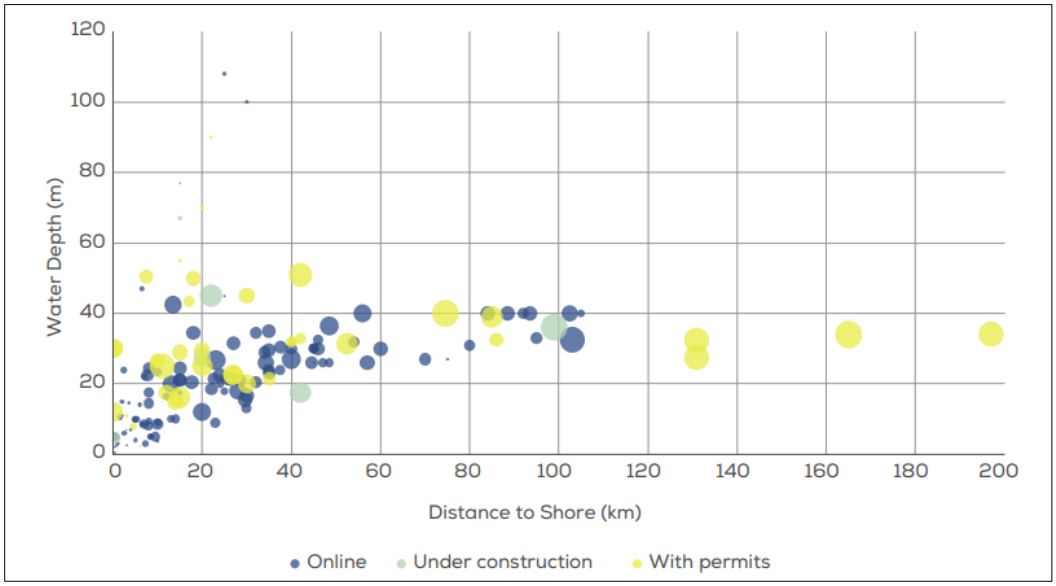

Fig. 2-4: "Average water depth and distance to shore of offshore wind farms in Europe. The bubble size indicates overall capacity of the site [44]."

2.3.2. Hornsea One: A Change in the Industry Position on HVdc?

Located in the North Sea, 120 km off the coast of Yorkshire, UK, Hornsea One, until recently, used to be the largest offshore wind power project in the world [46]. It recorded the following technical milestones:

a. First offshore wind farm in the world with over 1 GW capacity. At 1.2 GW, it was double the size of the second largest offshore wind farm, when it was commissioned.
b. Most remote, from the shore, offshore wind farm, at 120 km distance to shore.
c. Longest HVac submarine cable transmission system.
d. First offshore reactive compensation station.

HVdc was initially proposed to be used for the grid integration of Hornsea One [48]. However, HVac, with offshore reactive power compensation was eventually used. It is not very clear why this switch was made. However, it could be assumed that economic considerations played a significant role in the unprecedented decision in choosing HVac with offshore reactive compensation over HVdc. This shows that having a converter station located offshore, as in the case of HVdc, comes with significant costs, both capital and operational, which the industry may not be willing to accept going forward. Therefore, it could be envisaged that the proposed LF-HVac could become attractive in offshore wind applications as wind farms continue to grow in capacity, in addition to being sited farther from the coast. LF-HVac would not require any offshore converter station. Furthermore, offshore reactive compensation of the export cable system would not be required, at low enough operating frequencies [11], [49].

2.4. Frequency Converter Technologies for LF-HVac

This section presents an overview of frequency converters that have been considered and proposed for use in LF-HVac transmission. As mentioned in Chapter 1, modern power electronics have led to the development of static frequency converters, which are more efficient and less expensive than legacy rotary frequency converters used in low frequency ac railway systems [25]. Static frequency converters that have been proposed for use in LF-HVac include ac-ac cycloconverter [28], [29], [23], [21], [49], ac-ac modular multilevel matrix converter (M3C) [50], [51], and ac-dc-ac back-to-back voltage source converter (BtB-VSC) [52], [53], [18], [54].

2.4.1. Cycloconverter

Thyristor-based line commutated cycloconverter was initially proposed for frequency conversion in LF-HVac. This preference was due to its relatively low cost and wide application in high-power motor drives [28], [29], [23]. Modern cycloconverters are phase-controlled devices used to convert ac power at an input or primary frequency to output ac power at a different frequency, termed the secondary frequency [55]. Fig. 2-5 shows the block diagram of a cycloconverter. Studies presented in [23], [29], [49] used a three-phase-to-three-phase cycloconverter with 36 thyristors, shown in Fig. 2-6, as their LF-HVac frequency converter. The cosine crossing method is used to determine the firing angles of the thyristors [49]. Usually, cycloconverters are used to step down frequency from the grid nominal frequency to a lower frequency, as required by that application. However, for LF-HVac integrated offshore wind farms, the reverse would be the case [18], [29].

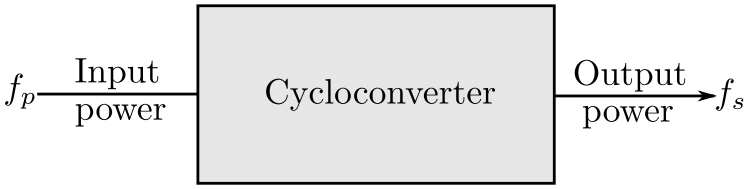

Fig. 2-5: Block diagram of a cycloconverter.

Note that operation of cycloconverters leads to output voltages with high harmonic contents [18], [29], [49], [55]. Therefore, ac filters are required on both sides of the cycloconverter since output voltage harmonics correspondingly reflect harmonics on the input line current [49], [55]. As previously mentioned, cycloconverters used in LF-HVac grid-integrated offshore wind would have their output frequency higher than the input frequency. Consequently, inter-harmonics, i.e.,

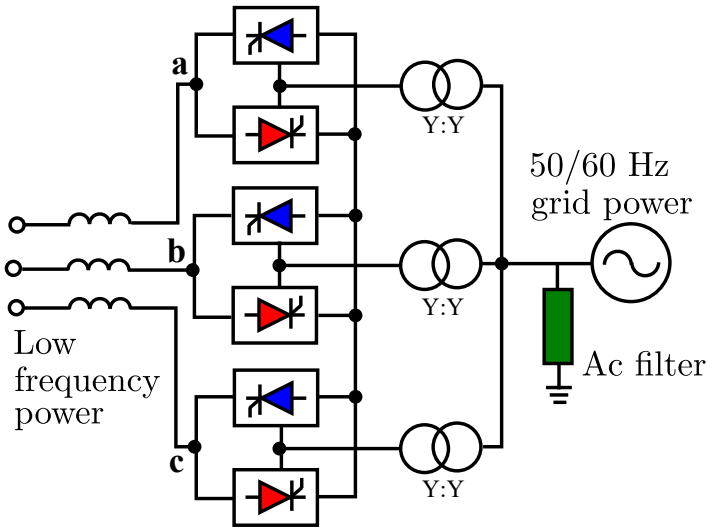

Fig. 2-6: Three-phase bridge 36-thyristor cycloconverter (also known as six-pulse cycloconverter).

harmonics which are not integer multiples of the output frequency, would be encountered [18]. Sub-harmonics, where the harmonics order is below the output frequency, would also be present.

Both sub-harmonics and inter-harmonics are complex harmonics, which are difficult to filter out. Thus, cycloconverter-based LF-HVac systems would require large and complex filters. Given the high standard for power quality demanded in modern electricity grids, this is seen as a major drawback in using cycloconverter as the frequency converter for grid-connected LF-HVac transmission schemes [18], [23], [49].

2.4.2. Matrix Converter and Modular multilevel matrix converter (M3C)

Modular multilevel matrix converter (M3C), as the name suggests, is a multilevel adaptation of the basic matrix converter. The matrix converter is a kind of cycloconverter. However, in lieu of the phase-controlled line commutated thyristor switches, it makes use of pulse width modulated (PWM) self-commutated bi-directional switches [55]. Fig. 2-7 shows a

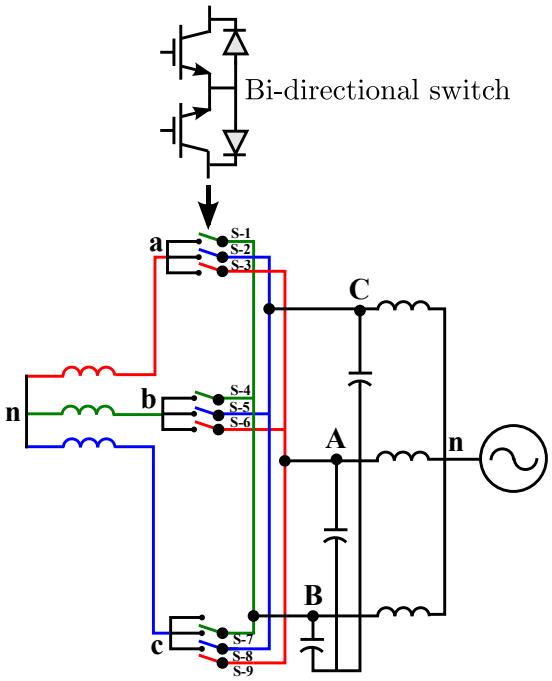

Fig. 2-7: Three-phase-to-three-phase matrix converter.

three-phase-to-three-phase matrix converter. It consists of a nine bi-directional switch matrix, which allows the connection of any input phase to any output phase. PWM control of the switches creates an output fundamental voltage, whose magnitude and frequency can be varied as desired. Unlike a voltage source converter (VSC), the matrix converter does not have energy storage elements, i.e., capacitors [18]. Thus, it has a more compact topology than VSC. However, it has a much higher device count (eighteen insulated gate bipolar transistors (IGBTs) and eighteen diodes) in comparison to a comparable BtB-VSC (twelve IGBTs and twelve diodes) [55]. Additionally, matrix converters allow transfer of disturbances from the input voltage to the output voltage since there is no intermediate dc link [18].

Modular multilevel matrix converter (M3C) has been introduced to overcome the output-input voltage gain cap of 86.6% encountered in matrix converters [18], [50]. Its topology is like

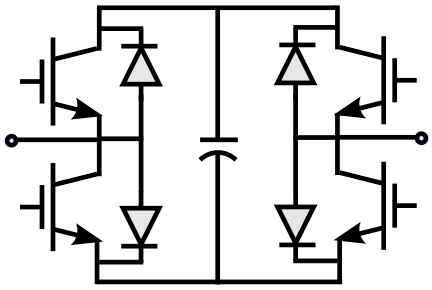

Fig. 2-8: Circuit diagram of an H-bridge switching cell used in M3C.

that of a matrix converter. However, the major deviation is that, instead of the bi-directional switches used in matrix converters, M3C makes use of H-bridge switching cells, which are capable of four-quadrant operation. Fig. 2-8 shows the circuit diagram of an H-bridge switching cell. The modular and multilevel configuration of M3C allows for it to be used in high-voltage and high-power applications. This feature also contributes to its reduced harmonics output [51].

M3C also has the capacity to rapidly control reactive power at both its input and output terminals. Thus, bulky capacitor for energy storage and reactive power compensation is not a requirement. It has been observed that control of M3C for LF-HVac would be complex since both active and reactive power control of two ac systems, given there is no dc link, is involved [51]. There is also the issue of voltage balancing control for the series H-bridge cells. Furthermore, M3C is still a developing technology, and it is yet to be widely used industrially [18]. Therefore, M3C may not be a practical frequency converter to be used in LF-HVac transmission, at least in the short term.

2.4.3. Back-to-Back Voltage Source Converter (BtB-VSC)

Ever since the Hellsjon Project (in Sweden), the world's first VSC-HVdc transmission scheme [56], went into operation in 1997, VSC has been used in high-voltage and high-power applications, which used to be the exclusive domain of line-commutated current-sourced converters (LCC) HVdc [36], [57], [58]. This is largely thanks to technological advancements in IGBTs, some of which are now rated up to 6.5 kV and 2 kA. HVdc converters connected back-to-back have been used to interconnect asynchronous ac systems, for instance, the 50 and 60 Hz grids in Japan [59]. In the same vein, BtB-VSC has been proposed and studied for frequency conversion in LF-HVac [18], [24], [53], [54]. Both the two-level and the modular multilevel converter (MMC) topologies have been considered. Fig. 2-9 shows the circuit diagram of a two-level BtB-VSC. Details of the converter operation are well explained in [60]. Initial VSC-HVdc applications adopted the two-level and the three-level configurations. Such configurations require connecting several semiconductor devices in series to achieve the desired high voltage.

However, having many series semiconductor devices switched on simultaneously presents technical challenges, which ultimately affects the reliability of two-level VSCs [61], [62].

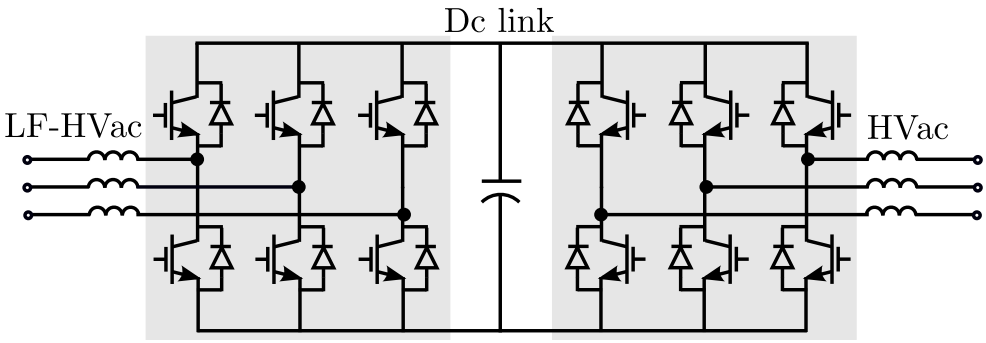

Fig. 2-9: Two-level BtB-VSC.

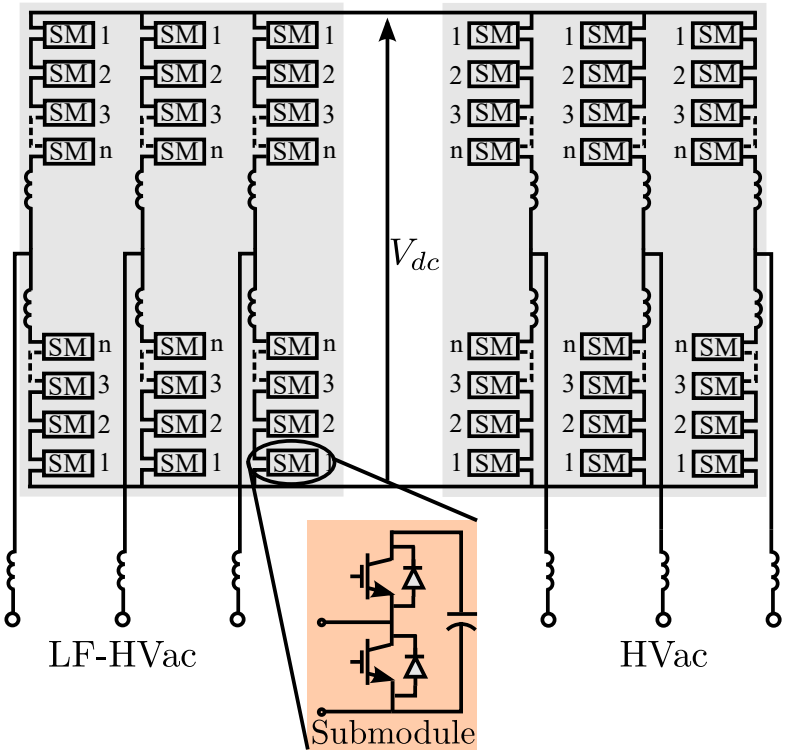

Fig. 2-10: MMC BtB-VSC with half-bridge submodules (SMs).

MMC-VSC is the state-of-the-art converter technology used in VSC-HVdc applications. Fig. 2-10 shows the schematic diagram of a three-phase MMC with half-bridge submodules (SMs). Unlike two-level VSC, MMC has a modular configuration. This provides flexibility in scaling the converter voltage and power. Series connection of semiconductor devices is not required to achieve high voltage operation [63], [64]. Therefore, lower rated IGBTs can be used to build the converter. Other advantages include reduced switching losses, and minimal or no ac filtering requirement. Detailed explanation of MMC operation and configuration types can be found in [61], [63], [65]. However, compared to two-level VSC, MMC requires a large number of semiconductor devices and capacitors [62]. This directly contributes to its higher cost, in addition to greater complexity of its control systems. For LF-HVac applications, the costs may be escalated because larger capacitors would be required in each submodule [53], [54]. Consequently, using a BtB-VSC with two-level VSC on the low frequency side and MMC on the grid frequency side has been proposed [53] to overcome this challenge. Nevertheless, more studies on the trade-offs are necessary to come to a definite economic conclusion on which BtB-VSC configuration should be used in LF-HVac transmission.

2.5. LF-HVac Frequency-Dependent Equipment

This section considers the impact of reduced ac frequency operation on the physical dimensions of transformers, reactors, turbines, and other associated electromagnetic ac equipment that may be used in LF-HVac transmission.

2.5.1. LF-HVac Transformer

In an ac system, transformers are used to step up or step down voltages to required levels. Power transformers used in conventional HVac are highly efficient devices, with efficiencies exceeding 99% [66]. Equation (2-4) is the transformer voltage equation,

$$E = 4.44fBNA \tag{2-4}$$

where E is voltage, f is frequency, B is magnetic flux density, N is number of turns, and A is transformer core cross-sectional area. This shows that voltage output of a transformer is frequency dependent. Note that below 100 Hz, magnetic flux density is independent of frequency [67]. Therefore, the only way to maintain the same output voltage while reducing frequency would be to increase either A or N, or both simultaneously. Consequently, a major drawback of LF-HVac is that its transformers would be physically larger and heavier than equivalent 50/60 Hz transformers. It has been suggested that maintaining a constant V/f ratio could be used in derating transformers originally designed for operation at 50/60 Hz [18]. However, this would reduce the power handling capacity of the transformer. Therefore, for a given LF-HVac power capacity, more V/f-derated transformers would be needed than if the transformers were specifically designed for LF-HVac operation.

In the light of this, size, and weight optimization methods for LF-HVac transformers have been studied. Wyllie et al. [68] designed two extreme versions of a 250 MVA, 16.67 Hz transformer, and compared them to a 250 MVA, 50 Hz transformer. The 16.67 Hz transformers were designed as follows:

a. A 50 Hz transformer was modified by increasing the thickness (in effect its cross-sectional area) of its magnetic core while leaving the number of windings turns unchanged. This version is termed the wide design.

b. Increasing the 50 Hz transformer windings windows' height and increasing the number of turns while leaving the thickness of the core unchanged. This version is termed the tall design.

Fig. 2-11 presents a pictorial comparison of the two 16.67 Hz transformer designs in reference to the conventional 50 Hz transformer design. The results show that the 16.67 Hz tall design would be about 1.8 times heavier than a 50 Hz transformer of similar capacity. On the other hand, the 16.67 Hz wide design is almost 3 times heavier than the equivalent capacity 50 Hz transformer. Furthermore, the 16.67 Hz tall design transformer volume would be about 1.7 times larger than that of the equivalent capacity 50 Hz transformer. On the other hand, the 16.67 Hz wide design transformer would be 2.5 times bigger than its 50 Hz counterpart. These two extreme designs show that an optimal LF-HVac transformer design could be arrived at, where size and weight would not be a direct multiple of the ratio between HVac frequency and the LF-HVac frequency.

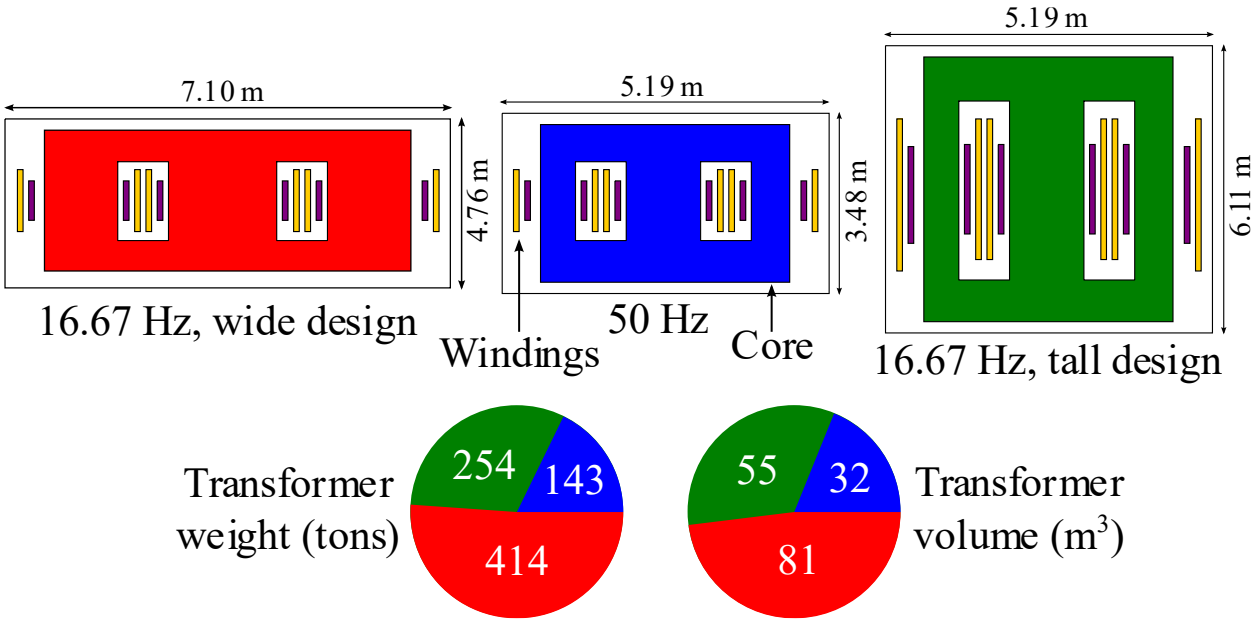

Fig. 2-11: Comparison of size and weight properties of a 50 Hz (HVac) and the two extreme configurations of equivalent 16.67 Hz (LF-HVac) transformers [68].

2.5.2. LF-HVac Wind Turbine

Wind turbines are equipped with transformers to step up its output voltage to medium voltage (MV) level (33kV or 66 kV) for the collection network. Most offshore wind turbines are horizontal axis wind turbines, i.e., the main rotor shaft rotates into the direction of the wind [69]. The nacelle, mounted atop the turbine tower, houses the rotor, generator, transformer, and other associated equipment. Reference [69] presents a comprehensive discussion of the types and the configurations of wind turbines used in large-scale offshore wind farms. There are two main classes of wind turbines: constant speed wind turbines, and variable speed wind turbines. As the name suggests, constant speed wind turbines operate at a fixed speed. Its generator is a squirrel cage induction generator, which is a robust and mechanically simple machine. This feature contributes to its relatively low cost. However, this turbine type is not able to take advantage of a wide range of wind speed [69]. In addition, it also suffers from rotor speed instability. Authors of [23] used a constant speed wind turbine for the 16.7 Hz LF-HVac study presented in their paper. The [23] study simulation results show that the dynamics of the turbine was unstable during start-up [18]. Consequently, the authors suggested that the turbine should be redesigned to have a larger inertia to eliminate the instability problem.

On the other hand, variable speed wind turbines can adapt to changing wind speed, within a design-specific range [69]. Such turbine types are equipped with either a full-rated converter or partially rated converter. Variable speed wind turbines with full-rated converter, referred to as Type IV wind turbines, convert the whole harnessed wind power, at usually low (< 50/60 Hz) and/or variable electrical frequency, to grid frequency (or to the applicable frequency, in the case of LF-HVac). Type IV wind turbine generators can be either a squirrel cage induction generator or a permanent magnet synchronous generator (PMSG). On the other hand, a partially rated wind

turbine consists of a doubly fed induction generator (DFIG), and a partially rated (about 30% of the power) power converter. Note that most wind turbine generators have voltage ratings in the range of 380-690 V [69]. Therefore, step-up transformer is essential in raising the output voltage of each turbine to MV level. As turbine power ratings increase, so does the size and the weight of the step-up transformer. Consequently, there is ongoing research on methods to reduce the size and the weight of turbine transformers. More details of the proposed methods can be found in [69]. Some studies have also considered replacing step-up transformers entirely with multilevel power converters. Given that LF-HVac transformers are expected to be bigger and heavier than their HVac counterparts, outcome of turbine transformer size and weight optimization studies could be beneficial to LF-HVac offshore wind applications.

2.6. Key Takeaways from the Literature Review

Following the literature review on LF-HVac, here is a summary of the highlights:

1. LF-HVac technology has the potential to increase the power transfer capacity of a given submarine cable system.
2. Being ac, LF-HVac could be amenable to multiterminal interconnections like the conventional HVac since it could make use of the already mature and commercially available ac circuit breakers.
3. Offshore wind energy, from remote wind farms, is being targeted as a source of clean energy, with projections for substantial growth in the coming decades. However, reliable, and less expensive technology for the energy transmission to the grid onshore is highly sought after to reduce the cost of electricity from offshore wind farms.

4. Modern HVdc systems majorly utilize VSC converter technology, with the MMC being the state of the art. Thus, most of the studies referenced in the literature review favour BtB-VSC for use at the frequency conversion stage of the proposed LF-HVac transmission scheme.
5. However, given the potential advantages of LF-HVac, its major drawback would be the larger size and weight requirements of the associated electromagnetic components, like the transformer, when compared to those used in voltage/power equivalent conventional HVac systems.

2.7. Thesis Research Questions

Literature review in research is an exploration exercise whose outcome not only provides detailed background of a given topic, but more importantly it helps the researcher(s) to identify gaps in research on that subject. The identified gaps in research often present as research questions which need to be answered through careful and methodical research. Therefore, following the literature review conducted on the topic of low frequency ac transmission for the grid integration of offshore wind, and hereby presented in this chapter, the following are the research questions this PhD thesis intends to provide answers to.

1. Most of the referenced LF-HVac studies used one-third of the conventional 50/60 Hz, i.e., 16.67 or 20 Hz, as the ac operating frequency value. Very little information was provided to justify the choice of either frequency value. However, given that wind power is intermittent and non-dispatchable, would there be an optimal nominal ac operating frequency for the LF-HVac transmission system?

2. It is evident that under LF-HVac transmission, associated electromagnetic equipment, most especially the transformer, would have to be, and in a substantial way, physically larger and heavier than equivalent equipment used in the conventional HVac transmission systems. For a dispatchable power source with a high utilization factor, e.g., a thermal power plant, being operated under the LF-HVac system, it would be difficult to get around the increased size and weight of the transformer and other associated electromagnetic equipment. On the other hand, wind power is highly variable and wind power installations do have low utilization factor. Therefore, the question these identified characteristics raise is whether some practical methods can be adopted in minimizing the physical dimensions and weight of transformers required in wind power LF-HVac transmission?
3. As a follow up to the first thesis research question, if research shows there is no single optimal nominal operating frequency for LF-HVac grid integration of offshore wind, would it be technically feasible and/or beneficial for the system to be operated within a variable frequency regime? This question is pertinent given that the power system hardware would be fixed. Variable frequency operation could also pose problems to the frequency converters controller design and parameters selection, in addition to the overall stability of the system.
4. As the name implies, LF-HVac specifically suggests reducing the ac nominal frequency, i.e., below the conventional 50/60 Hz, as a means of directly increasing the capacity of a given transmission system. For a cable transmission system, as shown by (2-1) to (2-3), the frequency parameter contributes to the magnitude of the charging current in the cable, which in turn affects the amount of useful power that

could be delivered to the load point. Nevertheless, beyond the frequency quantity, the voltage quantity V even has more impact on the magnitude of the deliverable real power. A quick observation of (2-5) would confirm this. Therefore, given the intermittent nature of wind, would it be technically feasible and/or beneficial to vary not just the ac frequency quantity, but also the LF-HVac grid voltage, simultaneously?

$$P_R = \sqrt{S^2 - 4\pi^2 f^2 C^2 V^4 l^2} \tag{2-5}$$

In the subsequent chapters, the presented studies have been inspired by the quest to provide cogent answers to the posed research questions.

Chapter 3

Electrical Characteristics of Submarine Cables in LF-HVac Transmission

3.1. Introduction

The objective of this chapter is to investigate the impact of the ac operating frequency on the electrical characteristics of commercially available submarine cables when used in LF-HVac transmission. The study would also look at the performance of the cables, in terms of power transfer efficiency and capacity, when deployed in LF-HVac. Comparisons are made between the results for operation under the conventional HVac nominal frequency values, i.e., 50/60 Hz, and for operation under potential LF-HVac frequency values. Unlike overhead transmission lines, cable capacitance and the associated charging current are significant quantities, which directly affect the real power handling capacity of power cables. This chapter begins with the study of the physical and the electrical properties of submarine cables, with respect to operation at the non-conventional LF-HVac frequency values. Thereafter, the effects of operating frequency on the thermal performance and efficiency of the cables are then explored.

3.2. Construction of Below-Surface Power Transmission Cables

It has been mentioned that capacitance is a more significant quantity in power cables than in overhead transmission lines. This stems from the differences in the physical construction of

overhead transmission lines and submarine/underground power transmission cables. Overhead lines consist of bare single or bundled phase conductors. The conductors are usually stranded aluminium wires with steel wire(s) reinforcement in the middle (ACSR: aluminium conductor, steel-reinforced) [5], [70]. Fig. 3-1 shows the cross-section of an ACSR conductor, with seven steel strands and twenty-four aluminum strands. On the other hand, power cables contain one or more conductors surrounded by a protective sheath, often lead [70]. The conductors, which are

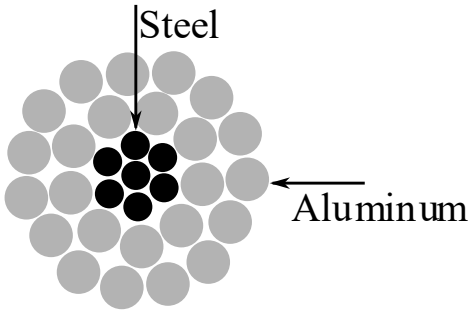

Fig. 3-1: Cross-section of an ACSR conductor used in overhead transmission lines.

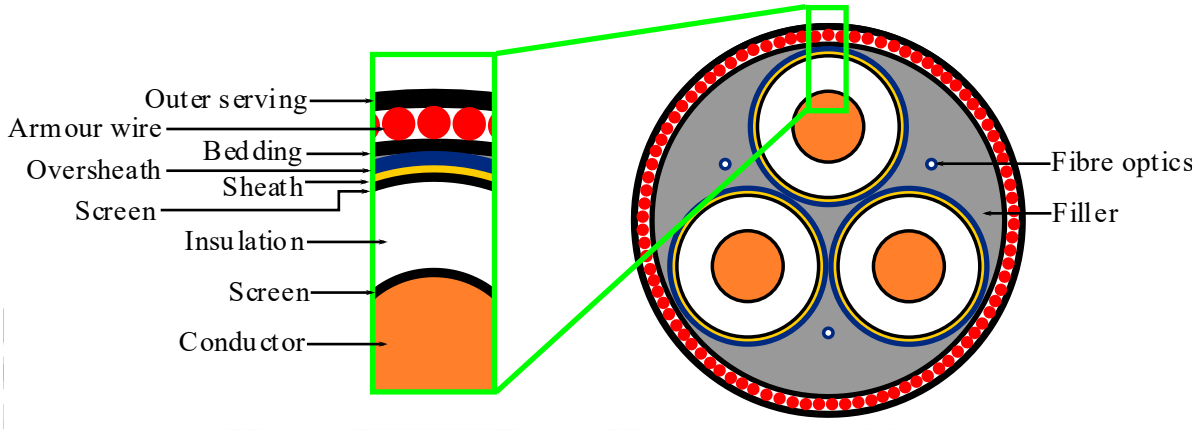

Fig. 3-2: Cross-section of a three-core XLPE power cable.

Table 3-1: Three-core XLPE cable layers and their geometric identifiers [71], [72].

Layer	Material	Outer diameter (mm)
Conductor	Copper/Aluminum (stranded)	d_c
Conductor screen	Polyethylene (PE)	d_{cs}
Insulation	XLPE	d_i
Insulation screen	PE	d_{is}
Sheath	Lead	d_s
Oversheath	Medium density PE (MDPE)	d_{os}
Filler	Polypropylene (PP)	d_f
Bedding	PP yarns	d_b
Armour	Galvanized steel (Individual steel wire diameter: d_{aw})	$d_a + d_{aw}$
Outer serving	PP yarns	D_{os}

made of stranded copper or aluminium wires, are separated from each other and from the sheath by a solid insulating material. Fig. 3-2 shows the cross-section of a three-phase, three-conductor (three-core) cross-linked polyethylene (XLPE) cable. XLPE is the insulating material used in modern power transmission cables [73]. Table 3-1 lists the layers, including their material type and geometric identifiers, of a three-core XLPE cable [71], [72].

3.3. Impact of Frequency on the Electrical Characteristics of Cables

Power cables, like overhead transmission lines, have associated series impedance $Z = R + j\omega L$, where R is the phase resistance and L is the phase inductance; and shunt admittance $Y = G + j\omega C$, where G is the shunt conductance and C is the shunt capacitance. In this section, the goal is to determine how significant the impact of operating power cables at a frequency lower than the conventional 50/60 Hz would be on their electrical parameters. Skin effect is a phenomenon whereby uniform current distribution across the cross-section of a conductor only exists for direct current flow [5]. For alternating current flow in the same conductor, skin effect causes non-uniform current distribution across the cross-section. In a round conductor, current density would be higher closer to the surface than at the centre of the conductor. This becomes more pronounced as the ac frequency is increased. Consequently, the phenomenon reduces the effective cross-sectional area of the conductor. Equation (3-1) implies that the ac resistance of a conductor would be higher than its dc resistance, where R is the resistance, ρ is the electrical resistivity of the material, l is the length of the conductor, and A is the effective cross-sectional area.

$$R = \frac{\rho l}{A} \tag{3-1}$$

Since skin effect is approximately proportional to frequency, the resistance of a conductor would be higher for current at a higher ac frequency than at a lower ac frequency. This investigation aims to gauge how significant the changes would be over a range of potential LF-HVac operating frequency values, and in comparison, to the conventional HVac 50/60 Hz.

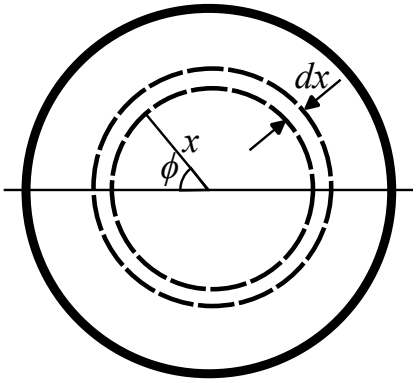

Fig. 3-3: Cross-section of a solid cylindrical conductor, with current flowing into the plane of the page.

Reference [70] presents detailed modelling and analysis of skin effect in solid, round conductors. Fig. 3-3 shows the cross-section of such a conductor. Note that current flows into the plane of the page. At x radial distance from the longitudinal axis of the conductor and displaced at an angle ϕ from the horizontal, as shown, the current density $s(x,t)$ is a function of x and time t. Evaluation of the applicable Maxwell's differential equations yields (3-2), which represents the complex current density as it varies from the centre of the conductor to its surface; where μ_0 is the permeability of free space, ω is the ac current angular frequency, and ρ is the resistivity of the conductor material.

$$\frac{d^2s(x)}{dx^2}+\frac{1}{x}\frac{ds(x)}{dx}-j\frac{\omega\mu_0}{\rho}s(x)=0 \tag{3-2}$$

Equation (3-2) is a Bessel differential equation of order zero, whose general solution is given by (3-3) [70]; where c_1 and c_2 are arbitrary constants, $k^2=-j\frac{\omega\mu_0}{\rho}$, and $J_0(kx)$ and $Y_0(kx)$ are Bessel functions of order zero, of the first and second kinds, respectively.

$$s(x)=c_1J_0(kx)+c_2Y_0(kx) \tag{3-3}$$

Further evaluations lead to (3-4), which is the total current in the conductor, i.e., the integral of the differential current over the radial distance from the conductor centre to its surface; where s_0

is the current density at the centre of the conductor (i.e., at $x = 0$), a is the radius of the conductor, and $J_1(kx)$ is a Bessel function of the first kind and first order given by (3-5).

$$I_{tot} = 2\pi s_0 \int_0^a J_0(kx)xdx = \frac{2\pi s_0}{k} aJ_1(ka) \tag{3-4}$$

$$J_0'(kx) = -J_1(kx) \tag{3-5}$$

The Bessel functions $J_0(kx)$ and $J_1(kx)$ are complex transcendental functions with infinite series and thus, they can be represented by (3-6) and (3-7), respectively; where $m^2 = \frac{\omega\mu_0}{\rho} = jk^2$, $M_0(mx)$ and $M_1(mx)$ are the amplitudes, and θ_0 and θ_1 are the angles of the complex functions.

$$J_0(kx) = ber_0(mx) + jbei_0(mx) = M_0(mx)e^{j\theta_0(mx)} \tag{3-6}$$

$$J_1(kx) = ber_1(mx) + jbei_1(mx) = M_1(mx)e^{j\theta_1(mx)} \tag{3-7}$$

Thus, at the surface of the conductor the current density is given by (3-8).

$$s(a) = \frac{I_{tot}}{2\pi a} k \frac{J_0(ka)}{J_1(ka)} \tag{3-8}$$

Consequently, the voltage drop per unit length along the conductor surface is given by (3-9), where r_{dc} is the dc resistance of the conductor.

$$V_{drop} = \rho s(a) = \frac{I_{tot}}{2\pi a} \rho k \frac{J_0(ka)}{J_1(ka)} = I_{tot} r_{dc} \frac{ma}{2} \frac{M_0(ma)}{M_1(ma)} \angle\left(\theta_0(ma) - \theta_1(ma) + \frac{3\pi}{4}\right) \tag{3-9}$$

As the ratio $\frac{V_{drop}}{I_{tot}}$ is the impedance of the conductor, its ac resistance is given by (3-10), i.e., the real part of the complex impedance.

$$r_{ac} = r_{dc} \frac{ma}{2} \frac{M_0(ma)}{M_1(ma)} \cos(\theta_0(ma) - \theta_1(ma) + \frac{3\pi}{4}) \tag{3-10}$$

Table IX in the Appendix of [70] lists values of M_0, M_1, θ_0, and θ_1 for a limited range of ma values. However, Appendix A of this thesis presents the formulae for determining values of M_0, M_1, θ_0, and θ_1 for any value of ma.

3.3.1. Variation of Ac Resistance with Frequency

Reference [30] provides a comprehensive rundown of the performance advantages of LF-HVac in comparison to HVac. The study claims that skin effect has negligible impact on the values of the resistance and the inductance of a transmission line. It determined that the variation of the resistance magnitude between 0 and 60 Hz was only 0.25% while the variation in the inductance magnitude was only 0.12%. Thus, the paper suggested that the electrical parameters determined for a transmission line at either 50/60 Hz operation could be used, with a high degree of accuracy, for calculations when the same line is operated at any lower LF-HVac frequency value. However, the diameter of the conductor used to conduct this study was only 5 mm, which amounts to a conductor cross-sectional area of about 20 mm^2. Of course, in such a thin conductor skin effect would not be significant. Even for a stranded conductor, skin effect becomes pronounced as the cross-sectional area becomes larger.

Experimental results have shown that increase in resistance due to skin effect in a stranded conductor (assuming the strands are all parallel to each other) is approximately equal to the increase caused in a solid round conductor having the same dc resistance [70]. Note that spiralling of wires only amounts to approximately 2% increase in the resistance of a stranded conductor, when compared to parallel strands with no spiralling [70]. The charts in Fig. 3-4, generated by the author using (3-10), show the variation in the value of ac resistance of three different conductor sizes (800, 1000, and 2000 mm^2) from their dc resistance values over a 1-60 Hz frequency range. The line plots show results at cable temperatures of 20℃ and 90℃. Note that 90℃ is the maximum operating temperature allowed in XLPE cables [73]. The cables' parameters, including the dc resistances of the conductors, used in the computation are presented in Table 3-2. The plots in Fig. 3-4 clearly show that skin effect results in substantial increase in

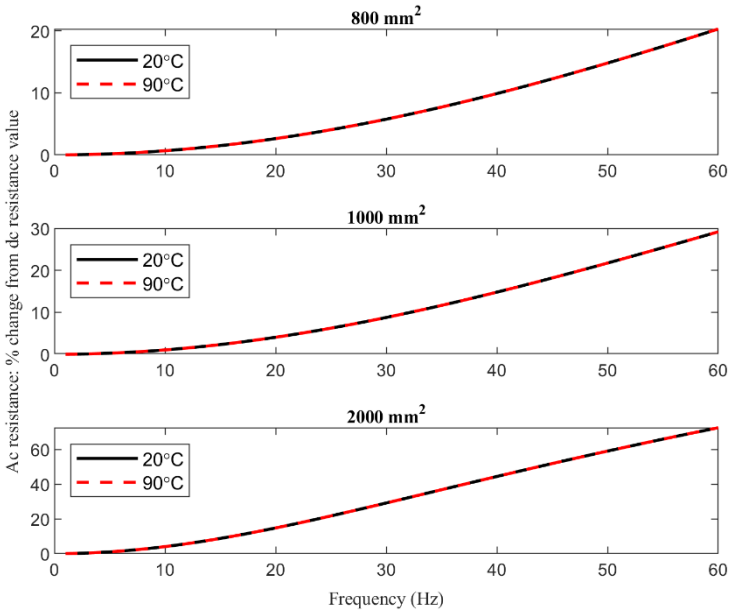

Fig. 3-4: Percentage increase in ac resistance, compared to dc resistance, vs. frequency plots for three conductor sizes.

Table 3-2: Parameters of the cables used for Fig. 3-4 computations [72].

Parameter	Value		
Conductor cross-sectional area (mm^2)	800	1000	2000
Dc resistance at 20℃ (Ω/m)	2.259×10^{-5}	1.807×10^{-5}	0.904×10^{-5}
Dc resistance at 90℃ (Ω/m)	2.881×10^{-5}	2.305×10^{-5}	1.152×10^{-5}
Conductor material	Copper		
Conductor material resistivity (ρ) ($\Omega \cdot$ m)	1.7719×10^{-8}		
Copper temperature coefficient (α) ($1/$℃)	3.93×10^{-3}		
XLPE relative permeability	1		
Permeability of free space (μ_0) (H/m)	$4\pi \times 10^{-7}$		

the magnitude of the ac resistance of a conductor from a low frequency, e.g., 10 Hz, to the conventional 50/60 Hz. For instance, at 20 Hz, the ac resistance of the 800 mm^2 conductor is about 4% higher than its dc resistance value. However, at 60 Hz, the ac resistance of the same conductor would be 20% larger than the dc resistance value. The plots in Fig. 3-4 also show that the variation increases as the cross-sectional area of the conductor becomes larger. For instance, at 20 Hz, the ac resistance of the 1000 mm^2 conductor is about 5% higher than its dc resistance, and the increase is around 15% for the 2000 mm^2 conductor. On the other hand, at 60 Hz, the ac resistance of the 1000 mm^2 conductor would be approximately 30% higher than the dc resistance, and the increase would be around 72% for the 2000 mm^2 conductor.

Furthermore, although (3-11) shows that r_{dc} is a function of temperature, where r_{dc0} is

$$r_{dc} = r_{dc0}(1 + \alpha\Delta T) \tag{3-11}$$

the measured dc resistance at standard testing temperature (typically 20℃), α is the conductor material temperature coefficient, and ΔT is the temperature change, the ratio r_{ac}/r_{dc} is independent of temperature as there is no noticeable difference between the line plots for the results at 20℃ and 90℃ cable temperatures. Therefore, as shown in Fig. 3-4 charts, the contribution of skin effect to ac resistance value can be said to be independent of temperature. In conclusion, it has been determined that LF-HVac transmission would have the advantage of reduced conductor resistance in comparison to conventional HVac transmission. This feature would contribute to reduced transmission losses and smaller impedance magnitude for LF-HVac transmission than for equivalent HVac transmission.

3.3.2. Impact of Skin Effect on Inductive Reactance

Equation (3-12), which is the imaginary part of the complex number of which (3-10) is the real part, represents the equivalent reactance of a conductor due to skin effect-influenced internal flux linkages within the conductor alone [70]; where x_{dc} is the reactance due to the internal flux, assuming uniform current distribution.

$$x_{ac} = x_{dc}\frac{ma}{2}\frac{M_0(ma)}{M_1(ma)}\sin(\theta_0(ma) - \theta_1(ma) + \frac{3\pi}{4}) \tag{3-12}$$

The tendency of skin effect is to push current towards the surface of a conductor. Consequently, there will be less internal flux linkages in the conductor for an ac current than if the current were dc. Effectively, the inductance, and in essence the reactance, due to conductor internal flux linkages alone should decrease as frequency increases. However, studies have shown that reactance due to internal flux linkages is a minor component of the overall reactance of a conductor [70]. Therefore, skin effect has negligible impact on the inductive reactance of a conductor. Thus, the reactance of a LF-HVac transmission line can be approximated, to a high degree of accuracy, from the HVac line data by scaling it with the applicable frequency ratio. For instance, at 20 Hz LF-HVac operation, the conductor inductive reactance would be one-third of the value at 60 Hz HVac operation.

3.4. Impact of Frequency on the Current Carrying Capacity of Cables

The plots in Fig. 2-2, Chapter 2, compare the power transfer capacity, as a function of transmission distance, of power cables under LF-HVac and HVac operation. For those results, it was assumed that the cables have the same current rating across the operating frequencies considered. However, the preceding section of this chapter has shown that skin effect plays a

significant role in the magnitude of the ac resistance of a conductor. It becomes even more apparent as the cross-sectional area of the conductor becomes larger. Therefore, this section presents an investigation into the impact of ac operating frequency on the current carrying capacity of power cables. Note that this study only considers the static current rating of power cables, i.e., the cables are assumed to be continuously loaded at the applicable current rating(s). However, given the intermittent nature of wind, studies have been carried out to determine the dynamic rating of export cables for offshore wind farms [24], [73]. The dynamic current rating approach, which makes use of a thermal ladder network of the cable and is further validated by finite element method (FEM) simulations, often results in smaller size cables being needed since the intermittent loading would not allow the operating temperature to exceed the maximum 90℃ temperature stipulated for XLPE cables. However, the investigation of a cable dynamic current rating for LF-HVac is not within the scope of this thesis.

3.4.1. Three-core XLPE Cable Thermal Equivalent Circuit

The thermal equivalent circuit of a three-core XLPE cable is shown in Fig. 3-5 [72]. It mirrors an electric circuit. However, it only represents the heat transfer model of the cable. Nodes T_c, T_s, T_a, and T_e are the temperatures of the conductor, sheath, armour, and the cable external surface, respectively. The current source symbols W_c, W_s, and W_a represent the heat losses in the conductor, the shield, and the armour, respectively. The resistor symbols represent thermal resistances of parts of the cable, where R_{th1} is the thermal resistance between one conductor and the sheath, R_{th2} is the thermal resistance between the sheath and the armour, and R_{th3} is the thermal resistance of the external serving of the cable. A fourth thermal resistance

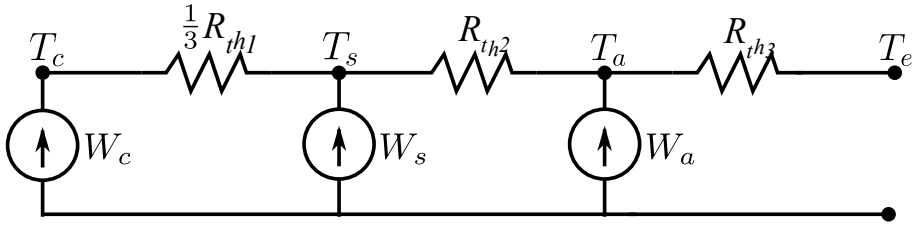

Fig. 3-5: Thermal equivalent circuit of a three-core XLPE cable.

Table 3-3: Definition of variables or symbols in the Thermal Resistances Formulae: (3-13) − (3-16) [74].

Symbol	Definition	Unit
ρ_i	Thermal resistivity of cable insulation	K.m/W
t_i	Thickness of insulation to sheath	mm
ρ_f	Thermal resistivity of the cable filler	K.m/w
G	Geometric factor for cables with separate sheaths	-
ρ_{sv}	Thermal resistivity of outer serving or jacket of cable	K.m/W
ρ_{sb}	Thermal resistivity of seabed or soil	K.m/W
L	Burial depth of cable	mm

R_{th4}, not shown in Fig. 3-5, is the thermal resistance between the cable surface and its surrounding medium. Equations (3-13) to (3-16)

$$R_{th1} = \frac{\rho_i}{2\pi}\ln\left(1+\frac{2t_i}{d_c}\right) \tag{3-13}$$

$$R_{th2} = \frac{\rho_f}{6\pi}G \tag{3-14}$$

$$R_{th3} = \frac{\rho_{sv}}{2\pi}\ln\left(\frac{D_{os}}{d_a}\right) \tag{3-15}$$

$$R_{th4} = \frac{\rho_{sb}}{2\pi} \ln\left(\frac{2L}{D_{os}} + \sqrt{\left(\frac{2L}{D_{os}}\right)^2 - 1}\right) \tag{3-16}$$

are used to determine the values of the thermal resistances [73], [72], [74], [75]. The variables in those equations are defined in Table 3-3. The mathematical expression for G is given in Appendix B.

3.4.2. Static Current Rating of Power Cables

Equation (3-17), provided by the IEC Standard 60287 [74], [75], is used to calculate the current rating I_c of a three-core XLPE cable at 100% load factor. The symbols and variables in the equation are defined in Table 3-4. Mathematical expressions for some of the terms are

$$I_c = \sqrt{\frac{\Delta T - W_d\left[\frac{1}{2}R_{th1} + n(R_{th2} + R_{th3} + R_{th4})\right]}{R_{ac}(R_{th1} + n(1+\lambda_1)R_{th2} + n(1+\lambda_1+\lambda_2)(R_{th3} + R_{th4}))}} \tag{3-17}$$

presented in Appendix B. To determine the impact of ac operating frequency on the current rating of power cables, an 800 mm^2 three-core XLPE cable is used as a test case. The cable parameters are presented in Table 3-5 and Table 3-6 [71]. In Table 3-6, ρ_E is the electrical resistivity, α is the temperature coefficient, ρ_T is the thermal resistivity, ϵ_r is the relative permittivity, and μ_r is the relative permeability. Please refer to Table 3-1 for the cable's geometric identifiers.

Table 3-4: Definition of variables and symbols in the cable current rating equation: (3-17) [74], [75].

Symbol	Definition	Unit
ΔT	Conductor temperature rise above ambient temp.	℃
W_d	Dielectric losses in the insulation	W/m
n	Number of conductors in the cable, i.e., $n = 3$	-
R_{ac}	Electrical resistance of the conductor at 90℃	Ω/m
λ_1	Loss factor of cable shield, plus the screen	-
λ_2	Loss factor of armour	-

Table 3-5: Geometric parameters of the 800 mm^2 three-core XLPE cable [71].

Layer	Material	Dimension (mm)
Conductor	Copper (stranded)	$d_c = 34.8$
Conductor screen	PE	$d_{cs} = 38.8$
Insulation	XLPE	$d_i = 72.8$
Sheath	Lead	$d_s = 82.2$
Oversheath	Medium density PE (MDPE)	$d_{os} = 87.2$
Filler	PP	$d_f = 189$
Armour bedding	PP yarns	$d_b = 194$
Armour	Steel	$d_a = 206$ (mean diameter)
Armour wires	Steel	$d_{aw} = 6$ $n_{aw} = 98$ (number of armour wires)
Outer serving	PP yarns	$D_{os} = 212$

Table 3-6: Electrical and thermal parameters of the 800 mm^2 three-core XLPE cable [71].

Layer	$\rho_E\ (\Omega \cdot m)$	α (1/°C)	$\rho_T\ (K \cdot m/W)$	ϵ_r	μ_r
Conductor	1.7241×10^{-8}	0.00393	-	-	1
Conductor screen	-	-	3.5	-	1
Insulation	-	-	3.5	2.5	1
Insulation screen	-	-	3.5	-	1
Sheath	2.14×10^{-7}	0.004	-	-	1
Oversheath	-	-	3.5	2.5	1
Filler	-	-	3.5	2.2	1
Armour bedding	-	-	3.5	2.2	1
Armour	1.38×10^{-7}	0.0045	-	-	200
Outer serving	-	-	3.5	2.2	1

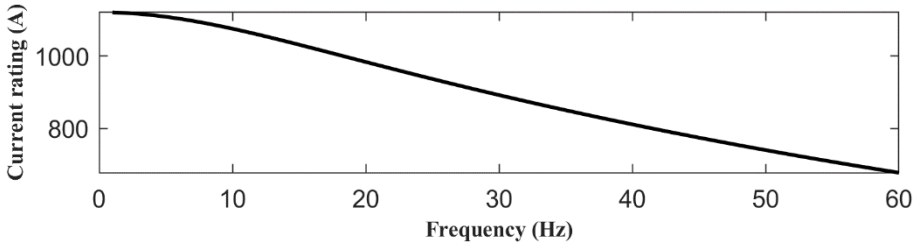

Fig. 3-6: Current rating vs. frequency plot for the 800 mm^2 three-core XLPE cable, determined using (3-17).

The graph in Fig. 3-6, generated by the author using (3-17), shows the variation of the static current rating of the test case 800 mm^2 three-core XLPE cable with operating frequency. The plot shows that operation at frequencies below the conventional 50/60 Hz would increase the

continuous current rating of the cable while maintaining the cable-specified thermal limit. For instance, at 20 Hz operation, the cable would carry 31% more current than at 50 Hz, and 43% more current than at 60 Hz. The plot shows the lower the frequency, the higher the static current rating. By looking at (3-17), the reader would appreciate this assertion. Note that the most important quantity in that equation is the magnitude of the ac resistance, R_{ac}. In this chapter, it has already been demonstrated that due to skin effect, the value of R_{ac} is significantly smaller at lower operating frequency than if the same conductor had to transfer power at the conventional HVac frequency value of either 50 or 60 Hz. Thus, this feature is noted as an advantage of LF-HVac over HVac. Consequently, at the same voltage level, the real power transfer capacity performance results for LF-HVac transmission would be better than those shown in the charts of Fig. 2-2, which was generated using uniform current rating across the operating frequencies considered.

3.4.3. Impact of Frequency on Export Cable Losses

The plots in Fig. 3-7 show the dielectric, the sheath, the armour, the conductor, and the total losses, per km, in the 800 mm^2 three-core XLPE test case cable for a range of operating frequencies, i.e., 1 to 60 Hz. The plots in Fig. 3-7, chart (a), were computed using the static current rating of the cable determined at the applicable operating frequency. In effect, the results show losses for different power transfer magnitudes. On the other hand, the plots in Fig. 3-7, chart (b), were computed using the static current rating of the cable determined at 60 Hz. In effect, the results show losses for the same magnitude of power transfers. Note that the rated line-to-line voltage of the cable is 150 kV. The bar graph in Fig. 3-8 visually compares the total and the different kinds of losses in the test case cable for operation at 10, 20, 35, 50, and 60 Hz,

and at the applicable frequency-determined continuous current rating. The line plots in Fig. 3-7 show that for most of the frequency range, conductor losses are the predominant losses encountered in the cable system. It is readily observed in Fig. 3-7 (a) and Fig. 3-8 that the magnitude of conductor losses is higher at lower frequency values than at higher frequency values. However, this should not be of concern since at lower LF-HVac operating frequency the cable would support larger continuous current flow than at 50/60 Hz, for example. The charts in Fig. 3-7 and Fig. 3-8 also show that for most of the frequency range, sheath losses are the second highest losses after conductor losses. However, unlike conductor losses, sheath losses grow

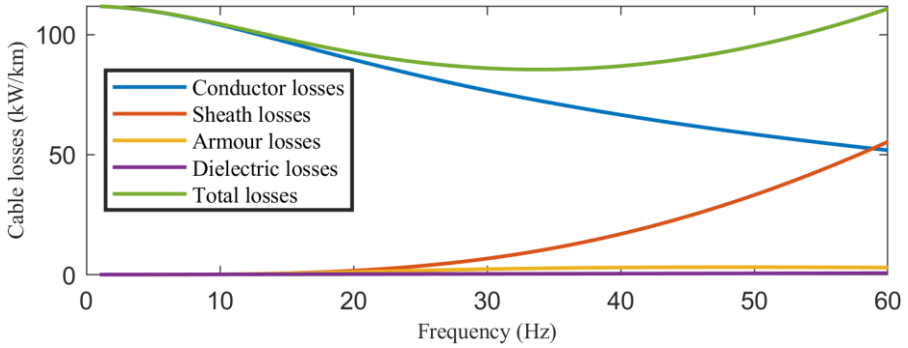

(a)

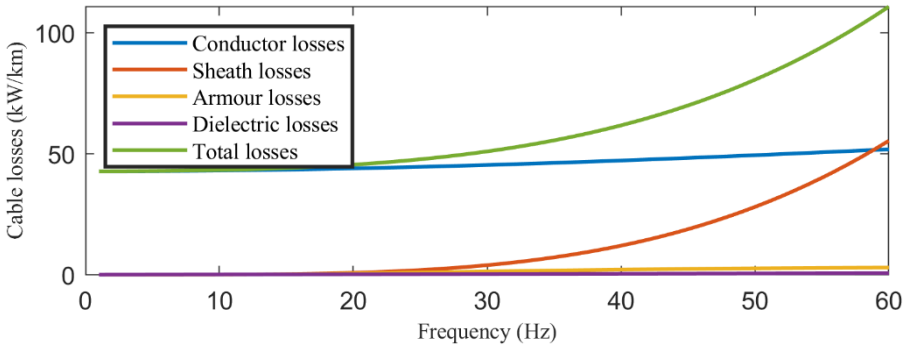

(b)

Fig. 3-7: Losses, per km, in the 800 mm^2 three-core XLPE cable, with respect to ac operating frequency; (a): current = frequency-applicable current rating, (b): current = current rating at 60 Hz.

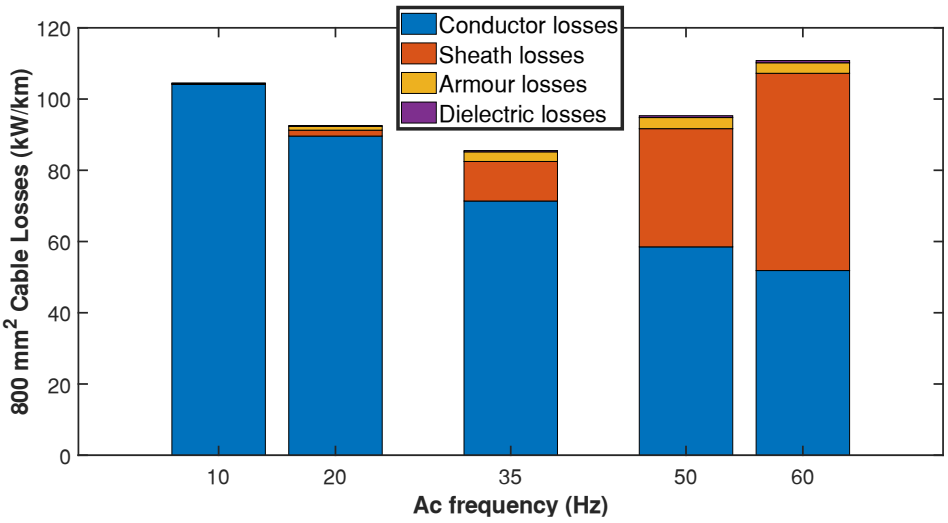

Fig. 3-8: Bar chart of the losses, per km, in the 800 mm^2 three-core XLPE cable for operation at 10, 20, 35, 50 and 60 Hz; current = frequency-applicable current rating of the cable.

almost exponentially as the cable operating frequency is increased. At 60 Hz, sheath losses are even larger than conductor losses. Armour losses and dielectric losses are also higher at higher operating frequency values than at lower ones. However, the increases are not exponential like sheath losses. Furthermore, the magnitudes of armour and dielectric losses are significantly less than those of conductor and sheath losses, with dielectric losses being the lowest of the lot.

The charts in Fig. 3-7 (a) and Fig. 3-8 also provide information about the total losses that could be encountered in the cable at different operating frequency values, and at the applicable continuous current rating. The "Total losses" curve in Fig. 3-7 (a) and the bar charts in Fig. 3-8 show that for the given frequency range, there exists a minimum magnitude of total losses in the cable. This would occur when the cable is operated at the applicable continuous current rating of approximately 35 Hz. However, assuming the same voltage level, and uniform voltage and current magnitudes across the cable length, note that maximum power transfer capacity at the frequency-applicable continuous current rating is not the same across the 1-60 Hz frequency range. The graph in Fig. 3-9 shows this. For example, at 20 Hz LF-HVac operation, the 800

mm^2 three-core XLPE cable could transfer 30% more active power than when the cable is operated at 50 Hz HVac. Furthermore, at 20 Hz LF-HVac operation, the cable system could transfer 43% more power than when operated at 60 Hz HVac. For a 50 km 150 kV 800 mm^2 three-core XLPE cable system, the total losses in the cable, as a percentage of the frequency-applicable maximum power at the sending terminal, are presented as a curve for the 1-60 Hz frequency range in Fig. 3-10. The plot shows an almost exponential relationship, increasing with frequency, between the fractional proportion of losses, expressed in percentage, that would be encountered through the length of the cable in the maximum power that could be dispatched into the system at the sending terminal.

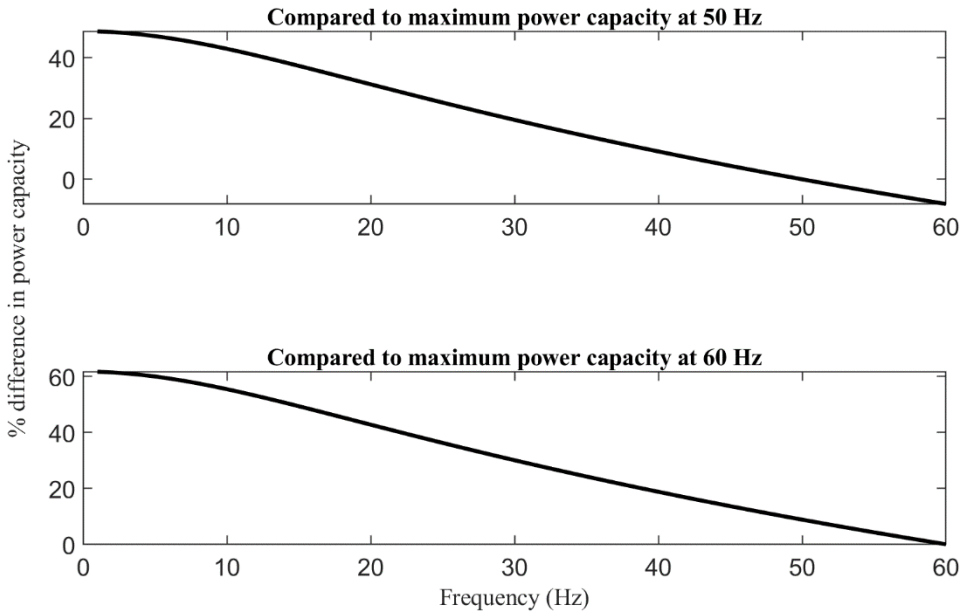

Fig. 3-9: Percentage difference plots for the maximum power capacity of the cable at a given operating frequency when compared to the capacity at 50 Hz and 60 Hz.

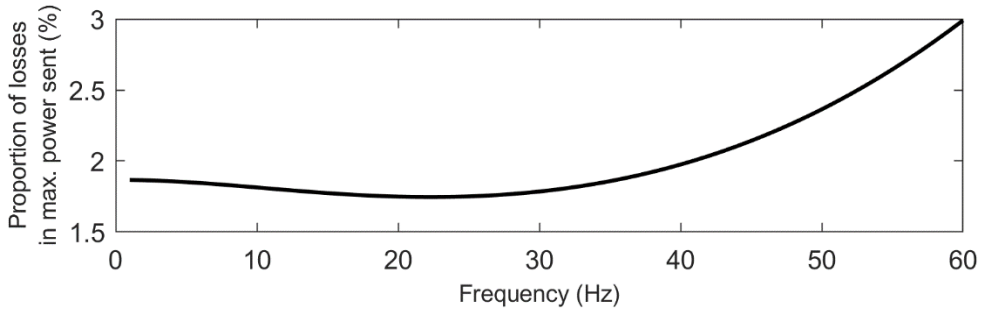

Fig. 3-10: Proportion of losses in the maximum power dispatched into the cable at the sending end of a 50 km 150 kV 800 mm^2 three-core XLPE cable system.

The plot in Fig. 3-10 shows that operation at LF-HVac would transfer more power in the cable in comparison to HVac, as previously determined, while recording less percentage losses than HVac. For instance, at 20 Hz LF-HVac operation, the total losses in the cable would be less than 1.8% of the maximum power capacity of the cable at 20 Hz. On the other hand, at 60 Hz HVac operation, the same cable system would encounter total losses equivalent to 3% of its maximum power capacity at 60 Hz. Simply put, a 20 Hz LF-HVac 150 kV 800 mm^2 three-core cable system could transfer 43% more power than a similar 60 Hz HVac system, while only registering total cable losses equivalent to 1.75% of its maximum power capacity. Contrast this to the 60 Hz HVac system, which would accumulate cable losses equivalent to 3% of its much-reduced maximum power capacity.

3.5. Summary

This chapter explored the implications of using lower than the conventional 50/60 Hz operating frequency for ac transmission in commercially available XLPE submarine cables. The presented study has identified the phenomenon of skin effect as having the most consequential impact when export cables are operated under the LF-HVac scheme. The reduction in the

magnitude of the ac resistance would directly increase the cable's current carrying capacity, which would in turn increase the power handling capacity of the cable. Note that the same voltage level has been assumed for this assertion. Furthermore, LF-HVac operation would also have the feature of reducing the total losses encountered while transmitting significantly more power in the cable system, when compared to the same cable system operated under the conventional HVac scheme.

Chapter 4

V/f Controlled LF-HVac Transmission: Theory and Fit for the Grid Integration of Offshore Wind

4.1. Introduction

The review and discussions presented in Chapter 2 indicate that, at the same voltage and power level, magnetically coupled electric circuits that are to be used in LF-HVac transmission, especially the transformer, would be larger and heavier than their equivalent HVac counterparts. Recall that, as (2-4) indicates, the peak flux density B in the transformer core is inversely proportional to the ac frequency f. Thus, the only way to maintain the peak flux density, while the ac frequency is reduced, would be to increase the core area A and/or the number of turns N. For example, Fig. 2-11 in Chapter 2 graphically illustrates how the dimensions and the weight of two extreme designs of a 16.67 Hz 132/33 kV LF-HVac transformer would compare to those of an equivalent 50 Hz HVac transformer. On the other hand, the peak flux density is proportional to voltage E (or V). Therefore, the peak flux density in a given transformer core can be maintained by adopting a constant V/f ratio in the adjustment of either V or f.

Furthermore, wind energy is intermittent and non-dispatchable. This means that naturally variable wind speed would, in the same manner, affect the power output of a turbine. For example, unlike a thermal power plant, wind power cannot be switched on nor ramped up on demand. Thus, in providing solutions to the research questions posited in Chapter 2, section 2.7, the work presented in this chapter demonstrates how the implementation of V/f control in the

LF-HVac transmission of offshore wind energy could maximize the amount of real power imported into the grid for any given OWPP output level. The study presented in the preceding chapter shows the export cable system electrical performance over a wide range of ac operating frequency, i.e., 1-60 Hz. However, for a feasible design, the LF-HVac variable frequency range would have to be much more limited than that, as will be discovered in this chapter.

This chapter begins with a discussion on the concept of V/f control in LF-HVac transmission for the grid integration of offshore wind. Then the focus shifts to the steady-state model, analysis, and performance characteristics of the export cable in LF-HVac transmission. Analysis of the model ensues, which includes study of the real power transfer capacity, plus the applicable reactive power, and the voltage and current profile characteristics of the export cable during LF-HVac transmission.

4.2. V/f Controlled LF-HVac Transmission

This section demonstrates, with the objective of maximizing power transfer to the grid while repurposing 50 Hz rated power transformers and reactors, the technical fit between the proposed V/f controlled LF-HVac transmission and the energy output characteristics of offshore wind. The literature review undertaken in preparation for this thesis shows that the studies on LF-HVac transmission have typically tended to be more theoretical than practical. For example, as mentioned in section 2.7 of Chapter 2, several studies referenced in that chapter have selected either 16.67 or 20 Hz as the nominal LF-HVac operating frequency. However, little or no information had been provided to support the choice of either value as the ac operating frequency. Furthermore, the studies did point out that LF-HVac transformers would be larger and heavier than equivalent HVac transformers. At this juncture, it is important to note that either

16.67 or 20 Hz power transformers are not commercially available. Therefore, there may be unforeseen technical, manufacturing, and logistical challenges that could hinder the acquisition of those transformers for the proposed LF-HVac transmission scheme. On the other hand, this thesis adopts the approach of proposing and demonstrating how transformers originally designed for operation at 50 Hz HVac could be repurposed, using the equipment applicable V/f derating factor, in the V/f controlled LF-HVac transmission scheme for offshore wind. The following subsections would explore the technical arguments for this approach.

4.2.1. Wind Turbine Power Output Characteristics

In this sub-section, the link between the variability of wind speed and the energy output characteristics of a wind turbine would be established. Equation (4-1) is the mathematical expression for the mechanical power harnessed from wind by a variable speed wind turbine [76], [77], [78]. Table 4-1 presents the definitions of the variables used in the equation. Equation (4-2) gives the mathematical expression for the turbine performance coefficient C_p, while (4-3) gives the formula for λ_i.

$$P_t = \frac{\rho_t \pi {R_t}^2}{2} C_p(\lambda_t, \beta_t) v^3 \tag{4-1}$$

$$C_p(\lambda_t, \beta_t) = 0.5176 \left(\frac{116}{\lambda_i} - 0.4\beta_t - 5\right) \mathrm{e}^{\left(-\frac{21}{\lambda_i}\right)} + 0.0068\lambda_t \tag{4-2}$$

$$\frac{1}{\lambda_i} = \frac{1}{\lambda_t + 0.08\beta_t} - \frac{0.035}{\beta_t^3 + 1} \tag{4-3}$$

Table 4-1: Parameters for calculating wind power output of an 8 MW rated wind turbine [76], [77], [78].

Parameter	Definition	Value/Unit
ρ_t	Air density	1.225 kg/m^3
R_t	Turbine radius	83.5 m
$C_p(\lambda_t, \beta_t)$	Turbine performance coefficient	(4-2)
v	Wind speed at hub height	m/s
ω_t	Turbine angular speed	rad/s
λ_t	Tip speed ratio: $\lambda_t = \frac{\omega_t R_t}{v}$	rad
β_t	Turbine blades pitch angle	0 deg.

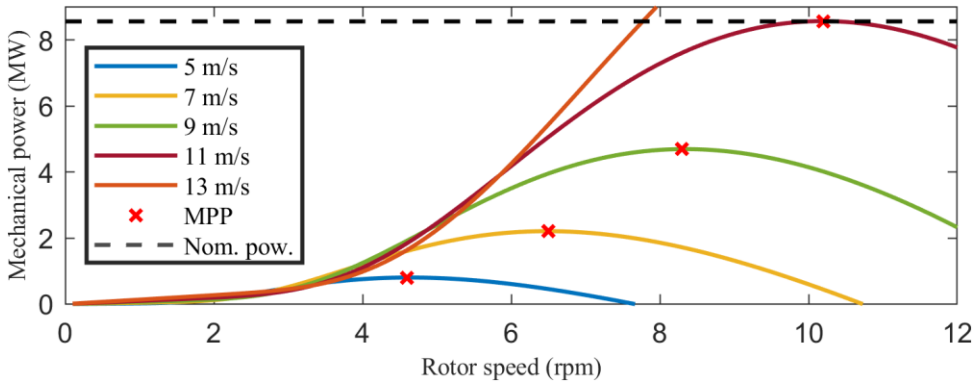

Fig. 4-1: Mechanical output power vs. rotor speed curves of the 8 MW rated wind turbine, whose parameters are listed in Table 4-1. "Nom. pow." is short for nominal power.

Fig. 4-1 shows the mechanical output power vs. rotor speed curves, for a set of wind speeds, of an 8 MW (nominal power rating) variable speed offshore wind turbine, whose parameters are listed in Table 4-1. The curves are generated, by the author, using (4-1)-(4-3). The line plots show the typical power output characteristics of a wind turbine. For example, at each prevailing wind speed there exists a maximum output power, termed the maximum power point (MPP). The

wind turbine MPPT (MPP tracking) control algorithm is applied to ensure that the maximum power is harnessed from the wind at each prevailing wind speed [77]. The chart in Fig. 4-2 shows the typical power output characteristics curve of a wind turbine in the presence of varying wind speeds. At the cut-in speed, usually around 4 m/s [79], the turbine blades would start to rotate, thus, power generation would start. So, following the MPPT curve for the increasing wind speed (see Fig. 4-1), the power harnessed by the turbine would increase accordingly up to the rated nominal speed/power. In Fig. 4-2, this occurs at 11 m/s and 8.5 MW rated nominal values. For wind speeds above the rated nominal value(s), the turbine would maintain the rated nominal output power, up to the cut-out wind speed of typically 25 m/s [79]. Above this wind speed point, the turbine would shut down to protect the plant.

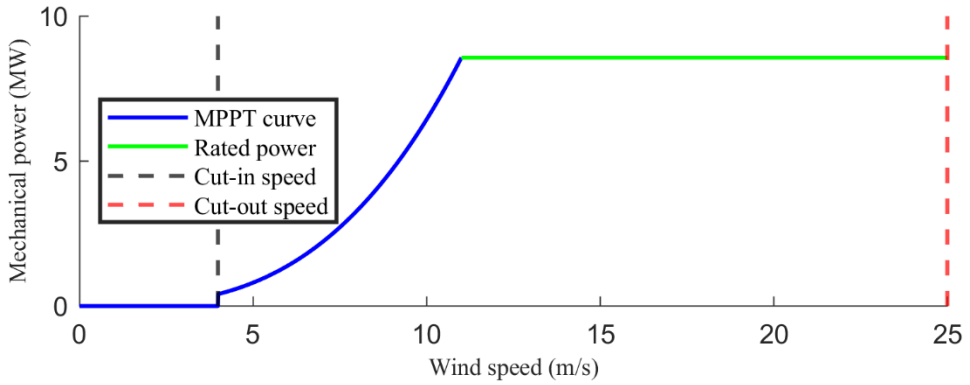

Fig. 4-2: Wind turbine power output characteristics curve.

From this discussion, therefore, two distinct regions of operation of a turbine can be identified in the chart presented in Fig. 4-2. The first one is the MPPT curve where the turbine operates between the cut-in wind speed and the rated nominal wind speed. The second region of operation is between the point the rated nominal wind speed is attained and the cut-out wind speed point. Nevertheless, due to wide variability of wind speeds, a wind turbine would rarely

operate at its rated nominal power [80]. Of course, a wind farm is a collection of tens of turbines distributed over an area which could be as large as a mid-size North American city. For instance, the Hornsea One offshore wind project discussed in Chapter 2 has 174 turbines spread over an area of 407 km^2 [46]. Therefore, over a given period each turbine would likely produce its own unique set of power outputs. Consequently, the sum of the power produced by the wind farm, like each individual turbine, would be a variable quantity, dependent on the wind characteristics at the given time, the day, or the season. Hence, in planning an offshore wind installation it is important to not only provide adequate export capacity for the wind farm rated power, which is rarely achieved, but to consider means of maximizing the net energy imports into the grid even as the wind farm output power varies over the applicable production range.

4.2.2. V/f Control Operation

This sub-section discusses the fundamentals behind the V/f controlled LF-HVac transmission scheme for offshore wind. It concludes with a basic example demonstrating the concept, highlighting how V/f control could reduce charging current losses while boosting active power delivery to the grid. From the preceding sub-section, it could be understood that a wind farm would rarely operate at its rated output power. Rather, depending on hourly, daily, and seasonal wind variabilities, the power output of a wind farm would fluctuate within an operational design range. Thus, the real challenge is in providing the export means that would deliver the most amount of real power (while minimizing losses due to charging current in the cable), relative to the applicable wind energy output, to the point of interconnection (POI) between the wind installation and the grid. In the discussions in Chapter 2, charging current is identified as an important quantity which puts a limit on the amount of real power that could be

transmitted via a cable system. Therefore, given that charging current is proportional to frequency, LF-HVac transmission has been proposed as a means of curtailing losses associated with this quantity, while increasing the power transfer capacity of the export cable system. As previously mentioned, at the same voltage and power level as conventional HVac transmission systems, LF-HVac power transformers and reactors would have to be larger and heavier than their HVac counterparts to avoid over fluxing in their cores.

However, as (2-5) shows, repeated below as (4-4), voltage magnitude V is a more

$$P_R = \sqrt{S^2 - 4\pi^2 f^2 C^2 V^4 l^2} \tag{4-4}$$

consequential quantity than frequency f, since its exponent is twice that of the latter, when it comes to maximizing the amount of real power that could be exported via a cable system to the grid POI. In addition, this feature provides a solution to the identified problem of LF-HVac that would require its transformers and reactors to be larger and/or heavier than those of equivalent HVac equipment to maintain the applicable flux to feasible level(s). Thus, with the application of V/f control, a commercially available 50 Hz rated transformer/reactor could be derated using the equipment applicable V/f ratio for use in LF-HVac transmission of offshore wind energy. For instance, a 380 kV (HV side) transformer designed for 50 Hz nominal frequency operation could be derated by the V/f ratio of 7.6 to operate at 220 kV voltage/29 Hz frequency set of nominal operating values.

Recall that, as graphically illustrated in Fig. 2-4, some planned offshore wind farms could be sited well over 100 km (even up to 200 km) away from the shore. As discussed in Chapter 2, experience from the Hornsea One project has shown that the only way the conventional (50 Hz) HVac transmission scheme could be applied in the wind energy export of such remote offshore wind farms would be through the use of intermediate offshore reactive compensation [46].

Without the intermediate offshore reactive compensation station(s), the active power being delivered to the grid would be dissipated by the relatively high charging current losses in the export cable. On the other hand, for the V/f controlled LF-HVac transmission scheme, (4-4) suggests that even with the applicable V/f derating applied, beyond a certain transmission distance l, the active power P_R delivered by a lower V/f parameters set would exceed that delivered by a much higher V/f parameters set. HVdc, an alternative to HVac transmission, could be applied in the grid integration of remote offshore wind farms. However, HVdc transmission scheme would require a converter station to be sited offshore. Therefore, if offshore siting of power equipment and/or converter station(s) would not be economically viable, the proposed V/f controlled LF-HVac transmission scheme could be an attractive or even the only offshore wind energy transmission option since it would involve having the minimum amount of equipment/facilities sited offshore.

Given the variability of wind, there is the important challenge of the offshore wind power export technology being able to maximize the amount of real power, relative to the wind energy output, imported into the grid. Once again, (4-4) shows that as the OWPP output power S (i.e., the apparent power) decreases, simultaneous reduction of V and f in accordance with the V/f ratio would result in a higher delivered active power compared to operation at a higher voltage and frequency parameters set. The following example provides some illustration. Consider a 162 MW rated offshore wind farm, which could be sited up to 200 km from the shore. The export cable is the 150 kV three-core XLPE cable used for case study in Chapter 3. Note that the cable is originally designed for 50 Hz HVac operation. Thus, the V/f derating factor is 3. Table 4-2 shows the cable current rating for ac operation at three frequency values: 30, 36, and 50 Hz.

Table 4-2: Cable current ratings of the 150 kV three-core XLPE cable for a V/f derating factor of 3.

Voltage/Frequency (V/f = 3)	90 kV/30 Hz	108 kV/36 Hz	150 kV/50 Hz
Cable current rating (kA)	0.93	0.88	0.78

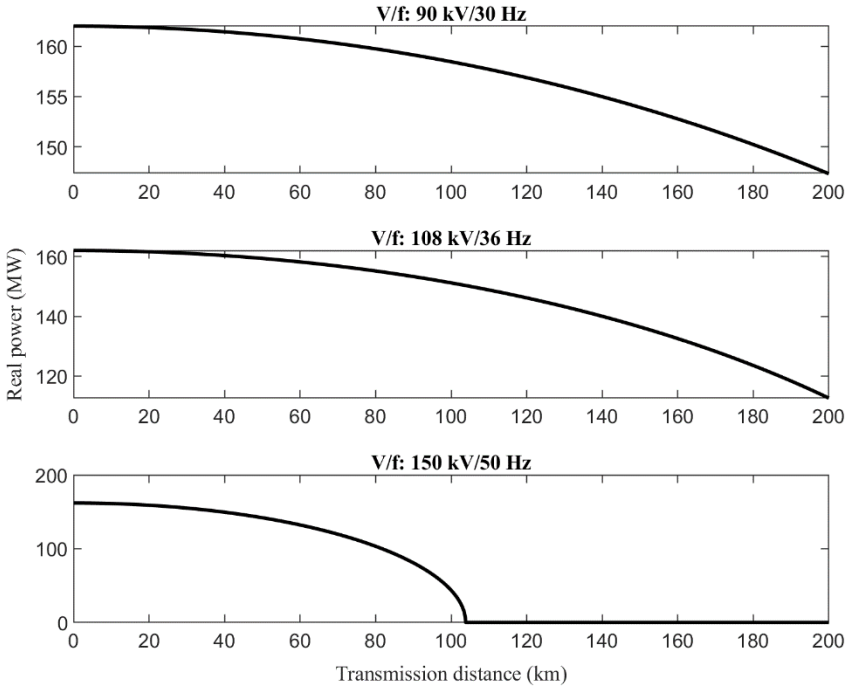

Fig. 4-3: Real power transfer vs. transmission distance plots for the V/f pairs in Table 4-2; for the wind farm rated output, i.e., 162 MW.

At the rated wind farm output power of 162 MW, Fig. 4-3 shows the real power transfer vs. transmission distance plots for the pairs of voltage and frequency values in Table 4-2. Note that neither terminal nor intermediate reactive power compensation is applied. Observation of the plots in Fig. 4-3 shows that for the V/f pair of 150 kV/50 Hz, no active power could be delivered via the export cable, when the length exceeds 104 km. For V/f = 108 kV/36 Hz, 113 MW could be delivered via the export cable, with the length = 200 km. Assuming constant current along the cable length, the current for this V/f pair when used for the ac system operation would be 0.87

kA, which is less than the applicable cable current rating shown in Table 4-2. On the other hand, still on Fig. 4-3, even though the V/f pair of 90 kV/30 Hz is shown to have delivered 147 MW to the grid via the 200 km export cable, its use for ac operation would not be feasible because the current would exceed the applicable cable current rating by 12%. Therefore, for the V/f pairs in Table 4-2, only V/f = 108 kV/36 Hz could be used to transmit active power to the grid via the 200 km long export cable.

However, for the scenario when the wind farm output is only two-thirds of its nominal rating, Fig. 4-4 shows the real power transfer vs. transmission distance plots for the same V/f pairs. Unlike in the previous scenario, the ac system operation at V/f = 108 kV/36 Hz would deliver no active power to the grid via the 200 km export cable. All the power supplied at the wind farm has been expended in the cable charging current (and other losses). On the other hand,

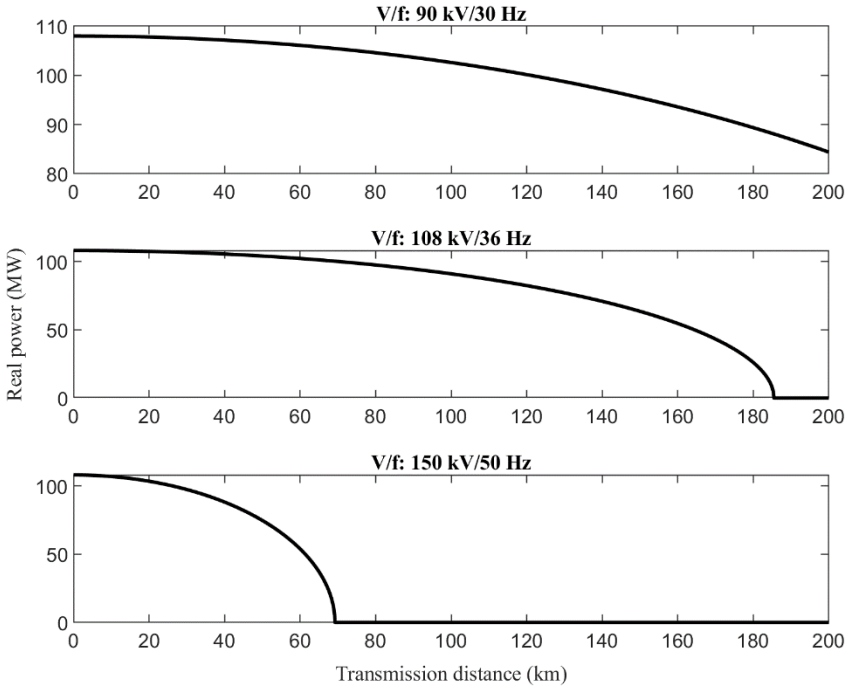

Fig. 4-4: Real power transfer vs. transmission distance plots for the V/f pairs in Table 4-2; for wind farm output = 67% of the rated power, i.e., 108 MW.

operation at V/f = 90 kV/30 Hz could deliver 84 MW to the grid for the same cable length. This example illustrates how, without any reactive compensation, the optimum V/f pair for the ac system operation, which would result in the maximum power transfer to the grid, via a given export cable, is dependent on the wind energy output. Hence, this thesis-proposed V/f controlled LF-HVac transmission scheme could, relative to the wind energy output, maximize the real power delivery to the grid from remote offshore wind farms, while repurposing existing HVac power equipment.

4.3. Steady-State LF-HVac Transmission Model for the Export Cable

As determined in Chapter 3, both the series impedance and shunt admittance parameters of a power transmission cable are influenced by the ac operating frequency quantity. Thus, this section presents the investigation on how this characteristic affects the $ABCD$ constants along the export cable length. $ABCD$ constants are the generalized circuit constants of a transmission line or cable system [5]. Furthermore, the accuracy of the constant frequency model of the export cable is also investigated. The constant frequency model ignores the impact of skin effect and assumes that RLC parameters of the cable, determined at the conventional HVac frequency of 50/60 Hz, are unchanged at lower LF-HVac operating frequencies. Fig. 4-5 shows the schematic

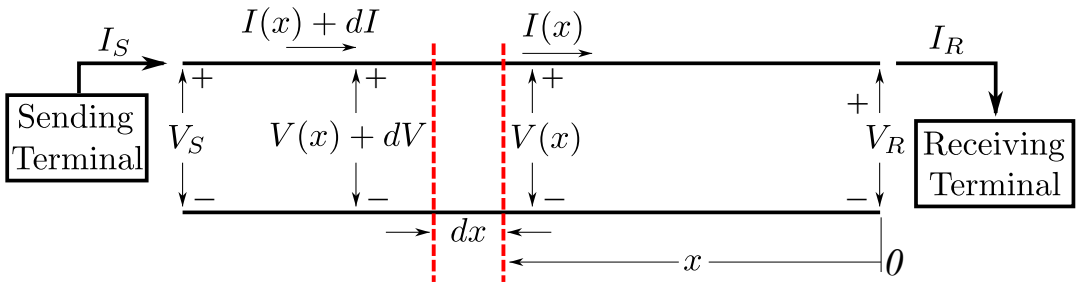

Fig. 4-5: Distributed parameters export cable representation, showing one phase and the ground or neutral return [5].

diagram of a transmission line (general term for below surface cable and overhead line), with one phase and the ground or the neutral return shown [5]. The cable parameters are uniformly distributed throughout the length of the cable. Variable x is the distance measured from the receiving terminal. For a differential element of length dx in the line, and located x km from the receiving terminal of the line, the series impedance and the shunt admittance are zdx and ydx, respectively [5]; where $z = R + j\omega L$ is the series impedance per unit length per phase, and $y = G + j\omega C$ is the shunt admittance per unit length per phase to neutral or ground. $V(x)$ and $I(x)$ in Fig. 4-5, respectively, are x-dependent voltage and current phasors. Within the elemental section, the average current is $I(x) + \frac{dI}{2}$, and the average voltage is $V(x) + \frac{dV}{2}$. Thus, the voltage increase (in the direction of the sending terminal) across the elemental distance dx is given by (4-5), with the product of the differential quantities neglected.

$$dV = \left(I(x) + \frac{dI}{2}\right) zdx = I(x)zdx = I(x)(R + j\omega L)dx \tag{4-5}$$

Similarly, the current in the elemental section is given by (4-6).

$$dI = \left(V(x) + \frac{dV}{2}\right) ydx = V(x)ydx = V(x)(G + j\omega C)dx \tag{4-6}$$

Equation (4-5) can be rewritten as (4-7), and (4-6) can be rewritten as (4-8).

$$\frac{dV}{dx} = I(x)z = I(x)(R + j\omega L) \tag{4-7}$$

$$\frac{dI}{dx} = V(x)y = V(x)(G + j\omega C) \tag{4-8}$$

On differentiating (4-7) and (4-8) with respect to x, (4-9) and (4-10), respectively, are derived [5].

$$\frac{d^2V}{dx^2} = z\frac{dI}{dx} = (R + j\omega L)\frac{dI}{dx} \tag{4-9}$$

$$\frac{d^2I}{dx^2} = y\frac{dV}{dx} = (G + j\omega L)\frac{dV}{dx} \tag{4-10}$$

Substitutions of (4-8) into (4-9) and (4-7) into (4-10) yield (4-11) and (4-12), respectively.

$$\frac{d^2V}{dx^2} = yzV(x) = [RG - \omega^2 LC + j\omega(LG + RC)]V(x) \tag{4-11}$$

$$\frac{d^2I}{dx^2} = yzI(x) = [RG - \omega^2 LC + j\omega(LG + RC)]I(x) \tag{4-12}$$

Note that in both (4-11) and (4-12), the term $yz = [RG - \omega^2 LC + j\omega(LG + RC)]$ is a function of the ac operating frequency since $\omega = 2\pi f$. Furthermore, due to skin effect, R in the term also makes it a function of frequency. The solutions to (4-11) and (4-12) are of the exponential form, where (4-13) is the solution to (4-11) and (4-14) is the solution to (4-12) [5].

$$V(x) = A_1 e^{\sqrt{yz}\,x} + A_2 e^{-\sqrt{yz}\,x} \tag{4-13}$$

$$I(x) = \frac{1}{\sqrt{\frac{z}{y}}} A_1 e^{\sqrt{yz}\,x} - \frac{1}{\sqrt{\frac{z}{y}}} A_2 e^{-\sqrt{yz}\,x} \tag{4-14}$$

At the receiving end, $x = 0$, $V = V_R$, and $I = I_R$. Substituting these values into (4-13) and (4-14), and subsequent evaluations yield the expressions for the constants A_1 and A_2: (4-15) and (4-16), respectively, where $Z_c = \sqrt{\frac{z}{y}} = \sqrt{\frac{RG+\omega^2 LC+j\omega(LG-RC)}{G^2+\omega^2 C^2}}$.

$$A_1 = \frac{V_R + Z_c I_R}{2} \tag{4-15}$$

$$A_2 = \frac{V_R - Z_c I_R}{2} \tag{4-16}$$

Z_c is termed the characteristic impedance of the export cable. Equations (4-17) and (4-18) give the expressions for $V(x)$ and $I(x)$, respectively, with A_1 and A_2 expressed in terms of V_R, I_R, and Z_c.

$$V(x) = \frac{V_R + Z_c I_R}{2} e^{\gamma x} + \frac{V_R - Z_c I_R}{2} e^{-\gamma x} \tag{4-17}$$

$$I(x) = \frac{\frac{V_R}{Z_c} + I_R}{2} e^{\gamma x} - \frac{\frac{V_R}{Z_c} - I_R}{2} e^{-\gamma x} \tag{4-18}$$

The variable γ in (4-17) and (4-18) is the propagation constant. It has the expression $\gamma = \sqrt{yz} = \sqrt{RG - \omega^2 LC + j\omega(LG + RC)}$. Rearrangement of the terms in (4-17) and (4-18) and using the hyperbolic functions $\cosh \gamma x = \frac{e^{\gamma x} + e^{-\gamma x}}{2}$ and $\sinh \gamma x = \frac{e^{\gamma x} - e^{-\gamma x}}{2}$ yield (4-19), where $A(x) = D(x) = \cosh \gamma x$, $B(x) = Z_c \sinh \gamma x$, and $C(x) = \frac{1}{Z_c} \sinh \gamma x$.

$$\begin{bmatrix} V(x) \\ I(x) \end{bmatrix} = \begin{bmatrix} A(x) & B(x) \\ C(x) & D(x) \end{bmatrix} \begin{bmatrix} V_R \\ I_R \end{bmatrix} \tag{4-19}$$

The (4-19) matrix elements $A(x)$, $B(x)$, $C(x)$, and $D(x)$ are the generalized circuit parameters of the export cable system [5].

The charts in Fig. 4-6 show the plots for the magnitude of $A(x)$ vs. transmission distance, along the 200 km length of the 150 kV 800 mm^2 three-core XLPE cable discussed in Chapter 3. The plots compare $|A(x)|$ determined using the accurate model and the constant frequency model. The plots of the error in using the constant frequency model for the determination of $|A(x)|$ are presented in Fig. 4-7. The errors are negligible. Fig. 4-8 shows the plots for the phase angle of $A(x)$. Unlike for $|A(x)|$, non-negligible errors are introduced when the constant frequency model is used, as shown in Fig. 4-9. The errors are higher at lower frequency values. Thus, it could be concluded that the constant frequency model may be used to determine $|A(x)|$ and $|D(x)|$ to a high degree of accuracy. However, significant errors would be introduced if the model is used in the computation of the phase angle, or when complex number calculations are involved. Observation of the charts in Fig. 4-6 show that $|A(x)|$ drops below unity as the cable length increases. Also, the lower the operating frequency, the closer $|A(x)|$ is to unity across the cable length.

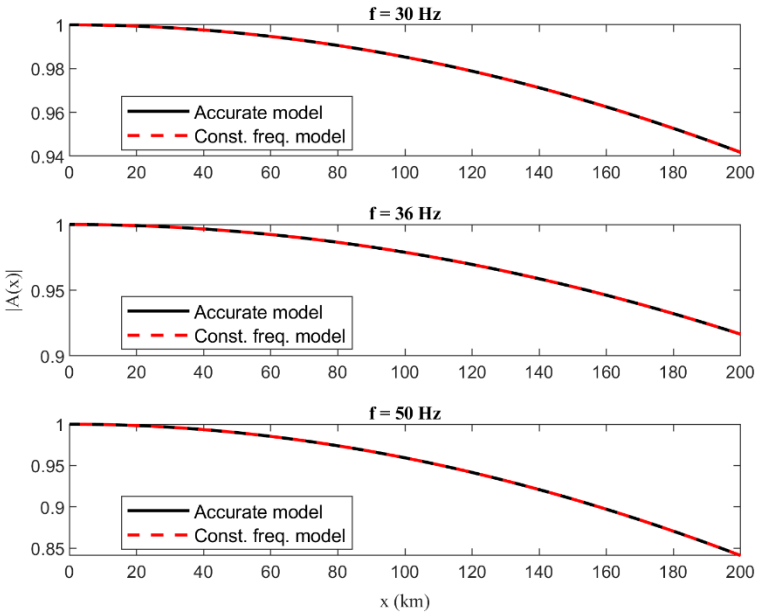

Fig. 4-6: $|A(x)|$ vs. transmission distance (i.e., x) plots along the 150 kV 800 mm^2 three-core XLPE cable length.

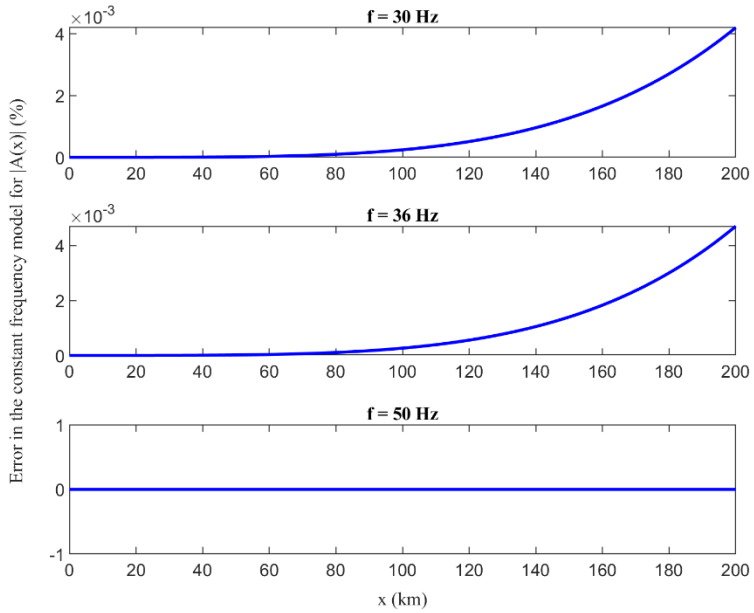

Fig. 4-7: Error in using the constant frequency model for calculating $|A(x)|$.

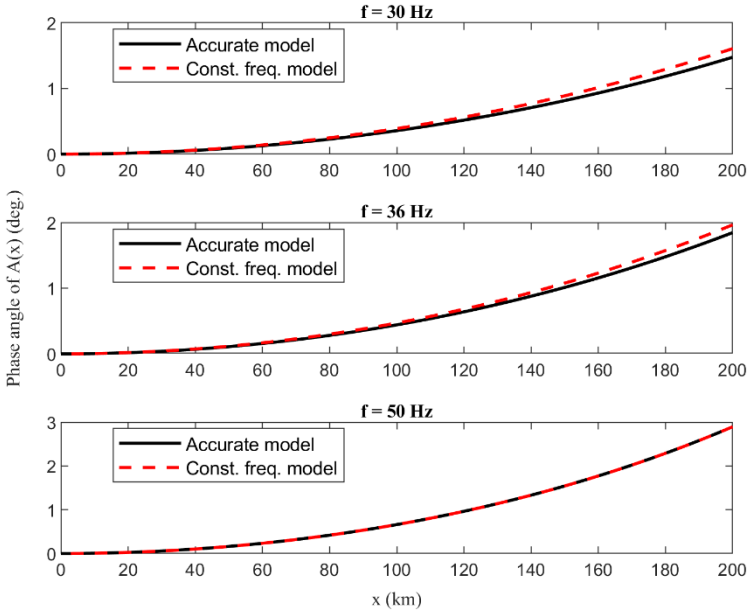

Fig. 4-8: Phase angle of $A(x)$ vs. transmission distance (i.e., x) plots along the 150 kV 800 mm^2 three-core XLPE cable length.

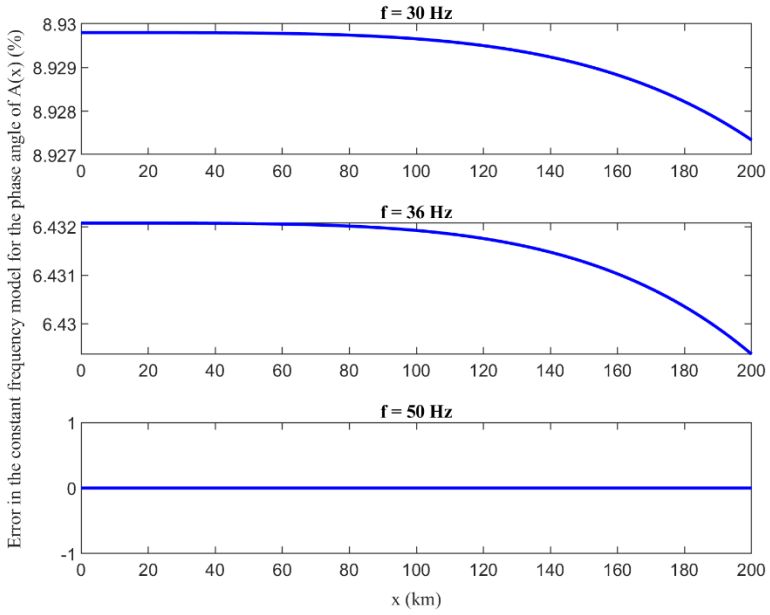

Fig. 4-9: Error in using the constant frequency model for calculating the phase angle of $A(x)$.

The charts in Fig. 4-10 show the plots for $|B(x)|$ vs. transmission distance along the 200 km run of the export cable. The plots show the lower the frequency, the lower $|B(x)|$ is along the

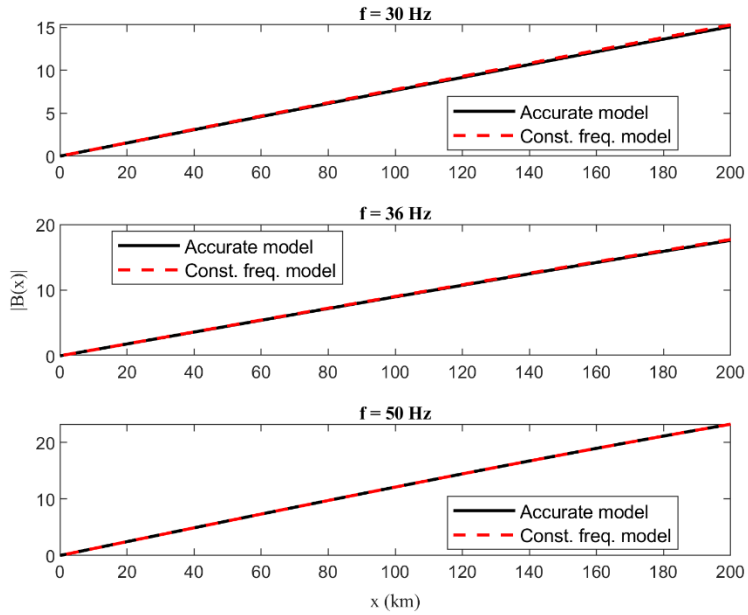

Fig. 4-10: $|B(x)|$ vs. transmission distance (i.e., x) plots along the 150 kV 800 mm^2 three-core XLPE cable length.

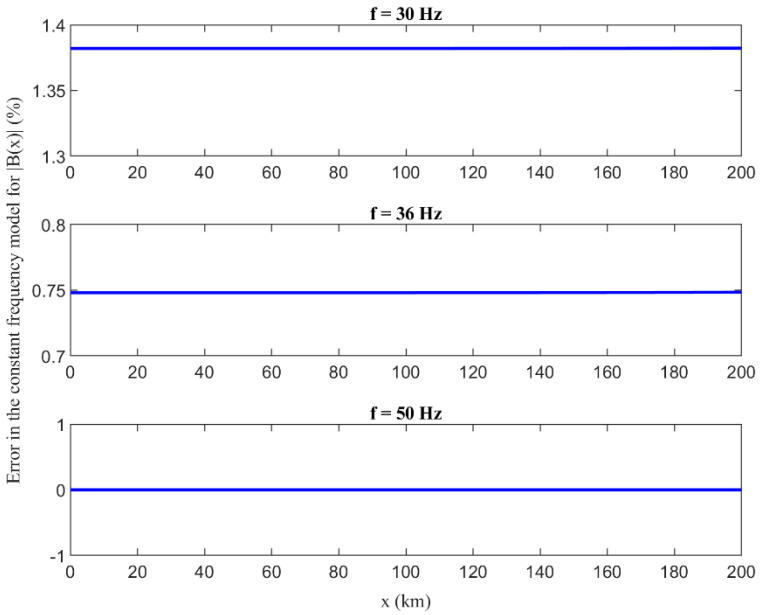

Fig. 4-11: Error in using the constant frequency model for calculating $|B(x)|$.

cable length. This observation is reasonable since $|B(x)|$ is proportional to cable impedance, which in turn is largely proportional to frequency. The plots in Fig. 4-11 show the errors, which are not negligible, when the constant frequency model is used to determine $|B(x)|$. The error would get larger as the operating frequency is lowered, up to 1.5% for f = 30 Hz. This figure may not seem drastic but consider that at 20 Hz, the error would be around 5% and over 10% at 10 Hz. Fig. 4-12 and Fig. 4-13 show the charts for the phase angle of $B(x)$, and the error introduced in its determination when the constant frequency model is used. The errors are not negligible. Therefore, these observations lead to the conclusion that the constant frequency model should not be used to determine $|B(x)|$ and the phase angle of $B(x)$ in LF-HVac calculations.

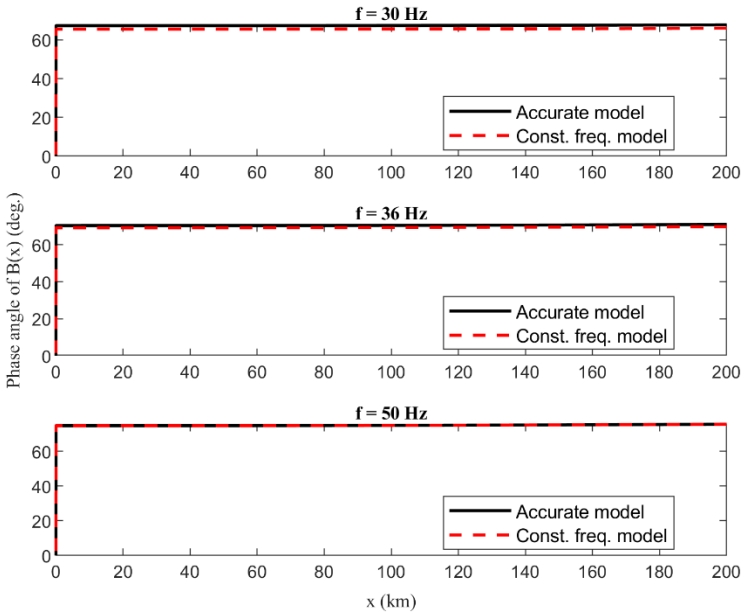

Fig. 4-12: Phase angle of $B(x)$ vs. transmission distance (i.e., x) plots along the 150 kV 800 mm^2 three-core XLPE cable length.

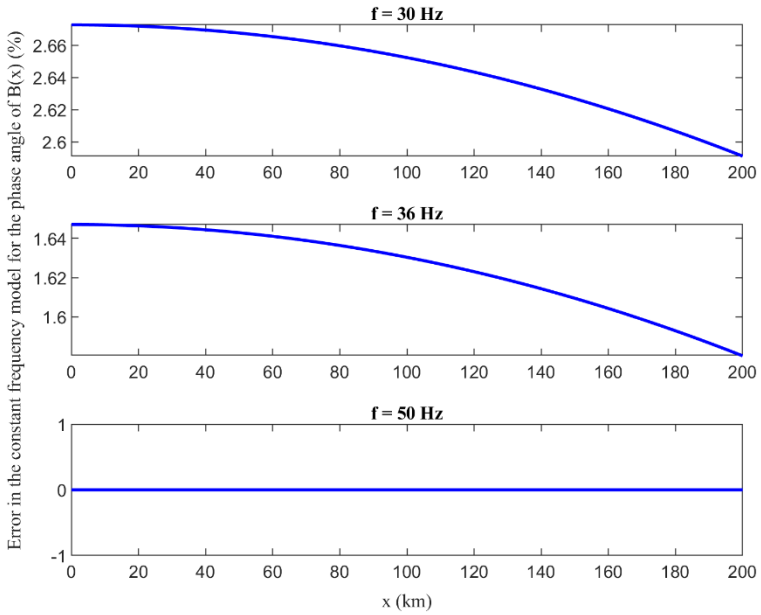

Fig. 4-13: Error in using the constant frequency model for calculating the phase angle of $B(x)$.

The charts in Fig. 4-14 show the plots for $|C(x)|$ vs. transmission distance along the 200 km run of the export cable. The corresponding error plots when the constant frequency model is used to determine $|C(x)|$ are shown in Fig. 4-15. The results show these errors to be negligible. The charts in Fig. 4-16 show the plots for the phase angle of $C(x)$ vs. transmission distance along the export cable. The corresponding error plots due to the constant frequency model being used for the computation are shown in Fig. 4-17. The errors could be considered negligible as well. In conclusion, of the ABCD constants of the export cable, only $C(x)$ parameters may be calculated using the constant frequency model. To ensure high degree of accuracy in the determination of the LF-HVac export cable ABCD parameters, the recommendation would be to use the accurate model developed in this section. Skin effect is an important phenomenon when export cables are operated in an ac system with frequency values below the conventional HVac 50/60 Hz.

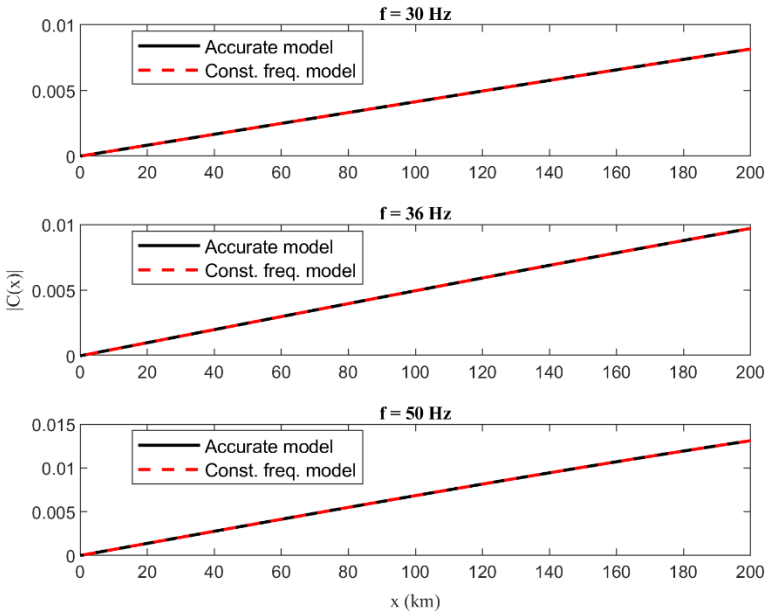

Fig. 4-14: $|C(x)|$ vs. transmission distance (i.e., x) plots along the 150 kV 800 mm^2 three-core XLPE cable length.

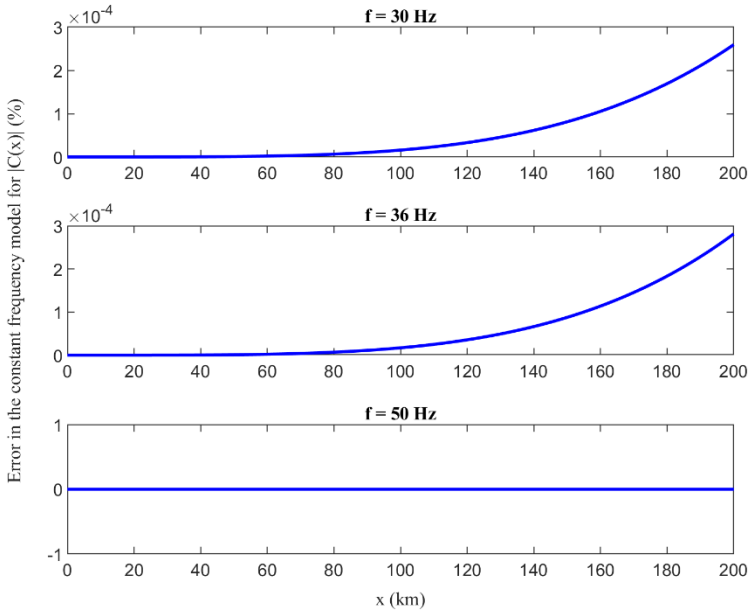

Fig. 4-15: Error in using the constant frequency model for calculating $|C(x)|$.

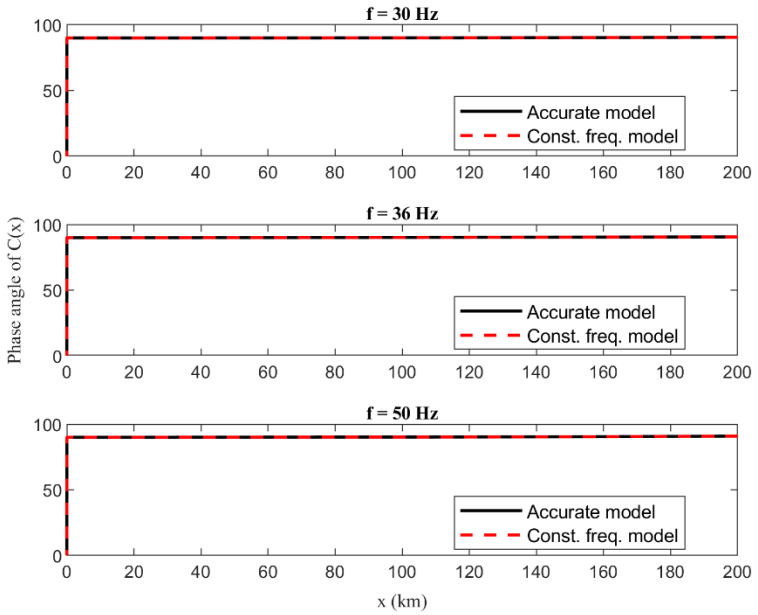

Fig. 4-16: Phase angle of $C(x)$ vs. transmission distance (i.e., x) plots along the 150 kV 800 mm^2 three-core XLPE cable length.

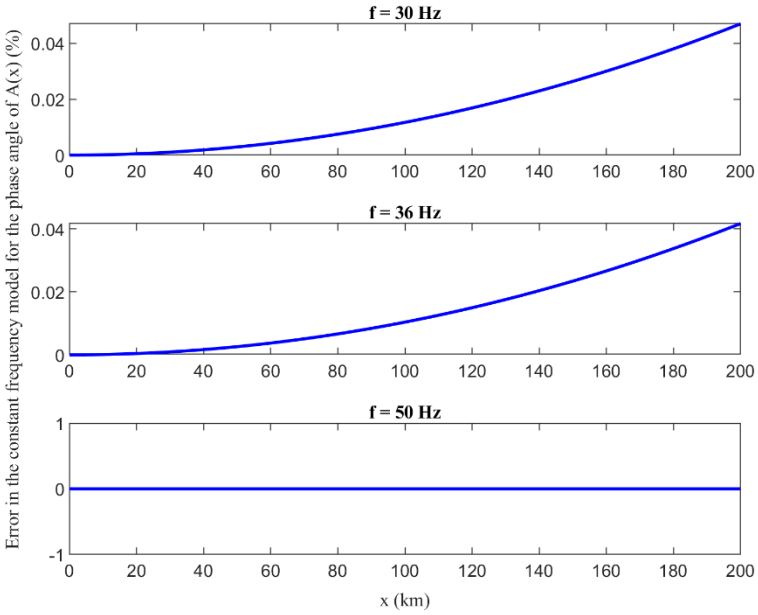

Fig. 4-17: Error in using the constant frequency model for calculating the phase angle of $C(x)$.

4.4. Frequency-Dependent Power Flow Model for the Export Cable

This section presents the derivation and analysis of generalized frequency-dependent equations used to determine the power flow at any point along the export cable length. The first sub-section focuses on the determination of the real power (P) and reactive power (Q) at the receiving terminal of the export cable. The second sub-section presents the derivation of the equations used to determine P and Q at the sending terminal, i.e., the offshore wind farm platform. The derived equations are then used to analyze the characteristics and performance of the export cable in the V/f controlled LF-HVac transmission system for offshore wind.

4.4.1. P and Q at the Receiving Terminal of the Export Cable

Equation (4-19) can be split into (4-20) and (4-21).

$$V(x) = A(x)V_R + B(x)I_R \tag{4-20}$$

$$I(x) = C(x)V_R + D(x)I_R \tag{4-21}$$

From (4-20), the current at the receiving terminal is determined, in terms of $V(x)$, $A(x)$, V_R, and $B(x)$, as (4-22) [5].

$$I_R = \frac{V(x) - A(x)V_R}{B(x)} \tag{4-22}$$

The terms in (4-22) are complex functions and can be expressed in terms of their magnitudes and phase angles as (4-23) - (4-26).

$$V(x) = |V(x)|\angle 0° \tag{4-23}$$

$$V_R = |V_R|\angle(-\delta) \tag{4-24}$$

$$A(x) = |A(x)|\angle a \tag{4-25}$$

$$B(x) = |B(x)|\angle b \tag{4-26}$$

Thus, I_R can be expressed as (4-27).

$$I_R = \frac{|V(x)|}{|B(x)|}\angle(-b) - \frac{|A(x)||V_R|}{|B(x)|}\angle(a-\delta-b) \tag{4-27}$$

Therefore, the complex power at the receiving terminal of the line is expressed as (4-28), where P_R is the real power, given by (4-29), and Q_R is the reactive power, given by (4-30) [5].

$$S_R = V_R I_R^* = P_R + jQ_R = \frac{|V(x)||V_R|}{|B(x)|}\angle(b-\delta) - \frac{|A(x)||V_R|^2}{|B(x)|}\angle(b-a) \tag{4-28}$$

$$P_R = \frac{|V(x)||V_R|}{|B(x)|}\cos(b-\delta) - \frac{|A(x)||V_R|^2}{|B(x)|}\cos(b-a) \tag{4-29}$$

$$Q_R = \frac{|V(x)||V_R|}{|B(x)|}\sin(b-\delta) - \frac{|A(x)||V_R|^2}{|B(x)|}\sin(b-a) \tag{4-30}$$

4.4.2. P and Q at the Sending Terminal of the Export Cable

In this sub-section the equations for the power flow at any point, other than at the receiving terminal, along the cable length are derived, provided that the voltage at that point is known or can be determined. Typically, this would be at sending end of the export cable. Equation (4-21) is repeated below as (4-31).

$$I(x) = C(x)V_R + D(x)I_R \tag{4-31}$$

It is desired to express $I(x)$ in terms of $V(x)$ and V_R, like the equations used in deriving the complex power at the receiving end. So, (4-22) is substituted for I_R in (4-31), thereby yielding (4-32).

$$I(x) = \frac{A(x)V(x)}{B(x)} + \left(C(x) - \frac{(A(x))^2}{B(x)}\right)V_R \tag{4-32}$$

To evaluate and simplify the second term on the right-hand side (RHS) of (4-32), it is more convenient to use the following hyperbolic substitutions: $A(x) = \cosh\gamma x$, $B(x) = Z_c \sinh\gamma x$, and $C(x) = \frac{1}{Z_c}\sinh\gamma x$. Thus, (4-32) becomes (4-33).

$$I(x) = \frac{A(x)V(x)}{B(x)} + \left(\frac{\sinh^2 \gamma x - \cosh^2 \gamma x}{Z_c \sinh \gamma x}\right) V_R \tag{4-33}$$

Using the hyperbolic function identity $\cosh^2 \gamma x - \sinh^2 \gamma x = 1$ in (4-33) results in (4-34).

$$I(x) = \frac{A(x)V(x)}{B(x)} - \frac{V_R}{B(x)} \tag{4-34}$$

Thus, $I(x)$ is now expressed in terms of $V(x)$ and V_R. Equation (4-34) can be written in magnitude and phase form as (4-35).

$$I(x) = -\frac{|V_R|}{|B(x)|}\angle(-\delta - b) + \frac{|A(x)||V(x)|}{|B(x)|}\angle(a - b) \tag{4-35}$$

Hence, the complex power at the sending end is given by (4-36), where $P(x)$ is the real power at that point, expressed as (4-37), and $Q(x)$ is the reactive power there, given by (4-38).

$$S(x) = V(x)I(x)^* = P(x) + jQ(x) = -\frac{|V(x)||V_R|}{|B(x)|}\angle(b + \delta) + \frac{|A(x)||V(x)|^2}{|B(x)|}\angle(b - a) \tag{4-36}$$

$$P(x) = -\frac{|V(x)||V_R|}{|B(x)|}\cos(b + \delta) + \frac{|A(x)||V(x)|^2}{|B(x)|}\cos(b - a) \tag{4-37}$$

$$Q(x) = -\frac{|V(x)||V_R|}{|B(x)|}\sin(b + \delta) + \frac{|A(x)||V(x)|^2}{|B(x)|}\sin(b - a) \tag{4-38}$$

4.5. Selection of V/f pairs for Maximum Power Delivery: Case Study

In sub-section 4.2.2, a basic example was used to illustrate how the proposed V/f controlled LF-HVac scheme could result in maximizing the amount of real power, corresponding to the wind energy output, that is delivered to the grid. The calculations for that example assumed that current and voltage values remained constant across the cable length. However, voltage and current profiles along a cable length do not produce a horizontal line when plotted on the cartesian plane, with the transmission distance on the abscissa (x-axis). Section 4.4 provides the equations for determining the voltage, current, and power flow at any point along the export

cable length. In power systems, voltage regulation is very important. To respect the applicable equipment insulation limit, its magnitude must never exceed a specified threshold. In addition, voltage regulation ensures that the core saturation design limits of transformers and reactors are not exceeded. So, it is crucial to define a set of performance criteria that would be used to judge the transmission performance of an export cable when deployed in the V/f controlled LF-HVac transmission scheme.

4.5.1. Case Study Offshore Wind Project Parameters

For the case study, the offshore wind project is specified to deliver 150 MW to the grid POI for wind conditions corresponding to the facility's rated output power. Thus, 150 MW is the nominal power rating, measured at the grid POI, of the offshore wind project. The term P_{rated} is used to identify this parameter. Note that for this study, the grid POI is defined as the export cable landing point, just before it is connected to the rectifying converter. The power rating of the wind farm would depend on the optimum V/f pair selected to deliver the P_{rated} = 150 MW at the grid POI. Note that the export cable is the 150 kV, 50 Hz rated 800 mm^2 three-core XLPE submarine cable of Chapter 3. Two offshore wind project configurations are considered: one with an export cable length of 150 km and the other being 200 km long.

4.5.2. The Export Cable Transmission Performance Criteria

It is important to specify some constraints, which would be used to judge the power transfer performance of the export cable. To minimize the requirements for reactive power support, [81] recommends limiting the power factor at the wind farm platform to $\geq$ 0.95. Utilities would typically require the generator owner (of the wind farm) to maintain unity power

factor at the grid POI. This would save them the trouble of provisioning for and managing any reactive power support at the POI.

The following outlines the criteria and assumptions that would be used to evaluate the transmission performance of the export cable system under the V/f controlled LF-HVac transmission of offshore wind energy.

1. The voltage magnitude at the receiving terminal (i.e., the grid POI) of the export cable, $|V_R|$, is assumed to be held constant at the applicable voltage value corresponding to the selected V/f pair for the LF-HVac transmission. Note that the applicable V/f pair is dependent on the wind energy output level. This is a realistic premise since the rectifying converter at the grid POI could be assigned the role of setting the LF-HVac grid voltage and frequency values.
2. Ideally, as often required by utility companies, the power factor at the grid POI should be unity. This is also recommended by [81].
3. The power factor at the sending terminal of the export cable should be greater than or equal to 0.95 [81].
4. The voltage magnitude at the sending end of the export cable, $|V_S|$, should be less than or equal to 1.05 of the applicable V/f ratio-determined $|V_R|$. Its lower limit should be $|V_S| = |V_R|$. This tight band is necessary to avoid saturation problems in transformers and reactors, especially when 50 Hz rated equipment are being repurposed for the V/f controlled LF-HVac transmission.
5. The aggregate wind farm power transformer, which is the LF-HVac transformer at the offshore platform, is assumed to be ideal, i.e., its losses are considered negligible.

Additionally, the onshore converters, at the grid POI, are also assumed to be ideal. These assumptions are to simplify the analysis.

4.5.3. Optimum V/f pair for P_{rated} Delivery to the Grid

The first step is to determine the range of V/f pairs that could support P_{rated} delivery to the grid via the export cable. To meet this criterion, the current value (measured at the defined grid POI) required to supply P_{rated} should not exceed the current rating of the export cable at the applicable frequency corresponding to the V/f pair. The following example would illustrate this.

Table 4-3: Cable current ratings, and current values required for P_{rated} delivery, for a set of V/f pairs.

V/f pair	72 kV/24 Hz	81 kV/27 Hz	90 kV/30 Hz	99 kV/33 Hz	108 kV/36 Hz
Current for P_{rated} (kA)	1.20	1.07	0.96	0.87	0.80
Cable current rating (kA)	0.98	0.95	0.93	0.90	0.88

Table 4-3 provides the current values required for P_{rated} delivery, and the applicable cable current rating, for a limited set of potential V/f pairs for the LF-HVac system case study. In the table, the shaded columns correspond to the V/f pairs that do not meet the criterion defined in the preceding paragraph. Thus, among the set of V/f pairs in Table 4-3, only V/f = 99 kV/33 Hz and V/f = 108 kV/36 Hz could support P_{rated} = 150 MW delivery to the grid. The logical next question would be, considering only integer values, how to determine the whole range of V/f pair candidates within the V/f pairs pool. Note that for the V/f controlled LF-HVac transmission case study, the pool consists of all V/f pairs < 150 kV/50 Hz, with the V/f derating factor being 3.

To determine the feasible V/f pairs range, the grid POI current corresponding to P_{rated} is limited to the applicable cable current rating if the value required to deliver P_{rated} exceeds the current rating. Hence, as shown in the graph of Fig. 4-18, the feasible V/f pairs range is determined to be 96 kV/32 Hz – 150 kV/50 Hz. Below 96 kV/32 Hz, the V/f pairs would not be able to support the delivery of P_{rated} without violating the stated criterion. The next step is to use the criteria and assumptions outlined in the preceding sub-section to narrow down the feasible V/f pairs range, and to eventually determine the optimum V/f pair.

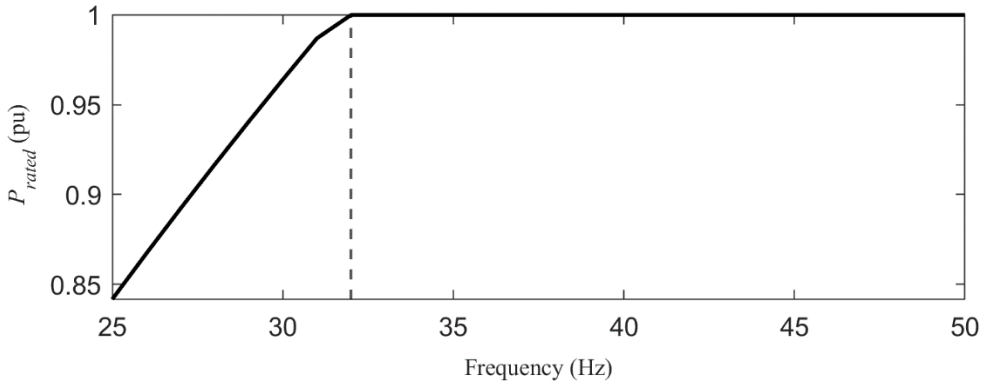

Fig. 4-18: Graph to determine the feasible V/f pairs range that could support the delivery of P_{rated} to the grid.

Wind Project Configuration I: Export cable length of 150 km

Fig. 4-19 presents the power factor vs. frequency, and the $|V_S|$ vs. frequency plots at the sending end of the export cable for this wind project configuration. In the power factor graph, only operation at the V/f pairs of 96 kV/32 Hz, 99 kV/33 Hz, and 102 kV/34 Hz would satisfy the power factor criterion (p.f. ≥ 0.95). Furthermore, of this set, only operation at V/f = 99 kV/33 Hz and V/f = 102 kV/34 Hz would satisfy the $1.00 \leq |V_S| \leq 1.05$ voltage requirement. Ultimately, V/f = 102 kV/34 Hz is selected as the optimum V/f pair. As will be shown in the following chapter, the V/f pair with the higher frequency value is favoured to minimize the LF-

HVac MMC submodules capacitor size. Thus, the wind project configuration I should have a rating of 160 MW/168 MVA (i.e., the offshore wind farm rating). These are determined using (4-36)-(4-38).

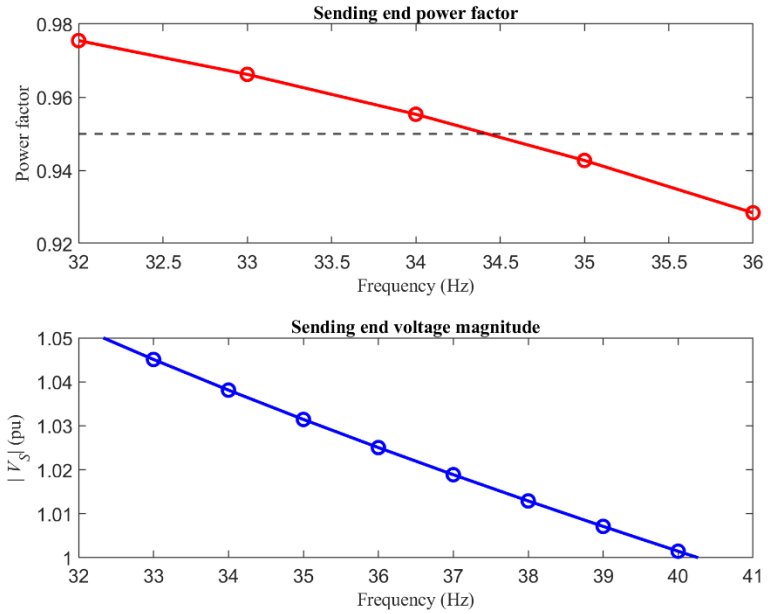

Fig. 4-19: Power factor vs. frequency, and $|V_S|$ vs. frequency plots at the sending end of the wind project configuration I, for P_{rated} delivery to the grid; export cable length = 150 km.

Fig. 4-20 presents the voltage and current profiles along the export cable length for the selected V/f pair: V/f = 102 kV/34 Hz. The current magnitude in the export cable would exceed the cable current rating along the 25 km stretch, measured from the wind farm, by up to 2%. However, this may not be a problem when the dynamic current rating of the cable is considered. Furthermore, the voltage profile plot shows the voltage magnitude along the cable did not exceed the recommended 1.05 pu threshold at any point.

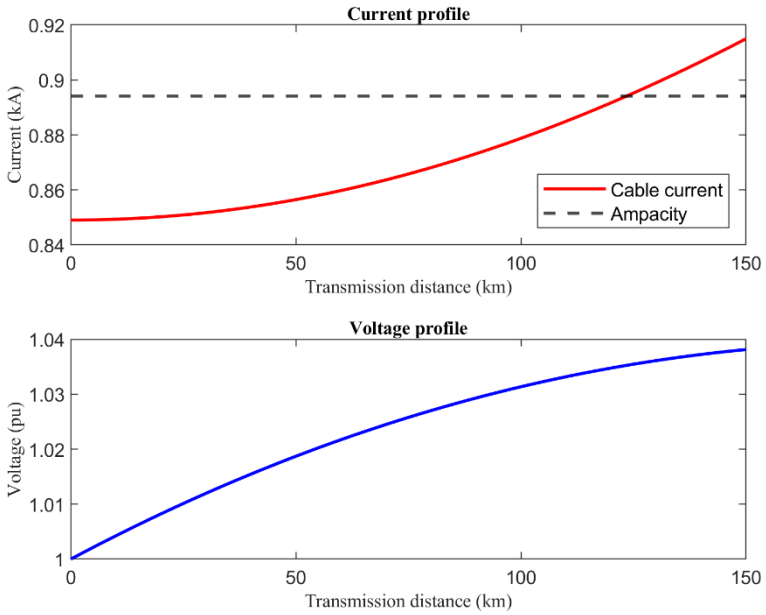

Fig. 4-20: Current and voltage profiles along the export cable length for wind project configuration I, during P_{rated} delivery to the grid. The graph origin represents the grid POI.

Wind Project Configuration II: Export cable length of 200 km

Fig. 4-21 presents the power factor vs. frequency, and the $|V_S|$ vs. frequency plots at the sending end of the export cable for this wind project configuration. In the power factor chart, only operation at V/f = of 96 kV/32 Hz would satisfy the power factor criterion (p.f. ≥ 0.95). However, this V/f pair would not meet the voltage magnitude criterion ($1.00 \leq |V_S| \leq 1.05$). On the other hand, operation at V/f = 99 kV/33 Hz would satisfy the voltage requirement, in addition to approximately meeting the power factor threshold. Thus, V/f = 99 kV/33 Hz is selected as the optimum V/f pair. Finally, the wind project configuration II would have a rating of 165 MW/174MVA (i.e., the offshore wind farm rating). These are determined using (4-36)-(4-38).

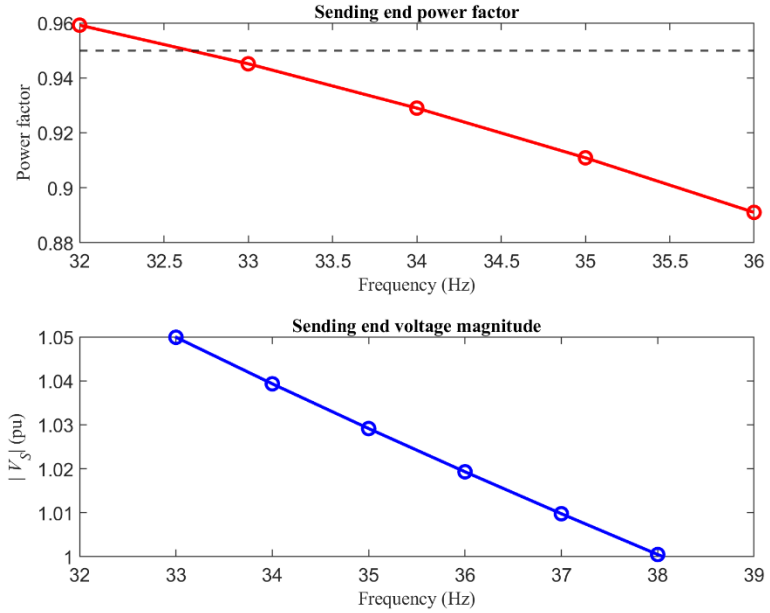

Fig. 4-21: Power factor vs. frequency, and $|V_S|$ vs. frequency plots at the sending end of the wind project configuration II, for P_{rated} delivery to the grid; export cable length = 200 km.

Fig. 4-22 presents the voltage and current profiles along the export cable length for the selected V/f pair: V/f = 99 kV/33 Hz. The current magnitude in the export cable would exceed the cable current rating through the first half, measured from the sending end, of the cable length, by up to 7%. Potentially, this could fall within the threshold of being considered acceptable when dynamic current rating is considered. As previously mentioned, dynamic current rating is beyond the scope of this thesis. Alternatively, some reactive compensation could be applied to improve the current profile along the cable length. Lastly, the voltage profile plot shows the voltage magnitude along the cable did not exceed the recommended 1.05 pu threshold at any point.

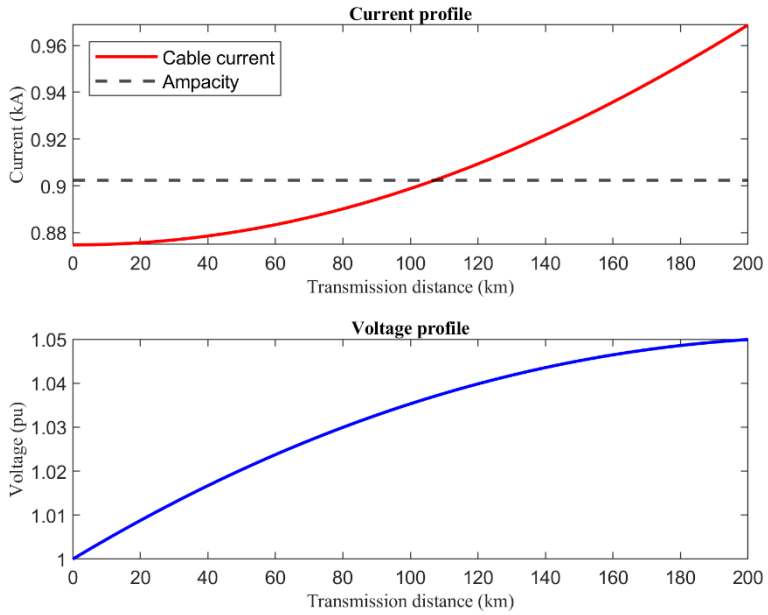

Fig. 4-22: Current and voltage profiles along the export cable length for wind project configuration II, during P_{rated} delivery to the grid. The graph origin represents the grid POI.

4.5.4. Optimum V/f pair for $0.8 \times P_{rated}$ Delivery to the Grid

Due to the intermittency of the wind farm power output, the V/f pair(s) for the optimal transmission performance of the export cable would be different at different output levels. Thus, for the delivery of $0.8 \times P_{rated}$, i.e., 120 MW, the first step is to determine the range of feasible V/f parameters for this energy output level. Similar to the method used in the preceding sub-section, the graph in Fig. 4-23 shows that below V/f = 72 kV/24 Hz, the V/f pairs would not be capable of supporting the delivery of $0.8 \times P_{rated}$ to the grid. This is based on the criterion specified in the preceding sub-section. As implemented in the preceding sub-section, the next step is to use the criteria and assumptions outlined for the evaluation of the export cable performance to narrow down the feasible V/f pairs range, and to eventually determine the optimum V/f pair.

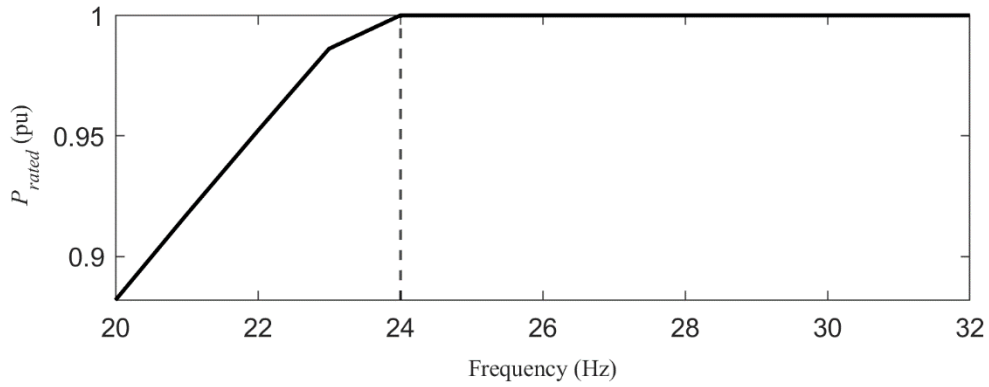

Fig. 4-23: Graph to determine the feasible V/f pairs range that could support the delivery of $0.8 \times P_{rated}$ to the grid.

Wind Project Configuration I: Export cable length of 150 km

Fig. 4-24 presents the power factor vs. frequency, and the $|V_S|$ vs. frequency plots at the sending end of the export cable for this wind project configuration. In the power factor graph, only operation within the range of V/f = 72 kV/24 Hz to V/f = 93 kV/31 Hz would satisfy the power factor criterion (p.f. ≥ 0.95). Furthermore, of this set, only operation at V/f = 90 kV/30 Hz and V/f = 93 kV/31 Hz would satisfy the $1.00 \leq |V_S| \leq 1.05$ voltage requirement. Ultimately, V/f = 93 kV/31 Hz is selected as the optimum V/f pair. As will be shown in the following chapter, the V/f pair with the higher frequency value is favoured to avoid any potential dc overvoltage problems with the rated LF-HVac MMC.

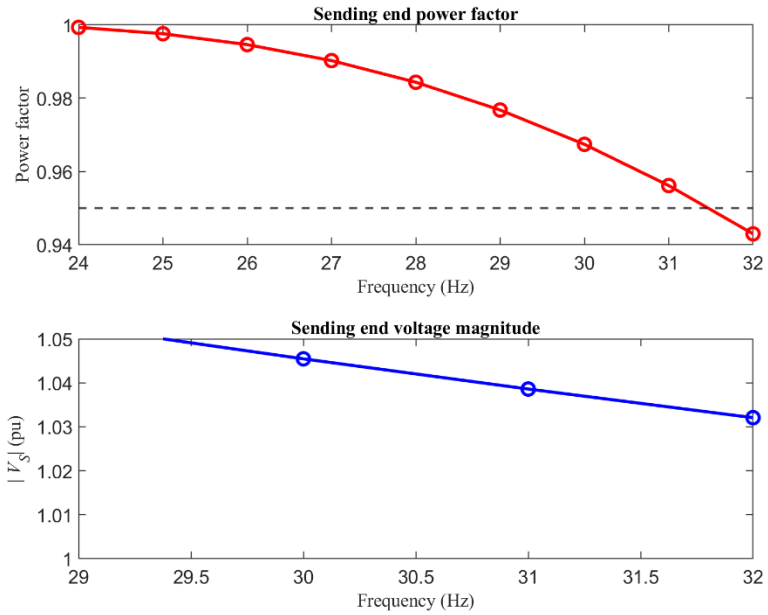

Fig. 4-24: Power factor vs. frequency, and $|V_S|$ vs. frequency plots at the sending end of the wind project configuration I, for $0.8 \times P_{rated}$ delivery to the grid; export cable length = 150 km.

Fig. 4-25 presents the voltage and current profiles along the export cable length for the selected V/f pair: V/f = 93 kV/31 Hz. At no point does the current magnitude exceed the export cable current rating. Also, the voltage profile plot shows the voltage magnitude along the cable does not exceed the recommended 1.05 pu threshold at any point.

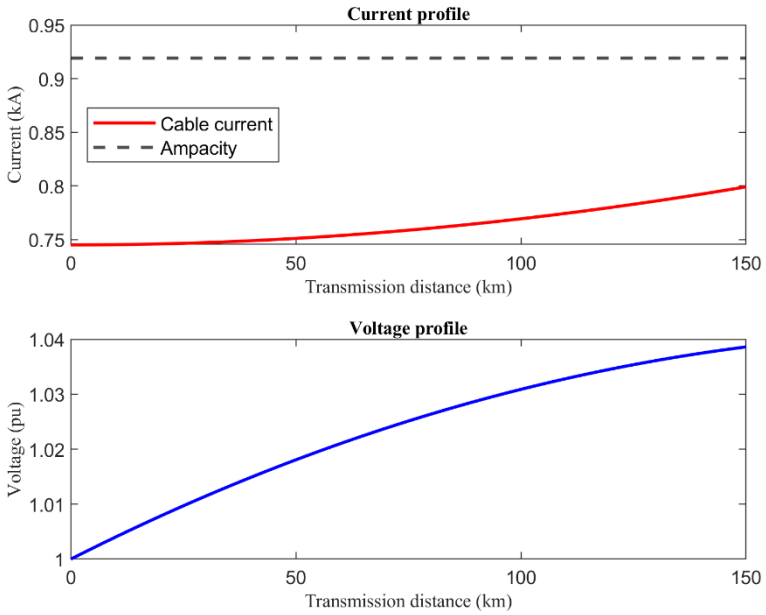

Fig. 4-25: Current and voltage profiles along the export cable length for wind project configuration I, during $0.8 \times P_{rated}$ delivery to the grid. The graph origin represents the grid POI.

Wind Project Configuration II: Export cable length of 200 km

Fig. 4-26 presents the power factor vs. frequency, and the $|V_S|$ vs. frequency plots at the sending end of the export cable for this wind project configuration. In the power factor graph, only operation within the range of V/f = 72 kV/24 Hz to V/f = 87 kV/29 Hz would satisfy the power factor criterion (p.f. ≥ 0.95). None of the V/f pairs within this set would satisfy the $1.00 \leq |V_S| \leq 1.05$ voltage requirement. However, note that, approximately, operation at V/f = 90 kV/30 Hz would meet both criteria. Hence, V/f = 90 kV/30 Hz is selected as the optimum V/f pair to deliver $0.8 \times P_{rated}$ to the grid.

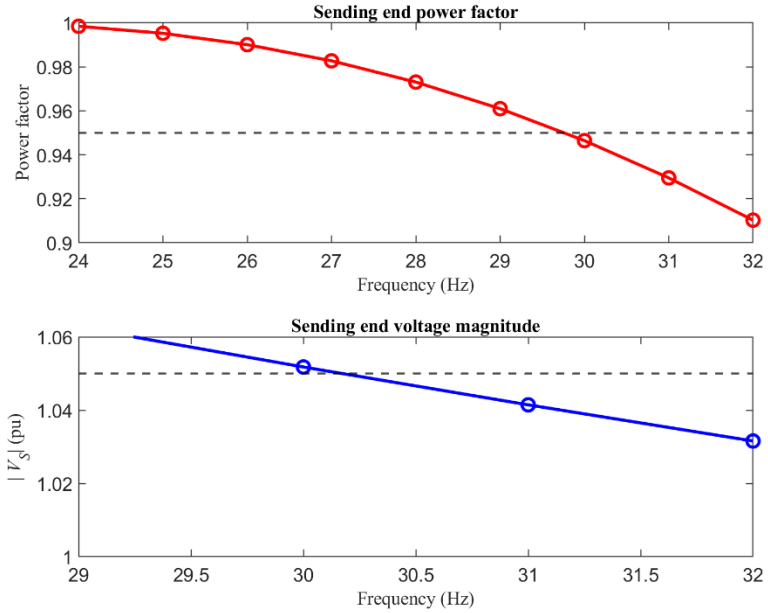

Fig. 4-26: Power factor vs. frequency, and $|V_S|$ vs. frequency plots at the sending end of the wind project configuration II, for $0.8 \times P_{rated}$ delivery to the grid; export cable length = 200 km.

Fig. 4-27 presents the voltage and current profiles along the export cable length for the selected V/f pair: V/f = 90 kV/30 Hz. At no point does the current magnitude exceed the export cable current rating. However, the voltage magnitude slightly exceeds the 1.05 pu threshold along a 20 km stretch, measured from the sending end, of the export cable. This could be accommodated within the design margins of the LF-HVac system.

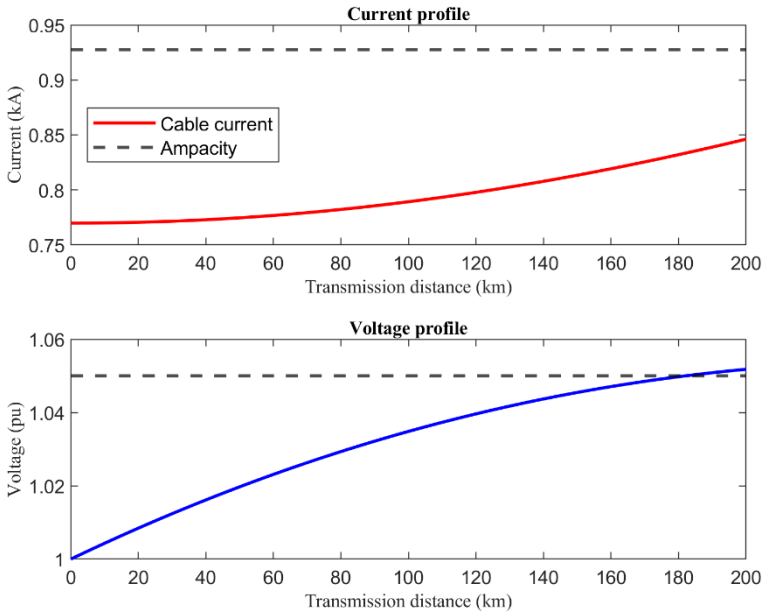

Fig. 4-27: Current and voltage profiles along the export cable length for wind project configuration II, during $0.8 \times P_{rated}$ delivery to the grid. The graph origin represents the grid POI.

4.5.5. Optimum V/f pair for $0.4 \times P_{rated}$ Delivery to the Grid

Following the method used in the preceding sub-section, the graph in Fig. 4-28 shows that below V/f = 33 kV/11 Hz, the V/f pairs would not be capable of supporting the delivery of $0.4 \times P_{rated}$ to the grid. The next step is to use the criteria and assumptions outlined for the evaluation of the export cable performance to narrow down the feasible V/f pairs range, and to eventually determine the optimum V/f pair.

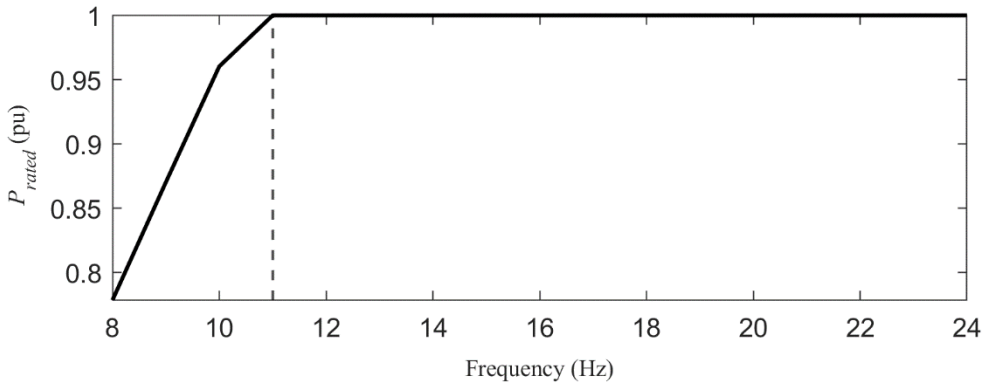

Fig. 4-28: Graph to determine the feasible V/f pairs range that could support the delivery of $0.4 \times P_{rated}$ to the grid.

Wind Project Configuration I: Export cable length of 150 km

Fig. 4-29 presents the power factor vs. frequency, and the $|V_S|$ vs. frequency plots at the sending end of the export cable for this wind project configuration. In the power factor graph, only operation within the range of V/f = 33 kV/11 Hz to V/f = 72 kV/24 Hz would satisfy the power factor criterion (p.f. ≥ 0.95). Furthermore, of this set, only operation at V/f = 66 kV/22 Hz, V/f = 69 kV/23 Hz, and V/f = 72 kV/24 Hz would satisfy the $1.00 \leq |V_S| \leq 1.05$ voltage requirement. Ultimately, V/f = 72 kV/24 Hz, the largest of the three, is selected as the optimum V/f pair.

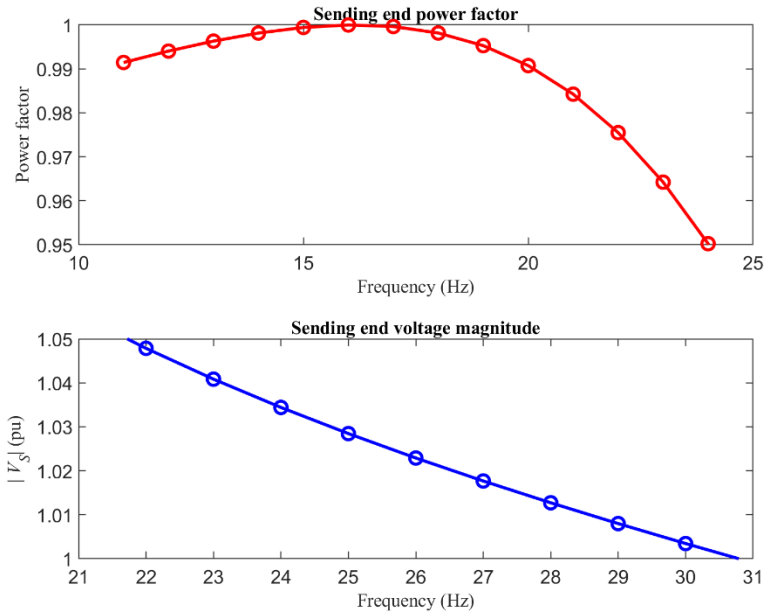

Fig. 4-29: Power factor vs. frequency, and $|V_S|$ vs. frequency plots at the sending end of the wind project configuration I, for $0.4 \times P_{rated}$ delivery to the grid; export cable length = 150 km.

Fig. 4-30 presents the voltage and current profiles along the export cable length for the selected V/f pair: V/f = 72 kV/24 Hz. At no point does the current magnitude exceed the export cable current rating. Also, the voltage profile plot shows the voltage magnitude along the cable does not exceed the recommended 1.05 pu threshold at any point.

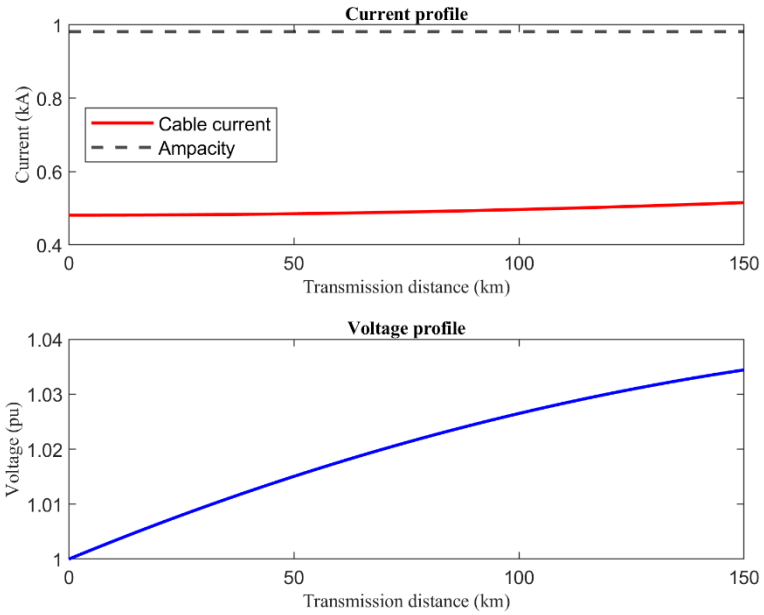

Fig. 4-30: Current and voltage profiles along the export cable length for wind project configuration I, during $0.4 \times P_{rated}$ delivery to the grid. The graph origin represents the grid POI.

Wind Project Configuration II: Export cable length of 200 km

Fig. 4-31 presents the power factor vs. frequency, and the $|V_S|$ vs. frequency plots at the sending end of the export cable for this wind project configuration. In the power factor graph, only operation within the range of V/f = 33 kV/11 Hz to V/f = 66 kV/22 Hz would satisfy the power factor criterion (p.f. ≥ 0.95). However, none of the V/f pairs within this set would satisfy the $1.00 \leq |V_S| \leq 1.05$ voltage requirement. Like the approximation method used in the preceding sub-section, V/f = 69 kV/23 Hz is selected as the optimum V/f pair to deliver $0.4 \times P_{rated}$ to the grid.

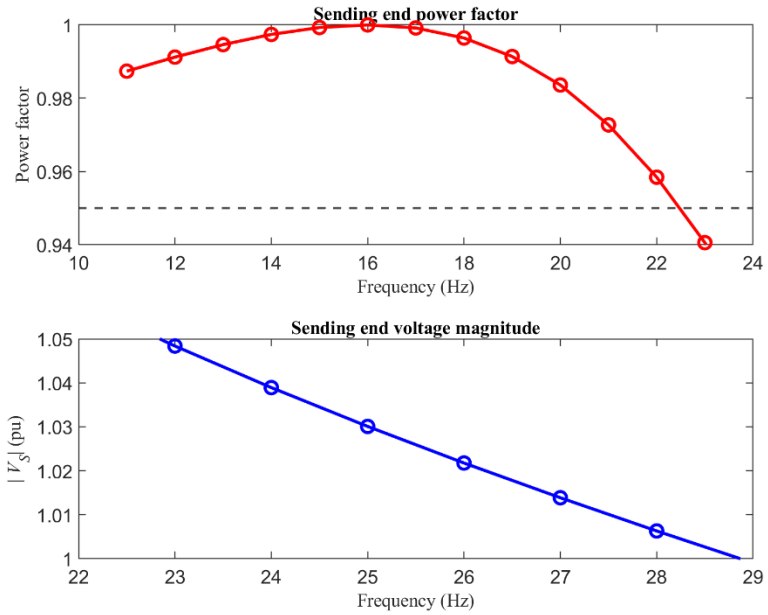

Fig. 4-31: Power factor vs. frequency, and $|V_S|$ vs. frequency plots at the sending end of the wind project configuration II, for $0.4 \times P_{rated}$ delivery to the grid; export cable length = 200 km.

Fig. 4-32 presents the voltage and current profiles along the export cable length for the selected V/f pair: V/f = 69 kV/23 Hz. At no point does the current magnitude exceed the export cable current rating. Also, the voltage profile plot shows the voltage magnitude along the cable does not exceed the recommended 1.05 pu threshold at any point.

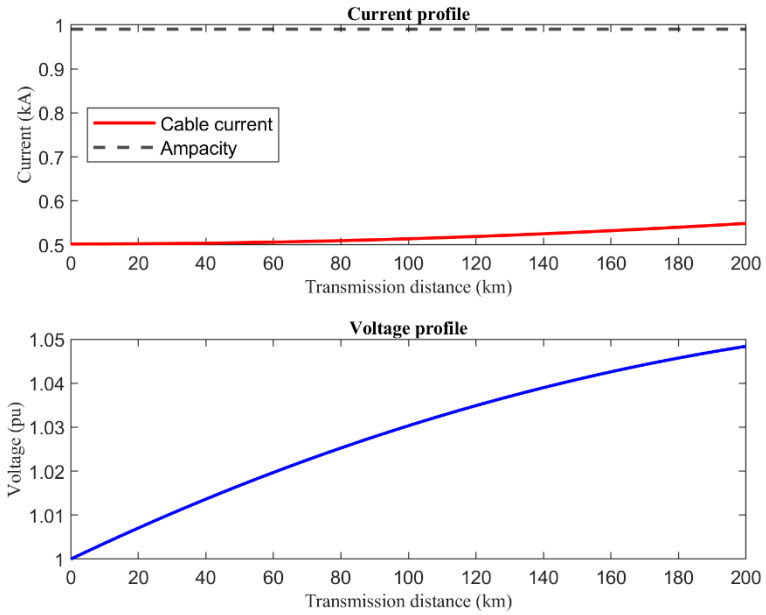

Fig. 4-32: Current and voltage profiles along the export cable length for wind project configuration I, during P_{rated} delivery to the grid. The graph origin represents the grid POI.

4.6. Summary

This chapter provided the technical premise in support of the feasibility and the fit, of this thesis-proposed V/f controlled LF-HVac transmission scheme for offshore wind. Wind is an intermittent and non-dispatchable energy resource. Therefore, it is important that for each available energy output quantity, the power transmission scheme can deliver most of the harnessed energy to the grid, while minimizing losses. As shown in Chapter 2 and Chapter 3, and further discussed in this chapter, charging current is the major limiting factor to the quantity of real power that can be delivered to the grid via a submarine cable. This becomes more pronounced as the cable length increases, even to the point that no useful power would reach the destination station.

As shown in this chapter, charging current is a function of the ac operating frequency f and the transmission voltage V. In determining the reactive power associated with the charging

current, it was shown that V impacts this quantity more than f, as the exponent of V is twice that of f. Thus, the most effective means to minimize losses associated with the charging current is to simultaneously reduce V and f for the ac system operation. As the case study results show, this strategy is especially useful during low wind energy output conditions since the combined reduction of V and f considerably minimizes charging current losses.

Finally, it is also shown that the V/f controlled LF-HVac method faces no technical obstacle when it comes to non-saturation operation of power transformers and reactors. On the contrary, the V/f controlled LF-HVac scheme allows for the repurposing of commercially available 50 Hz rated transformers, reactors, cables, and other power equipment. This is done by using the equipment applicable V/f derating factor in the selection of the optimum V and f for the applicable wind energy output.

Chapter 5

Modular Multilevel Converter: Capacity and Fit for the V/f Controlled LF-HVac Transmission Scheme

5.1. Introduction

The theme of this thesis has been the repurposing of existing power equipment, components, and technologies in the implementation of the V/f controlled LF-HVac transmission scheme for offshore wind. Thus far, it has been shown that commercially available 50 Hz rated export cables can be repurposed, even more advantageously, to implement the V/f controlled LF-HVac transmission scheme. It has also been shown that commercially available 50 Hz rated transformers and reactors can be used, by applying the equipment specific V/f derating, in the V/f controlled LF-HVac scheme. Note that commercially available wind turbines are increasingly of the type IV classification, whereby they are equipped with full power converters. Thus, with minor hardware modification and by applying the specified V/f derating, type IV turbines can be used in the V/f controlled LF-HVac transmission scheme.

In keeping with the theme, this chapter considers one of the most important components of the LF-HVac system: the converter, which converts the LF-HVac power to grid frequency power. MMC is the prevalent converter technology used in HVdc transmission. Its advantages were discussed in Chapter 2. The study presented in this chapter investigates the technical feasibility, the capacity, and the fit of MMC to be used in the V/f controlled LF-HVac

transmission scheme for offshore wind. Studies have recognized that the size of the MMC submodule capacitor is the key determinant in the overall size and weight of the converter [61], [82]. Reference [82] shows that the submodules capacitors' energy storage requirements are inversely proportional to the system frequency. Therefore, for the V/f controlled LF-HVac system, where the frequency is varied, it is vital to adequately size the submodules capacitor to accommodate the applicable LF-HVac frequency range.

5.2. MMC: Principles of Operation

Fig. 5-1 is the schematic representation of a back-to-back (BtB) MMC [63], [82]. The back-to-back arrangement permits the ac frequencies on the two ac buses to be different. Hence, it could serve as the frequency conversion interface between the LF-HVac system and the HVac grid. The Rectifier MMC converts the LF-HVac power to dc intermediate power. The Inverter

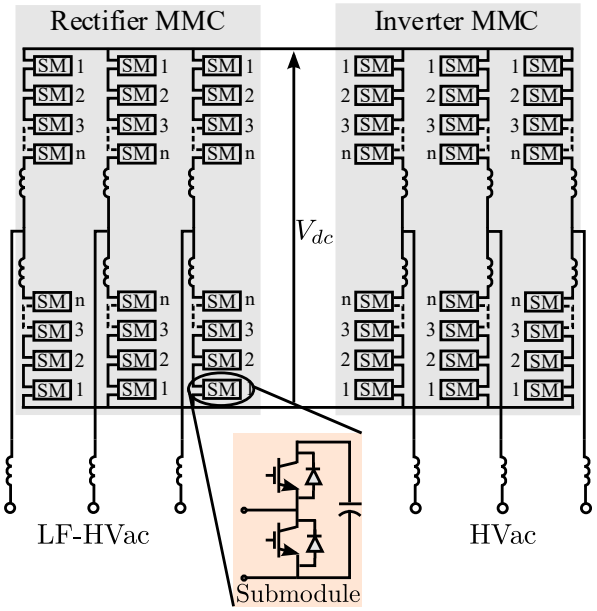

Fig. 5-1: Schematic diagram of a back-to-back MMC.

MMC then converts the dc intermediate power to grid HVac power. Each unit MMC consists of three phase legs. Fig. 5-2 shows the schematic diagram of an MMC phase leg. Each phase leg consists of an upper arm and a lower arm. In each arm is a series connected half-bridge submodules. The half-bridge submodule, which is the simplest submodule configuration, is not capable of dc fault blocking or bipolar operation [63]. However, those features may not be required in the LF-HVac BtB-MMC. On the other hand, the half-bridge submodules MMC has the minimum number of power semiconductor devices. In addition to its relative control simplicity, this MMC could prove advantageous in LF-HVac applications.

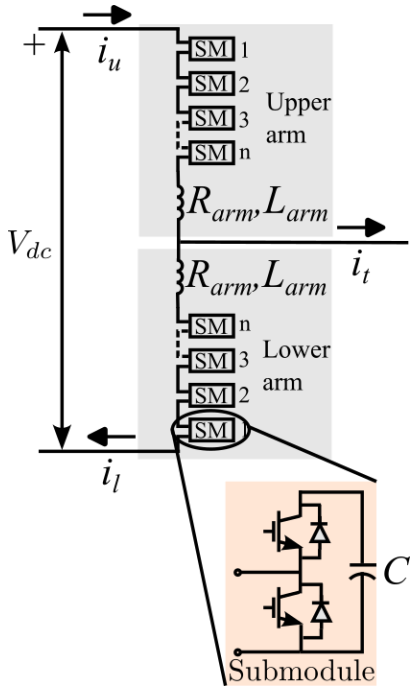

Fig. 5-2: Schematic diagram of a phase leg of an MMC, showing the upper and the lower arms.

With n submodules in each arm, the nominal voltage across the submodule capacitor, V_{SM}, is given by (5-1), where V_{dc} is the MMC dc-link voltage.

$$V_{SM} = \frac{V_{dc}}{n} \tag{5-1}$$

Each arm contains an arm reactor, represented as R_{arm}, L_{arm} in Fig. 5-2. L_{arm} is the inductance of the reactor while R_{arm} is the resistance associated with the reactor. The main function of the arm reactor is to limit the magnitude of the circulating current flowing in the arms [63]. The presence of the circulating current stems from switching mismatch between the upper and the lower arm submodules, in addition to voltage ripples in the submodule capacitors [63].

5.2.1. MMC: Voltage and Current in the Upper and the Lower Arms

Referring to Fig. 5-2, i_u is the current that flows in the upper arm while i_l is the current in the lower arm. Applying KCL to the node between the upper and the lower arms yields (5-2), where i_t is the current that flows to the ac terminal of the converter.

$$i_t = i_u - i_l \tag{5-2}$$

The peak phase ac voltage at the converter terminal is given by (5-3), where m is the modulation index of the converter.

$$\hat{V}_t = m\frac{V_{dc}}{2} \tag{5-3}$$

The current in each arm consists of a dc component, i_{dc}, an ac circulating current component, i_{c-ac}, and the ac terminal current i_t. Equations (5-4) and (5-5), respectively, are the expressions for the upper and the lower arm currents [63].

$$i_u = \frac{1}{3}i_{dc} + i_{c-ac} + \frac{1}{2}i_t \tag{5-4}$$

$$i_l = \frac{1}{3}i_{dc} + i_{c-ac} - \frac{1}{2}i_t \tag{5-5}$$

The sum of (5-4) and (5-5) yields (5-6), which is the equation for the circulating current in the arms.

$$i_c = \frac{1}{2}(i_u + i_l) = \frac{1}{3}i_{dc} + i_{c-ac} \tag{5-6}$$

Thus, (5-4) and (5-5) can be rewritten as (5-7) and (5-8), respectively.

$$i_u = i_c + \frac{1}{2} i_t \tag{5-7}$$

$$i_l = i_c - \frac{1}{2} I_t \tag{5-8}$$

The sinusoidal ac voltage and current at the converter terminal are expressed as (5-9) and (5-10), respectively, where ω is the fundamental angular frequency and ϕ is the phase difference between the voltage and the current [82].

$$v_t = \hat{V}_t \cos(\omega t) \tag{5-9}$$

$$i_t = \hat{I}_t \cos(\omega t \pm \phi) \tag{5-10}$$

5.2.2. MMC: Output Voltage Waveform Synthesis

The simplest output voltage synthesis method used in MMC is the nearest level control (NLC). The strategy is to apply stepwise switching control to the individual submodule switches to generate a multilevel near-sinusoidal waveform, closely resembling the sinusoidal voltage reference [64]. However, a commonly used MMC modulation strategy is the phase-shifted carrier (PSC) multilevel sinusoidal pulse width modulation (PWM) [64]. It can effectively minimize harmonics in the generated output voltage. Thus, PSC-PWM is the MMC modulation strategy that will be considered for the V/f controlled LF-HVac MMC. References [61] and [63] provide in-depth coverage of the strategies used in MMC PWM and control.

5.2.3. Energy Storage and Peak Voltage in the MMC Submodule Capacitor

This section provides the analysis of the required energy storage capacity of the V/f controlled LF-HVac MMC submodules capacitor. First, the following assumptions are adopted to simplify the analysis [82].

a. An ideal circulating current control is assumed. This means that only the dc component (of the circulating current) is present since the ac circulating current component would be completely suppressed.
b. Perfect capacitor voltage balance is achieved within each MMC arm. Note that realistically, some variations in the submodules' capacitor voltages would exist. This is due to the limited switching frequency of the converter PWM [82]. Hence, the selected submodule capacitor voltage limit must accommodate the deviations above the defined nominal capacitor voltage.

Equation (5-1) gives the nominal, i.e., the reference, voltage across each submodule capacitor: V_{SM}. However, as the capacitors are charged and discharged the voltage across each submodule capacitor would vary with time [82]. Thus, there exists a direct voltage, V_{SM}^{*}, whose expression is given in (5-11), associated with the time-average of the stored energy in the submodule capacitors [82].

$$V_{SM}^{*} = k_{dc} V_{SM} \tag{5-11}$$

The factor k_{dc} in (5-11) is unity at the defined nominal submodule voltage V_{SM}. Through the converter control, the value of k_{dc} could be greater than or less than unity, as the time-average of the stored energy in the submodule capacitors is varied [82]. Thus, the energy storage per MMC arm, E_{arm}, is given by (5-12), where C_{SM} is the submodule capacitance.

$$E_{arm} = \frac{k_{dc}^2 C_{SM} V_{dc}^2}{2n} \tag{5-12}$$

The submodules have a maximum voltage rating, which the peak instantaneous capacitor voltage must never exceed. To represent this voltage limit V_{SM-max}, k_{dc} in (5-11) is substituted with k_{max}:

$$V_{SM-max} = k_{max} V_{SM} \tag{5-13}$$

As observed in (5-12), k_{max} determines the maximum energy storage capacity for each MMC arm, as expressed in (5-14) [82].

$$E_{arm-max} = \frac{k_{max}^2 C_{SM} V_{dc}^2}{2n} \tag{5-14}$$

The difference between $E_{arm-max}$ and E_{arm}, expressed as (5-15), is the utmost excess energy stored in each arm [82].

$$\Delta E_{max} = E_{arm-max} - E_{arm} = \frac{C_{SM} V_{dc}^2}{2n}\left(k_{max}^2 - k_{dc}^2\right) \tag{5-15}$$

Examination of (5-15) suggests that for a given set of values for k_{max}, k_{dc}, V_{dc}, and ΔE_{max}, there is a corresponding minimum submodule capacitance, C_{SM-min}. This is expressed as (5-16).

$$C_{SM-min} = \frac{2n\Delta E_{max}}{V_{dc}^2(k_{max}^2 - k_{dc}^2)} \tag{5-16}$$

Thus, for $C_{SM} \geq C_{SM-min}$, the MMC submodule instantaneous voltage would not exceed the rated voltage. The term $\frac{C_{SM}V_{dc}^2}{2n}$ in the RHS of (5-15) represents the energy storage per MMC arm. Hence, for a given value of this term, the inequality in (5-17) is satisfied, where E_{nom} is the nominal energy storage per MMC arm [82].

$$E_{nom} \geq \frac{\Delta E_{max}}{k_{max}^2 - k_{dc}^2} \tag{5-17}$$

Similarly, substitution of (5-16) into (5-14) and evaluation yields the inequality in (5-18).

$$E_{max} \geq \frac{k_{max}^2}{k_{max}^2 - k_{dc}^2}\Delta E_{max} \tag{5-18}$$

Assessment of (5-18) suggests that the required energy storage capacity of the MMC depends on the ΔE_{max}, k_{max}, and k_{dc} design values.

5.2.4. MMC: Stored Energy Variations, Sinusoidal Voltage Reference PWM

In MMC PWM with sinusoidal voltage reference, (5-19) and (5-20)

$$v_u = \frac{V_{dc}}{2}(1 - m\cos\omega t) \tag{5-19}$$

$$v_l = \frac{V_{dc}}{2}(1 + m\cos\omega t) \tag{5-20}$$

are the expressions for the voltages in the upper and the lower arms of the MMC, respectively [82]. Assuming zero harmonics in the circulating current, the corresponding arm currents are given by (5-21) and (5-22) [82].

$$i_u = \frac{\widehat{I_s}}{4}(m\cos\phi + 2\cos(\omega t - \phi)) \tag{5-21}$$

$$i_l = \frac{\widehat{I_s}}{4}(m\cos\phi - 2\cos(\omega t - \phi)) \tag{5-22}$$

The product of the corresponding currents and voltages gives the instantaneous power in each arm [61], [82].

$$p_u = \frac{V_{dc}\widehat{I_s}}{8}[2\cos(\omega t - \phi) - m\cos(2\omega t - \phi) - m^2\cos\omega t \cdot \cos\phi] \tag{5-23}$$

$$p_l = -\frac{V_{dc}\widehat{I_s}}{8}[2\cos(\omega t - \phi) + m\cos(2\omega t - \phi) - m^2\cos\omega t \cdot \cos\phi] \tag{5-24}$$

Equation (5-23) is the expression for the instantaneous power in the upper arm while (5-24) denotes the instantaneous power in the lower arm. Integration of (5-23) and (5-24) yields the energy variations in the corresponding arms: (5-25) and (5-26), where the total apparent power transfer S is given as (5-27).

$$e_u = \frac{S}{12m\omega}[4\sin(\omega t - \phi) - m\sin(2\omega t - \phi) - 2m^2\sin\omega t \cdot \cos\phi] \tag{5-25}$$

$$e_l = -\frac{S}{12m\omega}[4\sin(\omega t - \phi) + m\sin(2\omega t - \phi) - 2m^2\sin\omega t \cdot \cos\phi] \tag{5-26}$$

$$S = \frac{3}{2}\widehat{V_t}\widehat{I_t} \tag{5-27}$$

Due to symmetry, the peak values of e_u and e_l are the same. This peak value is the excess energy storage capacity for each MMC arm: ΔE_{max}, given by (5-28).

$$\Delta E_{max} = \max(e_u) = \max(e_l) \tag{5-28}$$

Note that e_u or e_l, i.e., (5-25) or (5-26), respectively, is inversely proportional to the ac system operating frequency. Hence, for the V/f controlled LF-HVac scheme, ΔE_{max}, and thus the required MMC energy storage capacity would be considerably higher than for an equivalent conventional HVdc MMC.

5.2.5. MMC: Stored Energy Variations, Voltage Reference with Third-Order Harmonic Injection PWM

Third-order harmonic injection is used to extend the operating range of VSC converters [60]. Thus, the voltages in the upper and lower arms of the MMC are given by (5-29) and (5-30), respectively [82].

$$v_u^{th} = \frac{V_{dc}}{2}\left(1 - m\cos\omega t + \frac{1}{6}m\cos(3\omega t)\right) \tag{5-29}$$

$$v_l^{th} = \frac{V_{dc}}{2}\left(1 + m\cos\omega t - \frac{1}{6}m\cos(3\omega t)\right) \tag{5-30}$$

The corresponding instantaneous powers are given by (5-31) and (5-32), with p_u and p_l already defined in (5-23) and (5-24), respectively.

$$p_u^{th} = p_u + \frac{V_{dc}\widehat{I_t}}{48}m^2\cos(3\omega t)\cdot\cos\phi + \frac{V_{dc}\widehat{I_t}}{24}m\cos(3\omega t)\cdot\cos(\omega t - \phi) \tag{5-31}$$

$$p_l^{th} = p_l - \frac{V_{dc}\widehat{I_t}}{48}m^2\cos(3\omega t)\cdot\cos\phi + \frac{V_{dc}\widehat{I_t}}{24}m\cos(3\omega t)\cdot\cos(\omega t - \phi) \tag{5-32}$$

Integration of (5-31) and (5-32) yields the corresponding energy variations: (5-33) and (5-34), where e_u and e_l are defined in (5-25) and (5-26), respectively.

$$e_u^{th} = e_u + \frac{S}{12\omega}\left[\frac{m}{9}\sin(3\omega t)\cdot\cos\phi + \frac{1}{12}\sin(4\omega t - \phi) + \frac{1}{6}\sin(2\omega t + \phi)\right] \tag{5-33}$$

$$e_l^{th} = e_l - \frac{S}{12\omega}\left[\frac{m}{9}\sin(3\omega t)\cdot\cos\phi - \frac{1}{12}\sin(4\omega t - \phi) - \frac{1}{6}\sin(2\omega t + \phi)\right] \tag{5-34}$$

Finally, the excess energy in each MMC arm, when the PWM voltage reference has third-order harmonic injection, is given by (5-35).

$$\Delta E_{max}^{th} = \max(e_u^{th}) = \max(e_l^{th}) \tag{5-35}$$

5.2.6. MMC: Selection of k_{dc}

The factor k_{dc} in (5-17) and (5-18) can be adjusted by controlling the time-average of the stored energy in the MMC submodule capacitors [82]. However, at each operating point, the requested instantaneous voltage in the upper or the lower arm of the MMC must be fulfilled by the sum of the submodules' capacitor voltages in the corresponding arm. Thus, it is important that the selected value of k_{dc} must be that the requested arm voltage is always available in the submodule capacitors, as a summation [82]. In each MMC arm, the instantaneous stored energy is the sum of the time-average energy E_{arm} and the energy variations, e_u or e_l (e_u^{th} or e_l^{th} for the case of PWM with third-order harmonic injection voltage reference). Therefore, to ensure the requested instantaneous arm voltage never exceeds the sum total of the corresponding arm's submodules' capacitor voltages, (5-36) and (5-37) must be satisfied.

$$E_{arm} + e_u \geq \frac{1}{2}\frac{C_{SM}}{n}v_u^2 \tag{5-36}$$

$$E_{arm} + e_l \geq \frac{1}{2}\frac{C_{SM}}{n}v_l^2 \tag{5-37}$$

Substitution of (5-12) and (5-16) into (5-36) and evaluation yields (5-38). Note that due to symmetry, the above stated substitution and evaluation can alternatively be applied to (5-37) in the determination of k_{dc}.

$$\frac{k_{dc}^2 \Delta E_{max}}{k_{max}^2 - k_{dc}^2} + e_u \geq \frac{\Delta E_{max} v_u^2}{V_{dc}^2 (k_{max}^2 - k_{dc}^2)} \tag{5-38}$$

Solving (5-38) for k_{dc} yields (5-39).

$$k_{dc} \geq \sqrt{\frac{\Delta E_{max} v_u^2 - k_{max}^2 V_{dc}^2 e_u}{V_{dc}^2 (\Delta E_{max} - e_u)}}, e_u \neq \Delta E_{max} \tag{5-39}$$

The selection of k_{dc} depends on the MMC design objective(s). Note that selecting the minimum value of k_{dc}, which satisfies (5-39), would allow for the highest peak voltage ripple in the submodules' capacitors [82]. According to (5-25) and (5-26) (or (5-33) and (5-34)), the voltage ripples in the LF-HVac MMC would be much higher than the voltage ripples in an equivalent HVdc MMC. Therefore, the minimum possible k_{dc} should be selected when designing the V/f controlled LF-HVac MMC.

5.2.7. MMC: Rated and Nominal Energy Storage Requirement

The MMC nominal energy storage and the maximum energy storage capacity, per arm, can be determined using (5-17) and (5-18), respectively. Note that the nominal energy storage would depend on the required operating point, and the specified peak voltage ripple [82]. Observation of (5-17), (5-18), and (5-25) and (5-26) (or (5-33) and (5-34)) show that E_{nom} and E_{max} are proportional to the apparent power transfer S. Note that ΔE_{max} in (5-17) and (5-18) is equal to $\max(e_u)$ (or $\Delta E_{max}^{th} = \max(e_u^{th})$, for the case of voltage reference with third-order harmonic injection). Thus, with six arms per converter, the overall MMC energy storage requirement per transferred apparent power is given by (5-40) and (5-41), where W_{MMC} is the required MMC nominal energy storage, while $W_{MMC-rated}$ is the rated (i.e., the maximum) energy storage capacity of the MMC [82].

$$W_{MMC} = \frac{6E_{nom}}{S} \tag{5-40}$$

$$W_{MMC-rated} = \frac{6E_{max}}{S} \tag{5-41}$$

In (5-41), E_{max}, which is given by (5-18), has its primary determinants as k_{max}, m (modulation index), ω (ac frequency), and ϕ (phase angle between voltage and current). From (5-25) (or (5-33)), the energy variations are shown to be inversely proportional to frequency. Therefore, compared to the conventional HVdc MMC, the V/f controlled LF-HVac MMC would have a much higher energy storage requirement and/or capacity. Consequently, minimizing the MMC submodule capacitor size, and in turn the overall converter size, becomes a non-trivial problem, given the associated costs.

5.2.8. MMC Rated Energy Storage: PWM with Sinusoidal Voltage Reference vs. PWM with Third-Order Harmonic Injected Voltage Reference

Fig. 5-3 presents the plots of the required rated energy storage capacity of the MMC vs. the ac system frequency, where the frequency range is the feasible f range that could support the delivery of P_{rated} to the grid in the Chapter 4 case study. Two sets of plots are presented: the first one corresponds to PWM with sinusoidal voltage reference being used for the MMC output voltage synthesis, while the second one corresponds to PWM with third-order harmonic injected voltage reference being used for the MMC output voltage synthesis. The four individual line

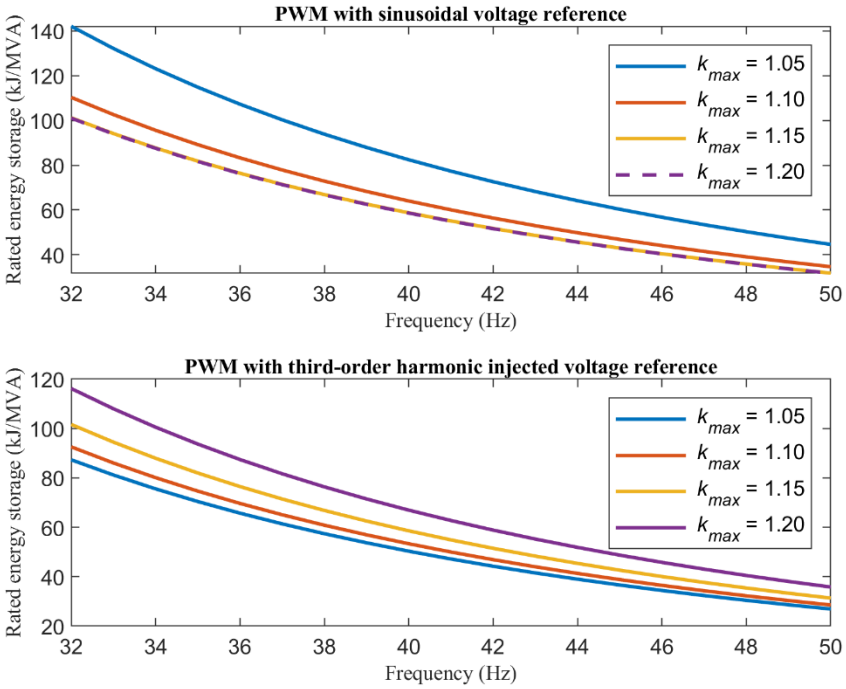

Fig. 5-3: Plots of the required rated energy storage capacity of the MMC vs. the ac system frequency (for the feasible f range to deliver P_{rated} in the Chapter 4 case study).

plots in each of the above sets correspond to k_{max} = 1.05, 1.10, 1.15, and 1.20. Note that k_{max} is the factor used to specify the MMC submodule rated voltage.

Inspection of Fig. 5-3 shows that, as expected, the lower the ac frequency, the higher the required rated energy storage capacity of the MMC. There is an interesting observation from the plots, with respect to the PWM voltage reference being used and the corresponding value of k_{max}. For the PWM with sinusoidal voltage reference modulation method, the rated energy storage capacity is the largest when k_{max} = 1.05. This means that larger submodule capacitors must be used to build the MMC. On the other hand, for the PWM with third-order harmonic injected voltage reference modulation method, the rated energy storage capacity is the largest when k_{max} = 1.20, and the lowest when k_{max} = 1.05. Therefore, this is the preferred modulation

method to be used. It would allow the MMC to have the minimum submodule voltage rating, in addition to minimizing the submodules capacitor size.

5.3. Case Study: V/f Controlled LF-HVac MMC Energy Storage Requirement

This is the continuation of the case study treated in Chapter 4. In that chapter, the selection of the energy output level applicable V/f parameters set is based on the defined export cable performance criteria. In line with the topic discussed in this chapter, this case study will determine the parameters of the rated MMC, in addition to verifying that its energy storage capacity is sufficient for the V/f controlled LF-HVac system operation at the Chapter 4 selected V/f pairs. Note that for brevity, only the wind project configuration I, whose export cable is 150 km long, is treated in this case study. Parameters for the V/f controlled LF-HVac MMC are listed in Table 5-1. The equations developed in this chapter were used to compute the values of the parameters.

Table 5-1: Parameters for V/f controlled LF-HVac MMC, for the case study wind project configuration I.

Parameter	Symbol	Value	Unit
Dc-link voltage	V_{dc}	250	kV
Submodule rated voltage limit factor	k_{max}	1.1	-
Submodule capacitance: PWM with sinusoidal voltage reference, for			
V/f = 102 kV/34 Hz	V/f = 150 kV/50 Hz		
3900 μF	1400 μF		
Time-averaged voltage factor: PWM with sinusoidal voltage reference			
$k_{dc} = 1.0089$			
Submodule capacitance: PWM with third-order harmonic injected voltage reference, for			
V/f = 102 kV/34 Hz	V/f = 150 kV/50 Hz		
3600 μF	1300 μF		
Time-averaged voltage factor: PWM with third-order harmonic injected voltage reference			
$k_{dc} = 1.0154$			

5.3.1. P_{rated} (150 MW) Delivery to the Grid: MMC Rated Parameters Design

For illustration purposes, the V/f controlled LF-HVac MMC is designed for the two MMC modulation methods discussed in the preceding section: PWM with sinusoidal voltage reference, and PWM with third-order harmonic injected voltage reference. For more comparisons, the MMC is designed for rated V/f = 102 kV/34 Hz (i.e., the rated V/f set selected in Chapter 4), and for rated V/f = 150 kV/50 Hz (which applies to an equivalent HVdc MMC).

MMC Modulation Method I: PWM with Sinusoidal Voltage Reference

From Table 5-1, and for the PWM with sinusoidal voltage reference method, the minimum submodule capacitance is 1400 μF when the rated V/f =150 kV/50 Hz. On the other hand, the minimum submodule capacitance is 3900 μF when the rated V/f =102 kV/34 Hz, which is nearly three times the capacitance of the equivalent HVdc MMC. This observation supports the MMC energy storage requirement(s) presented in the preceding section.

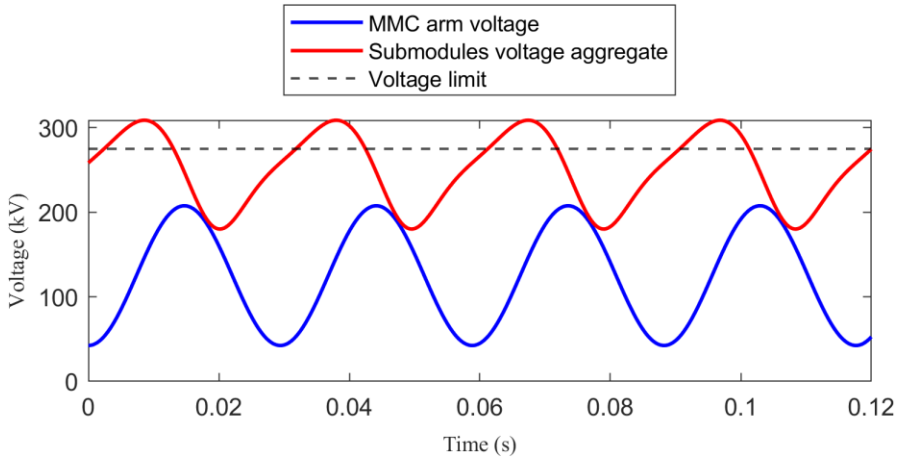

(a)

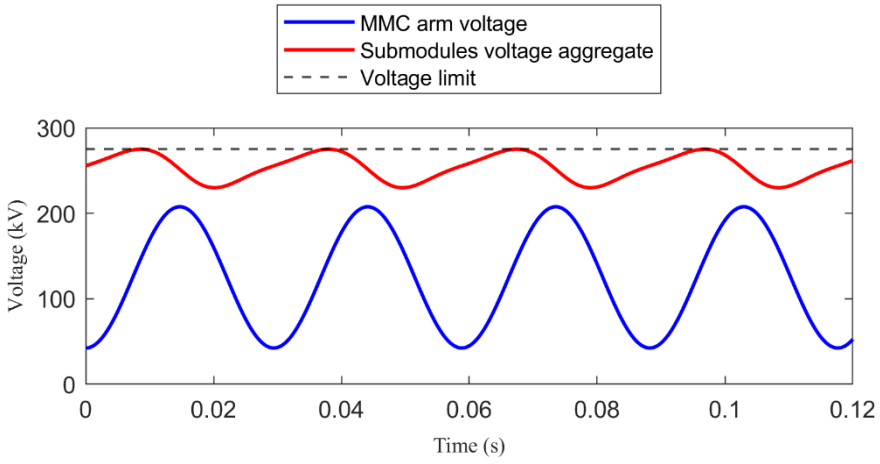

(b)

Fig. 5-4: Plots of the MMC upper arm voltage and the submodules voltage aggregate for the rated wind project configuration I; (a): submodules capacitance = 1400 μF, (b): submodules capacitance = 3900 μF.

The voltage plots in Fig. 5-4 show that using the equivalent HVdc MMC designed submodule capacitance instead of the capacitance specifically designed for the V/f controlled LF-HVac MMC would result in dc overvoltage.

MMC Modulation Method II: PWM with Third-Order Harmonic Injected Voltage Reference

From Table 5-1, and for the PWM with third-order harmonic injected voltage reference, the minimum submodule capacitance is 1300 μF when the rated V/f =150 kV/50 Hz. On the other hand, the minimum submodule capacitance is 3600 μF when the rated V/f =102 kV/34 Hz. This observation also supports the MMC energy storage requirement(s) discussed in the preceding section.

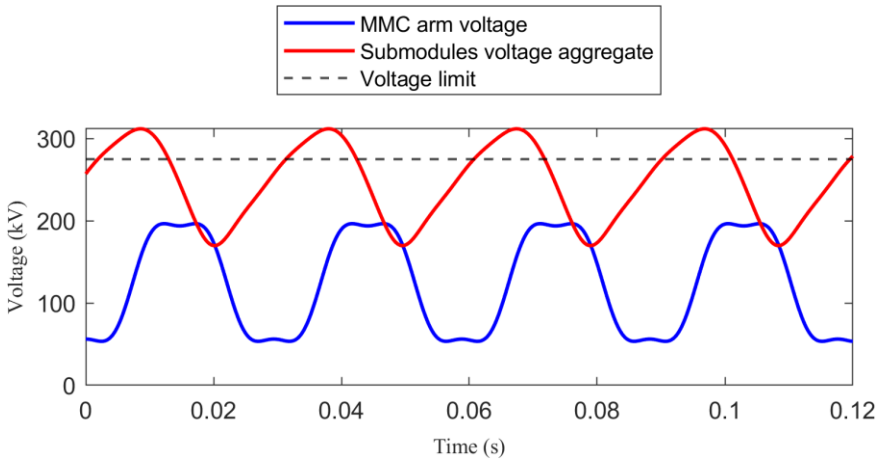

(a)

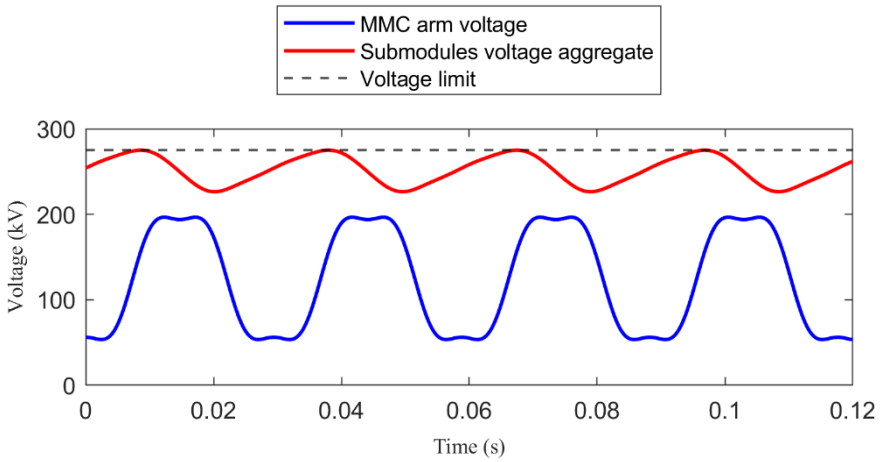

(b)

Fig. 5-5: Plots of the MMC upper arm voltage and the submodules voltage aggregate for the LF-HVac rated V/f pair (102 kV/34 Hz); (a): submodules capacitance = 1300 μF, (b): submodules capacitance = 3600 μF.

The voltage plots in Fig. 5-5 show that using the equivalent HVdc MMC designed submodule capacitance instead of the capacitance specifically designed for the V/f controlled LF-HVac MMC would result in dc overvoltage.

5.3.2. $0.8 \times P_{rated}$ Delivered to the Grid: MMC Energy Storage Evaluation

The preceding sub-section treated the design of the LF-HVac MMC for the system rated V and f. However, it is important to confirm that the required MMC energy storage for the selected lower V/f pairs during lower-than-rated-output-power wind conditions do not exceed the rated LF-HVac MMC energy storage capacity.

This section presents the energy storage evaluation of the rated LF-HVac MMC when $0.8 \times P_{rated}$ (120 MW) is delivered to the grid. In Chapter 4, V/f = 90 kV/30 Hz and V/f = 93 kV/31 Hz were considered suitable for this power output point. However, V/f = 93 kV/31 Hz was finally selected because less MMC energy storage would be required than if V/f = 90 kV/30 Hz was used. The plots in Fig. 5-6 confirm this assertion. They show that the submodules capacitor aggregate voltage peak for V/f = 90 kV/30 Hz exceeds the MMC dc voltage limit of 275 kV, while the peak for V/f = 93 kV/31 Hz does not exceed the dc voltage limit. Therefore, V/f = 93 kV/31 Hz was rightly selected in Chapter 4 for the delivery of $0.8 \times P_{rated}$ (120 MW) to the grid in the case study.

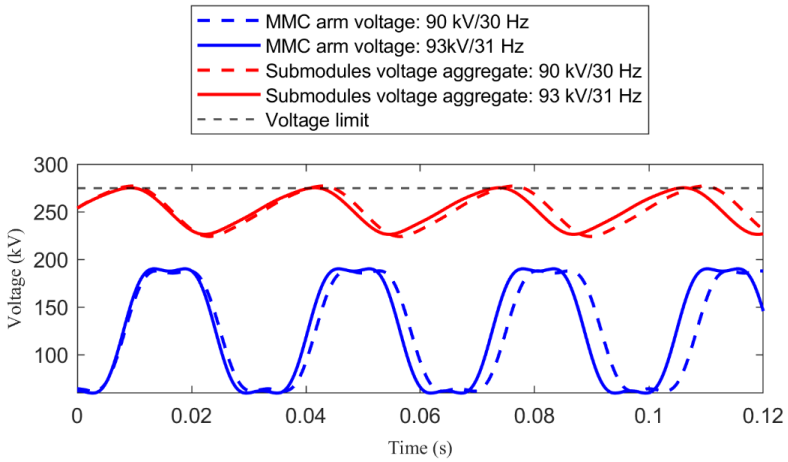

(a)

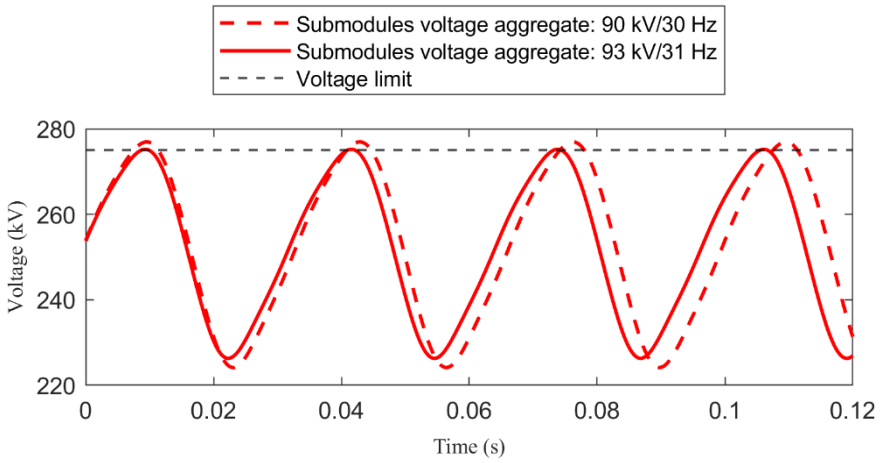

(b)

Fig. 5-6: Plots of the MMC upper arm voltage and the submodules voltage aggregate for V/f pairs: 90 kV/30 Hz and 93 kV/31 Hz; for the delivery of $0.8 \times P_{rated}$ to the grid.

5.3.3. $0.4 \times P_{rated}$ Delivered to the Grid: MMC Energy Storage Evaluation

This section presents the energy storage evaluation of the rated LF-HVac MMC when $0.4 \times P_{rated}$ (60 MW) is delivered to the grid. In Chapter 4, V/f = 72 kV/24 Hz was selected for this wind energy output level in the case study. The voltage plots in Fig. 5-7 confirm that V/f = 72 kV/24 Hz was rightly selected for this wind energy output level. The submodules voltage

aggregate peak does not exceed the dc voltage limit, and the MMC arm voltage peak is well below the submodules voltage aggregate trough.

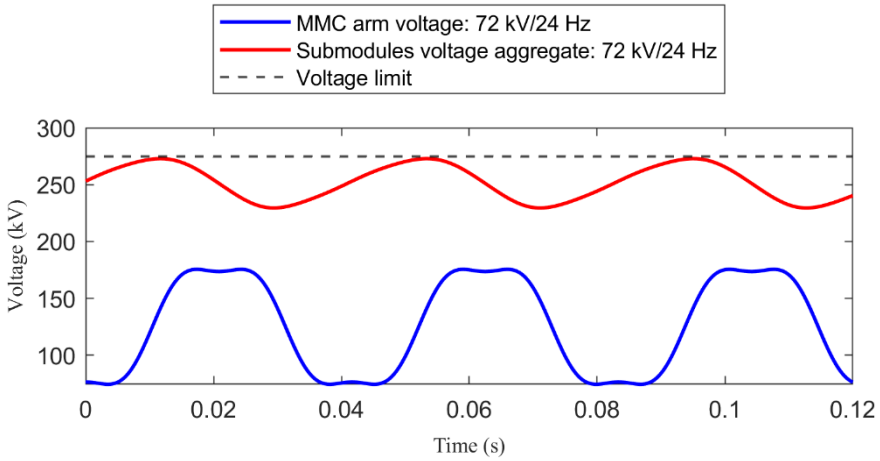

Fig. 5-7: Plots of the MMC upper arm voltage and the submodules voltage aggregate for V/f = 72 kV/24; for the delivery of $0.4 \times P_{rated}$ to the grid.

5.4. Summary

In this chapter, equations for the design of the LF-HVac MMC submodules capacitance and the evaluation of the MMC energy storage capacity were developed. The equations were then used to design the LF-HVac MMC for the case study introduced in Chapter 4.

Of the two PSC-PWM MMC output voltage synthesis methods, it was shown that the PWM with third-order harmonic injected voltage reference method would produce an MMC design with less energy storage requirement, which in turn requires smaller submodules capacitance than if PWM with sinusoidal voltage reference method was used. Finally, the case study results confirm the V/f pairs selected in Chapter 4 would operate within the energy storage capacity of the LF-HVac MMC designed for the case study.

Chapter 6

EMT Simulation and Validation of the V/f Controlled LF-HVac Transmission Scheme for Offshore Wind

6.1. Introduction

This chapter validates the proposed V/f controlled LF-HVac transmission scheme concept developed in Chapter 4 and Chapter 5. To do this, electromagnetic transient (EMT) simulation(s) of the detailed LF-HVac system model was implemented in PSCAD/EMTDC.

6.2. LF-HVac Transmission System Topology for Offshore Wind

Fig. 6-1 shows the system topology of the LF-HVac transmission scheme for the grid integration of offshore wind. It shows the OWPP, consisting of several wind turbines spread out

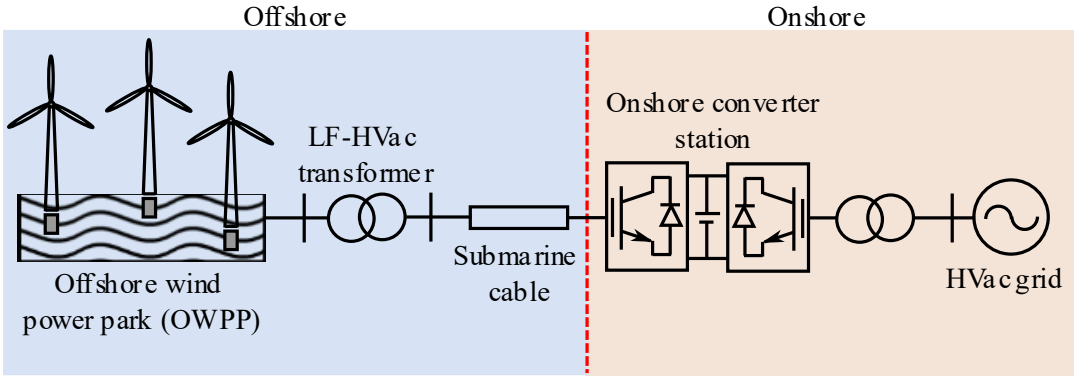

Fig. 6-1: LF-HVac transmission system topology for offshore wind.

over the area of the wind farm. The LF-HVac transformer is used to step up the OWPP collection system medium voltage (typically 33 kV) to the high voltage required for transmission. Other components include the submarine export cable(s), the onshore BtB-MMC converter station, and the power transformer, which is used for interconnection to the HVac grid.

The Onshore Converter Station in Fig. 6-1 is a BtB-MMC system. It consists of the rectifier MMC, which converts the LF-HVac power to dc intermediate power, and the inverter MMC, which converts the dc intermediate power to the grid frequency power. The main function of the rectifier MMC is to establish and to regulate the applicable LF-HVac system voltage and frequency. The inverter MMC is tasked mainly with the regulation of the dc-link voltage.

6.3. Case Study: EMT Validation

This section presents the EMT validation of the case study spanning Chapter 4 and Chapter 5. For brevity, only the results for the wind project configuration I, whose export cable length is 150 km, is presented. The system parameters are presented in Chapter 4 and Chapter 5.

6.3.1. EMT Simulation for P_{rated} (150 MW) Delivered to the Grid

Table 6-1 presents the power flow quantities in the wind project configuration I for the delivery of P_{rated} (150 MW) to the grid. It compares the results determined via the analytical method (treated in Chapter 4) and the EMT simulations. The reader can observe that the EMT results are approximately equal to the analytical results. Hence, this provides validation to the V/f controlled LF-HVac transmission scheme for offshore wind investigated in this thesis. Note that for active/reactive power determination, it is assumed that current flows into the applicable bus. Therefore, in Table 6-1, a negative sign indicates that the actual power flow is in the reverse

Table 6-1: Power flow quantities in the wind project configuration I for P_{rated} (150 MW) delivered to the grid; analytical results (Chapter 4) vs. EMT results comparison.

Quantity	Analytical results		EMT results	
	@ Grid POI	@ OWPP	@ Grid POI	@ OWPP
Active power (MW)	150.0	-160.3	149.9	-160.1
Reactive power (MVar)	0.00	49.59	-8.31	50.45
Power factor	1.0000	0.9553	0.9985	0.9540
Current (A)	849.04	914.98	850.62	921.24
Voltage (kV)	102.00	105.89	101.90	105.20
Efficiency (%)	93.57		93.69	

direction. For example, at the OWPP bus, the active power is negative, indicative of power flowing to the converter station, and eventually to the grid.

Fig. 6-2 presents the plots of the LF-HVac MMC upper/lower arm voltage and the submodules voltage aggregate for P_{rated} delivery to the grid, in the case study wind project configuration I. Note that the plots correspond to the LF-HVac system operation results presented in Table 6-1. It can be observed that the EMT results plots closely track those of the analytical results (treated in Chapter 5). Hence, this provides further validation to the V/f controlled LF-HVac transmission scheme for offshore wind investigated in this thesis.

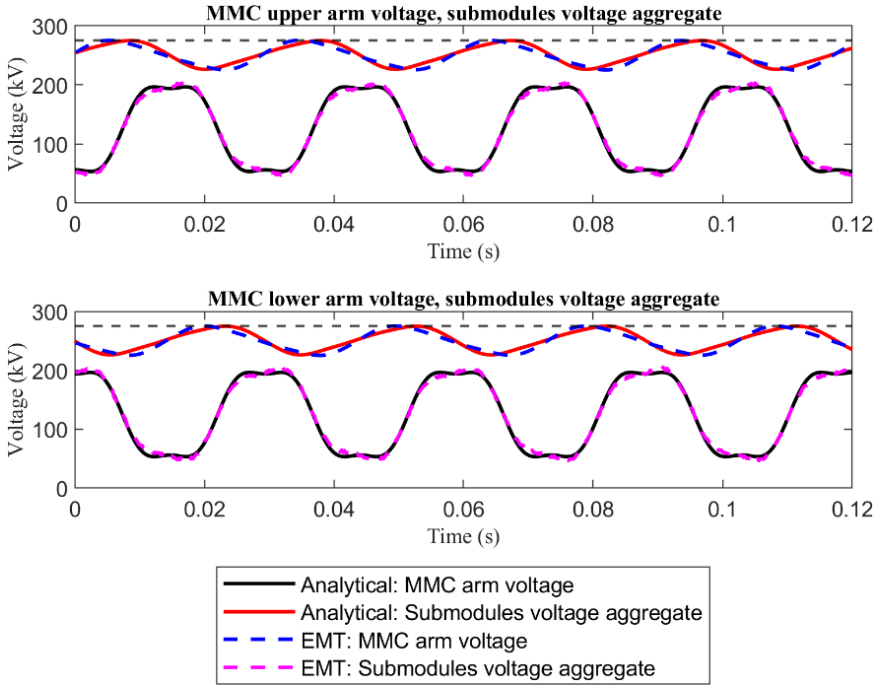

Fig. 6-2: Plots of the LF-HVac MMC upper/lower arm voltage and the submodules voltage aggregate for P_{rated} delivery to the grid, in the case study wind project configuration I.

6.3.2. EMT Simulation for Grid Delivered Power < P_{rated}

A good agreement between the results determined via EMT simulations and those determined analytically was also observed when the wind output falls below P_{rated}. As an example, the results for $0.4 \times P_{rated}$ (60 MW) delivered to the grid is hereby presented. Table 6-2 presents the power flow quantities in the wind project configuration I for the delivery of $0.4 \times P_{rated}$ (60 MW) to the grid. It compares the results determined via the analytical method (treated in Chapter 4) and the EMT simulations. The reader can observe that the EMT results are approximately equal to the analytical results. Hence, this provides further validation to the V/f controlled LF-HVac transmission scheme for offshore wind investigated in this thesis.

Table 6-2: Power flow quantities in the wind project configuration I for $0.4 \times P_{rated}$ (60 MW) delivered to the grid; analytical results (Chapter 4) vs. EMT results comparison.

Quantity	Analytical results		EMT results	
	@ Grid POI	@ OWPP	@ Grid POI	@ OWPP
Active power (MW)	60.0	-63.2	60.84	-63.93
Reactive power (MVar)	0.00	20.71	-1.36	19.56
Power factor	1.0000	0.9502	0.9998	0.9562
Current (A)	481.13	515.45	488.25	518.18
Voltage (kV)	72.00	74.48	71.96	74.49
Efficiency (%)	94.94		95.17	

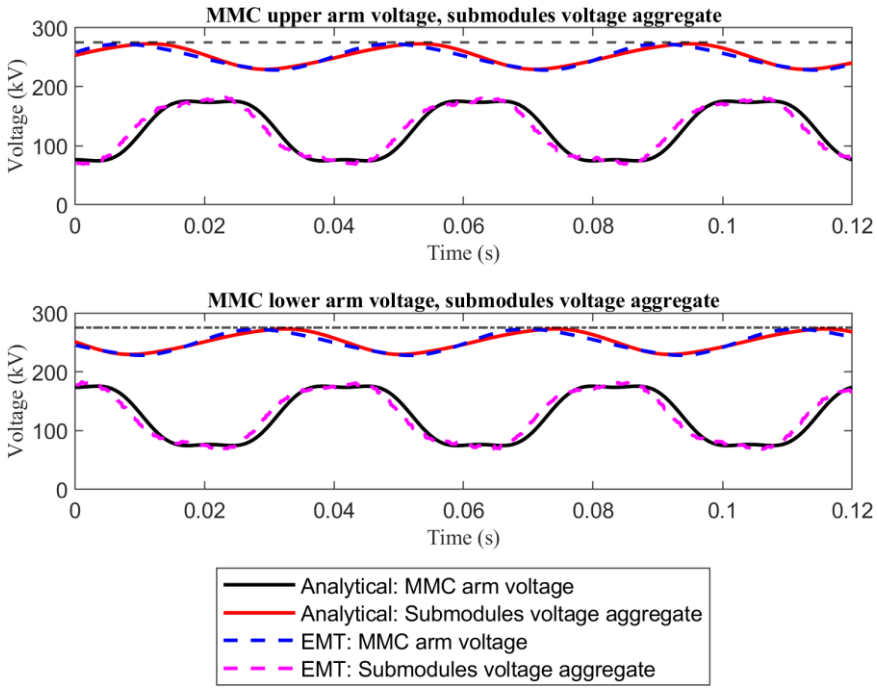

Fig. 6-3: Plots of the LF-HVac MMC upper/lower arm voltage and the submodules voltage aggregate for $0.4 \times P_{rated}$ delivery to the grid, in the case study wind project configuration I.

Fig. 6-3 presents the plots of the LF-HVac MMC upper/lower arm voltage and the submodules voltage aggregate for $0.4 \times P_{rated}$ delivery to the grid, in the case study wind project configuration I. Note that the plots correspond to the LF-HVac system operation results presented in Table 6-2. It can be observed that the EMT results plots closely track those of the analytical results (treated in Chapter 5). Hence, this provides further validation to the V/f controlled LF-HVac transmission scheme for offshore wind investigated in this thesis.

.

6.4. Summary

This chapter presented the results determined via the EMT simulation of the detailed system model of the V/f controlled LF-HVac transmission scheme for offshore wind in the PSCAD/EMTDC software. The results closely track those determined analytically in Chapter 4 and Chapter 5, thereby validating the thesis study proposal and investigations results. Therefore, it can be concluded that the V/f controlled LF-HVac transmission scheme for offshore wind developed in this thesis is technically feasible and is a good fit for offshore wind energy, even wind the intermittent nature of wind.

Chapter 7

Conclusions and Recommendations for Future Work

7.1. Thesis Contributions and Conclusions

In this thesis, a novel method for the grid integration of remote offshore wind farms has been proposed. The investigations on the technical feasibility and the fit of the V/f controlled LF-HVac transmission scheme for offshore wind energy have provided promising results in support of the proposed method. Therefore, the main contributions of this thesis are as follows:

1. V/f controlled LF-HVac transmission scheme for the grid integration of remote offshore wind is proposed. It is shown that the transmission scheme is technically feasible and is a good fit for offshore wind energy.
    a. Wind is an intermittent and non-dispatchable energy resource. Hence, it is important, as shown, that for each available energy output, the power transmission system can deliver most of that harnessed energy to the grid, by minimizing losses.
    b. It is shown that because of the relatively large capacitance of submarine cables, there is a large charging current which also flows through the line resistance, resulting in a substantial part of the wind energy dispatched into the cable system being lost. As also shown, charging current losses become more pronounced as the cable length increases, even to the point that no useful power would reach the destination station. For example, in

Chapter 4 it was shown that 100% of the 162 MW dispatched into the export cable, whose length is 200 km, operated at V/f = 150 kV/50 Hz was lost due to charging current losses just midway through the cable length.

c. It is shown that charging current is a function of the ac operating frequency f and the transmission voltage V. In the developed equation for the reactive power due to the charging current, it is observed that the exponent of V is twice that of f. Therefore, reducing V rather than f would be more effective in reducing the charging current losses. An even better strategy, as demonstrated, for the most reduction of charging current losses is to simultaneously reduce V and f.

d. As shown with the case study, the above strategy is especially useful during low wind energy output conditions. The combined reduction of V and f considerably minimizes the charging current losses in contrast to operating the LF-HVac system at a higher V/f set. Consequently, it is shown that more active power is delivered to the grid at the smaller V/f set than at a higher V/f set. Following up with the example given in b. above, for instance, when the same cable system was operated at V/f = 108 kV/36 Hz, 113 MW was delivered to the destination station.

2. From the previous studies on LF-HVac transmission, the consensus is that LF-HVac transformers and reactors would be larger and/or heavier than those used in the conventional HVac system. This is apparent from the transformer voltage equation, where it is observed that to reduce the ac frequency while maintaining

the rated voltage, either the number of turns and/or the core cross-sectional area must be increased for non-saturation operation of the transformer.

   a. However, unlike the earlier studies on LF-HVac where only the ac frequency was reduced, the V/f controlled LF-HVac method involves the simultaneous reduction of V and f in accordance with the applicable transformer/reactor rated V/f derating factor.
   b. Thus, it is shown that the V/f controlled LF-HVac method is amenable to the repurposing of commercially available 50 Hz rated transformers, reactors, cables, and other power equipment. This could significantly reduce upfront investment costs in the deployment of LF-HVac transmission for offshore wind.

3. As shown in the case study, the V/f controlled LF-HVac transmission method would inherently result in minimized offshore wind equipment and components. This assertion is with respect to applicable comparisons to an equivalent conventional HVac system or an equivalent LF-HVac system where only f is reduced.

   a. It is shown that as the wind power output falls below the rated power, V and f are reduced simultaneously. Consequently, less reactive power support (for voltage regulation) is needed at the export cable terminal(s). Therefore, with only minimal reactive power support needed, the V/f controlled LF-HVac system terminal equipment rating(s) can be reduced. For example, in the case study results presented in Chapter 6, the reactive power required at the offshore wind platform for the delivery of $0.4 \times$

P_{rated} (60 MW) to the grid is 20 MVar while 50 MVar is needed for the delivery of P_{rated} (150 MW) to the grid.

4. It is shown that the MMC energy storage capacity/requirement is inversely proportional to the ac system frequency. Thus, LF-HVac MMC must have larger submodules' capacitance to meet the higher energy storage requirement(s). For example, in the case study treated in Chapter 5, the minimum submodules capacitance of the rated LF-HVac MMC (at V/f = 102 kV/34 Hz) was determined to be 3600 μF. Contrast this to the minimum capacitance for an equivalent HVdc MMC (with ac system V/f = 150 kV/50 Hz) of 1300 μF. Thus, as implemented in the V/f control method, it may seem counter-intuitive to initiate further reduction of f below the rated value used to design the MMC.
    a. However, it is shown in the case study that the rated LF-HVac MMC can support the V/f controlled LF-HVac transmission scheme. The ac system frequency is reduced in accordance with the specified V/f derating factor. Note that the V/f control is applied proportionately to the available wind output power. Therefore, these factors counterbalance the supposed larger energy storage requirement(s) in the MMC when f is reduced.
5. It is shown that the electrical characteristics and performance of submarine export cables are considerably improved under LF-HVac operation than when operated under the conventional 50/60 Hz HVac system.
    a. It is shown that due to skin effect, the ac resistance of the cable would be significantly smaller under LF-HVac operation than under HVac operation. For example, in Chapter 3, the ac resistance of the 800 mm^2

three-core XLPE submarine cable used for case study increased by 4% over the dc resistance for operation at 20 Hz. On the other hand, the same cable ac resistance increased by 20% over the dc resistance for operation at 60 Hz. This difference even grows bigger as the cross-sectional area of the conductor becomes larger, as shown in Chapter 3.

b. Furthermore, it is shown that skin effect contribution to the value of the ac resistance is independent of the cable temperature.

c. Consequently, it is shown that the current carrying capacity, and thus, the power transfer capacity, of the export cable at LF-HVac operation would be higher than for operation at the conventional HVac.

d. It is also shown that the overall transmission losses in the export cable are reduced considerably for operation at LF-HVac when compared to its operation at HVac, even though significantly more power is being transferred under LF-HVac operation than for operation at HVac.

The outcomes of this work have been presented in two conference papers (listed below) and a transactions paper is in the works.

- O. Efobi, W. Li, M. Das and A. Gole, "Frequency-dependent electrical characteristics of submarine cables in low frequency high voltage ac (LF-HVac) transmission for offshore wind," *2023 IEEE PES General Meeting*, Orlando, USA, July 2023.
- O. Efobi, W. Li, A. Gole and M. Das, "Modeling and step response analysis of back-to-back VSC for LFAC transmission," *2019 IEEE Electrical Power and Energy Conference (EPEC)*, Montreal, Canada, November 2019.

7.2. Recommendations for Future Work

The following are recommendations for potential future work and the extension of the research presented in this thesis:

1. Extension of the V/f controlled LF-HVac transmission scheme from the point-to-point configuration investigated in this thesis to the hub-and-spoke configuration(s). Beyond the point-to-point configuration covered in this thesis, the feasibility, the fit, and the merits of V/f controlled LF-HVac transmission scheme in hub-and-spoke interconnected wind farms, and connecting to different frequency grids should be investigated.
2. Comprehensive system stability study of the V/f controlled LF-HVac transmission scheme during transitions from one V/f parameters set to another, as the wind output changes.

Appendix A

Formulae for Determining Bessel Functions M_0, M_1, θ_0, and θ_1 [70], [83]

$$M_0(ma) = \sqrt{\left(U_0(ma)\right)^2 + \left(V_0(ma)\right)^2} \tag{A-1}$$

$$M_1(ma) = \sqrt{\left(U_1(ma)\right)^2 + \left(V_1(ma)\right)^2} \tag{A-2}$$

$$\theta_0 = -\tan^{-1}\left(\frac{V_0(ma)}{U_0(ma)}\right) \tag{A-3}$$

$$\theta_1 = \pi - \tan^{-1}\left(\frac{V_1(ma)}{U_1(ma)}\right) \tag{A-4}$$

Where $U_0(ma)$, $V_0(ma)$, $U_1(ma)$, and $V_1(ma)$ are given by the following formulae, where $\phi = \frac{\pi}{4}$.

$$U_0(ma) = \sum_{k=0}^{\infty}(-1)^k \frac{\left(\frac{ma}{2}\right)^{2k}}{(k!)^2}\cos(2k\phi) \tag{A-5}$$

$$V_0(ma) = \sum_{k=0}^{\infty}(-1)^k \frac{\left(\frac{ma}{2}\right)^{2k}}{(k!)^2}\sin(2k\phi) \tag{A-6}$$

$$U_1(ma) = -\frac{\partial}{\partial(ma)}\left(U_0(ma)\cos\phi + V_0(ma)\sin\phi\right) \tag{A-7}$$

$$V_1(ma) = \frac{\partial}{\partial(ma)}\left(U_0(ma)\sin\phi - V_0(ma)\cos\phi\right) \tag{A-8}$$

Appendix B

Formulae Used in the Calculations for Current Rating of Three-Core Cables [73], [74], [75]

G: Geometric factor for three-core cables with separate sheaths

Table B-1: Definitions for G.

Symbol	Definition	Unit
$\boldsymbol{G_{E1}}$	$\boldsymbol{G = G_{E1}}$, **for when** $\boldsymbol{0 < X_G \leq 0.03}$	**N/A**
$\boldsymbol{G_{E2}}$	$\boldsymbol{G = G_{E2}}$, **for when** $\boldsymbol{0.03 < X_G \leq 0.15}$	**N/A**
X_G	Factor for calculating G	N/A
t_{sh-ar}	Total thickness between separate sheath and armour	mm
d_s	Diameter over sheath	mm
ρ_{sv}	Thermal resistivity of outer serving or jacket of cable	K.m/W
ρ_{sb}	Thermal resistivity of seabed or soil	K.m/W
L	Burial depth of cable	mm

$$X_G = \frac{t_{sh-ar}}{d_s} \tag{B-1}$$

$$G_{E1} = 2\pi(0.00020238 + 2.03214 \cdot X_G - 21.6667 \cdot X_G^2) \tag{B-2}$$

$$G_{E2} = 2\pi\left(0.0126529 + 1.101 \cdot X_G - 4.56104 \cdot X_G^2 + 11.5093 \cdot X_G^3\right) \tag{B-3}$$

I_c: Static Current Rating of a Power Cable, at 100% Load Factor

Table B-2: Definitions for I_c.

Symbol	Definition	Unit
θ_c	Conductor temperature at 90℃	℃
θ_{amb}	Ambient temperature of cable surroundings	℃
C	Cable capacitance	F/m
V_0	Operating phase-to-phase voltage of the system	V
$\tan\delta$	Loss factor of insulation XLPE 0.001 (U_n > 30 kV) 0.004 ($U_n \leq$ 30 kV)	N/A
U_n	Rated line-to-line voltage	kV
λ_{11}	Loss factor of shield by circulating currents [$\lambda_{11} = 0$ for single-point/cross-bonded sheaths]	N/A
λ_{12}	Loss factor of shield by eddy currents	N/A
R_{eqv}	Equivalent electrical resistance of shield and armour	Ω/m
c	Axial distance between conductors	mm
d_{eqv}	Equivalent diameter of screen/sheath and armour	mm
d_{sh-sc}	Equivalent diameter of screen and sheath	mm
R_{sh}	Electrical resistance of shield	Ω/m
R_{ar}	Electrical resistance of armour	Ω/m
c_c	Distance between a conductor axis and the cable centre	mm

$$\Delta T = \theta_c - \theta_{amb} \tag{B-4}$$

$$W_d = \frac{1}{3}\omega C V_0^2 \tan\delta \tag{B-5}$$

$$\lambda_1 = \lambda_{11} + \lambda_{12} \tag{B-6}$$

$$\lambda_{12} = \frac{3.2\omega^2}{R_{ac}R_{eqv}}\left(\frac{2c}{\sqrt{3}d_{eqv}}\right)^2 \times 10^{-14} \tag{B-7}$$

$$d_{eqv} = \frac{d_{sh-sc}}{2} + \frac{d_a}{2} \tag{B-8}$$

$$R_{eqv} = \frac{R_{sh}R_{ar}}{R_{sh} + R_{ar}} \tag{B-9}$$

$$\lambda_2 = \frac{1.23R_{ar}}{R_{ac}}\left(\frac{2c_c}{d_a}\right)^2\left(\left(\frac{2.77R_{ar} \times 10^6}{\omega}\right)^2 + 1\right)^{-1} \tag{B-10}$$

References

[1] International Electrotechnical Commission (IEC), "World Plugs," IEC, [Online]. Available: https://www.iec.ch/world-plugs. [Accessed 8 November 2024].

[2] P. Mixon, "Technical origins of 60 Hz as the standard AC frequency in North America," *IEEE Power Engineering Review,* vol. 19, no. 3, pp. 35-37, 1999.

[3] E. L. Owen, "The origins of 60-Hz as a power frequency," *IEEE Industry Applications Magazine,* vol. 3, no. 6, pp. 8-14, 1997.

[4] A. Lantero, "The War of the Currents: AC vs. DC Power," US Department of Energy, 18 November 2014. [Online]. Available: https://www.energy.gov/articles/war-currents-ac-vs-dc-power. [Accessed 8 November 2024].

[5] J. Grainger and W. Stevenson , Power System Analysis, Singapore: McGraw Hill Education, 1994.

[6] H. Ito, Switching Equipment, Springer International Publishing AG, 2018.

[7] H. N. Scherer and G. S. Vassell, "Transmission of electric power at ultra-high voltages: Current status and future prospects," *Proceedings of the IEEE,* vol. 73, no. 8, pp. 1252-1278, 1985.

[8] P. Kundur, Power System Stability and Control, Chennai: McGraw Hill Education (India) Private Limited, 1994.

[9] H. Saadat, Power System Analysis, New York: McGraw Hill , 1999.

[10] A. Gole, *ECE 7990. Class Lecture, Topic: "HVDC Converters.",* Winnipeg, Manitoba : Department of Electrical and Computer Engineering, University of Manitoba , 2017.

[11] R. Perveen, N. Kishor and R. Mohanty , "Off-shore wind farm development: Present status and challenges," *Renewable and Sustainable Energy Reviews,* vol. 29, pp. 780-792, 2014.

[12] H. Chen , M. H. Johnson and D. C. Aliprantis, "Low-Frequency AC transmission for offshore wind power," *IEEE Transactions on Power Delivery,* vol. 28, no. 4, pp. 2236-2244, 2013.

[13] S. V. Bozhko, R. Blasco-Gimenez, R. Li, J. C. Clare and G. M. Asher , "Control of offshore DFIG-based wind farm grid with line-commutated HVDC connection," *IEEE Transactions on Energy Conversion,* vol. 22, no. 1, pp. 71-78, 2007.

[14] J. Arrillaga, High Voltage Direct Current Transmission, London: Peter Peregrinus Ltd, 1983.

[15] International Renewable Energy Agency (IRENA), "Wind Energy," IRENA, [Online]. Available: https://www.irena.org/wind. [Accessed 8 November 2024].

[16] International Energy Agency (IEA), "Renewables 2023: Analysis and Forecast to 2028," IEA, 2024.

[17] American Geosciences Institute (AGI), "What are the advantages and disadvantages of offshore wind farms?," AGI, [Online]. Available: https://www.americangeosciences.org/critical-issues/faq/what-are-advantages-and-disadvantages-offshore-wind-farms. [Accessed 8 November 2024].

[18] J. Ruddy, "Low Frequency AC Transmission for the Integration of Offshore Wind," PhD thesis, University College Dublin, Dublin, Ireland, 2017.

[19] International Energy Agency (IEA), "Offshore Wind Outlook 2019," IEA, 2019.

[20] W. Fischer, R. Braun and I. Erlich, "Low frequency high voltage offshore grid for transmission of renewable power," in *2012 3rd IEEE PES Innovative Smart Grid Technologies Europe (ISGT Europe), 2012*, Berlin,

2012.

[21] Y. Cho, G. J. Cokkinides and A. P. Meliopoulos, "LFAC-transmission systems for remote wind farms using a three-phase, six-pulse cycloconverter," in *2012 IEEE Power Electronics and Machines in Wind Applications*, Denver, USA, 2012.

[22] I. Erlich, F. Shewarega, H. Wrede and W. Fischer, "Low frequency AC for offshore wind power transmission - prospects and challenges," in *11th IET International Conference on AC and DC Power Transmission*, 2015.

[23] N. Qin, S. You, Z. Xu and V. Akhmatov, "Offshore wind farm connection with low frequency AC transmission technology," in *2009 IEEE Power & Energy Society General Meeting*, Calgary, Canada, 2009.

[24] E. Olsen, U. Axelsson and A. Canelhas, "Low Frequency AC Transmission on Large Scale Offshore Wind Power Plants, Achieiving the best from two worlds?," in *13th Wind Integration Workshop*, Berlin, 2014.

[25] J. Laury, "Stability of Low-Frequency AC Railways: Models and Transient Stability," PhD thesis, Lulea University of Technology, Lulea, Sweden, 2019.

[26] United Nations (UN) Climate Change , "The Paris Agreement," UN Climate Change, [Online]. Available: https://unfccc.int/process-and-meetings/the-paris-agreement. [Accessed 8 November 2024].

[27] X. Wang and X. Wang , "Feasibility study of fractional frequency transmission system," *IEEE Transactions on Power Systems,* vol. 11, no. 2, pp. 962-967, 1996.

[28] T. Funaki and K. Matsuura, "Feasibility of the low frequency AC transmission," in *2000 IEEE Power Engineering Society Winter Meeting. Conference Proceedings*, Singapore, 2000.

[29] X. Wang , C. Cao and Z. Zhou , "Experiment on fractional frequency transmission system," *IEEE Transactions on Power Systems,* vol. 21, no. 1, pp. 372-377, 2006.

[30] T. Ngo, M. Lwin and S. Santoso, "Steady-State Analysis and Performance of Low Frequency AC Transmission Lines," *IEEE Transactions on Power Systems,* vol. 31, no. 5, pp. 3873-3880, 2016.

[31] B. Gustavsen and O. Mo, "Variable Transmission Voltage for Loss Minimization in Long Offshore Wind Farm AC Export Cables," *IEEE Transactions on Power Delivery,* vol. 32, no. 3, pp. 1422-1431, 2017.

[32] Q. Nguyen and S. Santoso, "Optimal Planning and Operation of Multi-Frequency HVac Transmission Systems," *IEEE Transactions on Power Systems,* vol. 36, no. 1, pp. 689-698, 2021.

[33] ABB Technical Staff, "XLPE Submarine Cable System Attachment to XLPE Land Cable Systems - User´s Guide," ABB.

[34] K. C. Randall, "Oil Circuit Breakers," *Transactions of the American Institute of Electrical Engineers,* vol. XXXIV, no. 1, pp. 247-268, 1915.

[35] D. Van Hertem and M. Ghandhari, "Multi-terminal VSC HVDC for the European supergrid: Obstacles," *Renewable and Sustainable Energy Reviews,* vol. 14, no. 9, pp. 3156-3163, 2010.

[36] N. Flourentzou, V. G. Agelidis and G. D. Demetriades, "VSC-Based HVDC Power Transmission Systems: An Overview," *IEEE Transactions on Power Electronics,* vol. 24, no. 3, pp. 592-602, 2009.

[37] C. M. Franck, "HVDC Circuit Breakers: A Review Identifying Future Research Needs," *IEEE Transactions on Power Delivery,* vol. 26, no. 2, pp. 998-1007, 2011.

[38] H. Wei and X. Pang, "Research on Key Technology and Equipment for Zhangbei 500kV DC Grid," in *2018 International Power Electronics Conference*, Niigata, 2018.

[39] Z. Lin, J. Qin, H. Ma, J. Liu, B. Yang and Y. Wang , "Design of 500kV Hybrid HVDC Circuit Breaker Control and Protection System," in *2020 4th International Conference on HVDC (HVDC)*, Xi'an, China, 2020.

[40] ABB, "ABB enables world's first HVDC grid in China," ABB, 13 November 2018. [Online]. Available: https://new.abb.com/news/detail/10464/abb-enables-worlds-first-hvdc-grid-in-china. [Accessed 8 November 2024].

[41] W. Fischer, R. Braun and I. Erlich, "Low frequency high voltage offshore grid for transmission of renewable power," in *2012 3rd IEEE PES Innovative Smart Grid Technologies Europe (ISGT Europe)*, Berlin, 2012.

[42] Canada Energy Regulator, "Canada's Adoption of Renewable Power Sources – Energy Market Analysis," Government of Canada, Canada Energy Regulator, [Online]. Available: https://www.cer-rec.gc.ca/en/data-analysis/energy-commodities/electricity/report/archive/2017-canadian-adoption-renewable-power/canadas-adoption-renewable-power-sources-energy-market-analysis-emerging-technologies.html. [Accessed 12 November 2024].

[43] European Commission, "Offshore Renewable Energy," European Commission, [Online]. Available: https://energy.ec.europa.eu/topics/renewable-energy/offshore-renewable-energy_en#offshore-wind-energy. [Accessed 12 November 2024].

[44] WindEurope, "Offshore Wind in Europe – Key Trends and Statistics 2020," WindEurope, 2021.

[45] Global Wind Energy Energy Council, "Global Wind Report 2021," Global Wind Energy Energy Council, 2021.

[46] Orsted, "Operations start on Hornsea One, the world's largest offshore wind farm," Orsted, 2 June 2019. [Online]. Available: https://orsted.co.uk/media/newsroom/news/2019/05/operations-start-on-hornsea-one. [Accessed 8 November 2024].

[47] Orsted, "Hornsea 2 Powering well over 1.4 million homes with green electricity," Orsted, London, 2022.

[48] Smart Wind , "Hornsea Project One: Environmental Impact Assessment Scoping Report," 2010.

[49] H. Chen, M. H. Johnson and D. C. Aliprantis, "Low-Frequency AC transmission for offshore wind power," *IEEE Transactions on Power Delivery,* vol. 28, no. 4, pp. 2236-2244, 2013.

[50] J. Ma, M. Dahidah and V. Pickert, "Modular multilevel matrix converter for offshore low frequency AC transmission system," in *2017 IEEE 26th International Symposium on Industrial Electronics (ISIE)*, Edinburgh, UK, 2017.

[51] Y. Miura, T. Mizutani, M. Ito and T. Ise, "Modular multilevel matrix converter for low frequency AC transmission," in *2013 IEEE 10th International Conference on Power Electronics and Drive Systems (PEDS)*, Kitakyushu, Japan, 2013.

[52] J. Ruddy, R. Meere and T. O'Donnell, "Low Frequency AC transmission as an alternative to VSC-HVDC for grid interconnection of offshore wind," in *2015 IEEE Eindhoven PowerTech*, Eindhoven, 2015.

[53] J. Ruddy, R. Meere, C. O'Loughlin and T. O'Donnell, "Design of VSC Connected Low Frequency AC Offshore Transmission With Long HVAC Cables," *IEEE Transactions on Power Delivery,* vol. 33, no. 2, pp. 960-970, 2018.

[54] Y. Tang, P. B. Wyllie and J. Yu, "Offshore low frequency AC transmission with back-to-back modular multilevel converter (MMC)," in *11th IET International Conference on AC and DC Power Transmission*, Birmingham, UK, 2015.

[55] B. K. Bose, Modern Power Electronics and AC Drives, Upper Saddle River, NJ: Prentice Hall PTR, 2002.

[56] G. Asplund, K. Eriksson and K. Svensson, "DC Transmission based on Voltage Source Converters," in *CIGRE SC14 Colloquium in South Africa 1997*, 1997.

[57] G. Andersson and M. Hyttinen, "HVDC and Power Electronic Technology System Development and Economics," in *CIGRE*, Lund, Sweden, 2015.

[58] ENTSO-E, "Technologies for Transmission System," ENTSO-E, 2019.

[59] Toshiba Energy Systems & Solutions Corporation, "New East-West HVDC Commissioned, Interconnecting Nagano and Gifu Prefectures," Toshiba Energy Systems & Solutions Corporation, 1 April 2021. [Online]. Available: https://www.global.toshiba/ww/news/energy/2021/04/news-20210401-01.html. [Accessed 12 November 2024].

[60] A. Yazdani and R. Iravani, Voltage-Sourced Converters in Power Systems Modelling, Control, and Applications, Hoboken, New Jersey: John Wiley & Sons, Inc. , 2010.

[61] K. Sharifabadi, Design, Control, and Application of Modular Multilevel Converters for HVdc Transmission Systems, West Sussex, UK : John Wiley & Sons , 2016.

[62] Y. Meng, S. Yan and K. Wu, "Comparative economic analysis of low frequency AC transmission system for the integration of large offshore wind farms," *Renewable Energy ,* vol. 179, pp. 1955-1968, 2021.

[63] S. Du, A. Dekka and B. Wu, Modular Multilevel Converters Analysis, Control, and Applications, Hoboken, New Jersey: John Wiley & Sons Inc., 2018.

[64] U. N. Gnanarathna, "Efficient Modeling of Modular Multilevel HVDC Converters (MMC) on Electromagnetic Transient Simulation Programs," PhD thesis, University of Manitoba, Winnipeg,MB, 2014.

[65] U. N. Gnanarathna, "Efficient Modeling of Modular Multilevel HVDC Converters (MMC) on Electromagnetic Transient Simulation Programs," PhD thesis, University of Manitoba, Winnipeg, 2014.

[66] S. V. Khaparde and S. A. Kulkarni, Transformer Engineering Design and Practice, New York: Marcel Dekker, Inc., 2004.

[67] R. Meere, J. Ruddy and . P. McNamara, "Variable AC transmission frequencies for offshore wind farm interconnection," *Renewable Energy,* vol. 103, pp. 321-332, 2017.

[68] P. B. Wyllie, Y. Tang, L. Ran, T. Yang and J. Yu, "Low Frequency AC Transmission - Elements of a Design for Wind Farm Connection," in *11th IET International Conference on AC and DC Power Transmission*, 2015.

[69] M. R. Islam, Y. Guo and J. Zhu, "A review of offshore wind turbine nacelle: Technical challenges, and research and developmental trends," *Renewable and Sustainable Energy Reviews,* vol. 33, pp. 161-176, 2014.

[70] J. Zaborszky and J. W. Rittenhouse , Electric Power Transmission The Power System in the Steady State, New York : The Ronald Press Company , 1954.

[71] D. N. Kossyvakis, A. I. Chrysochos and K. Pavlou, "Calculation of losses in three-core submarine cables for fractional frequency transmission operation," in *2018 IEEE International Conference on High Voltage Engineering and Application (ICHVE)*, Athens, Greece, 2018.

[72] M. A. Gonzalez-Cagigal , J. C. del-Pino-Lopez and A. Bachiller-Soler, "A thermal model for three-core armored submarine cables based on distributed temperature sensing," *Energies,* vol. 14, no. 3897, pp. 1-19, 2021.

[73] T. V. M. Nielsen, S. Jakobsen and M. Savaghebi, "Dynamic rating of three-core XLPE submarine cables considering the impact of renewable power generation," in *2019 IEEE 13th International Conference on Compatibility, Power Electronics and Power Engineering (CPE-POWERENG)*, Sonderborg, Denmark, 2019.

[74] *60287-1-1 Electric Cables-Calculation of the Current Rating-Part 1-1: Current Rating Equations (100 % Load Factor) and Calculation of Losses-General,* Geneva, Switzerland: IEC Standard, 2015.

[75] Cableizer, "Documentation," Cableizer, [Online]. Available: https://www.cableizer.com/documentation/. [Accessed 12 November 2024].

[76] C. Huang , F. Li and Z. Jin, "Maximum power point tracking strategy for large-scale wind generation systems considering wind turbine dynamics," *IEEE Transactions on Industrial Electronics,* vol. 62, pp. 2530-2539, 2015.

[77] S. Senroy and N. Ghosh, "Electromechanical Dynamics of Controlled Variable-Speed Wind Turbines," *IEEE Systems Journal,* vol. 9, no. 2, pp. 639-646, 2015.

[78] Siemens Gamesa , "Scaling up the use of offshore wind turbines," [Online]. Available: https://www.siemensgamesa.com/global/en/home/products-and-services/offshore.html. [Accessed 12 November 2024].

[79] US Office of Energy Efficiency & Renewable Energy , "How do wind turbines survive severe storms?," US Office of Energy Efficiency & Renewable Energy , 20 June 2017. [Online]. Available: https://www.energy.gov/eere/articles/how-do-wind-turbines-survive-severe-storms#:~:text=The%20cut%2Din%20speed%20(typically,its%20maximum%2C%20or%20rated%20power.. [Accessed 03 March 2023].

[80] M. H. El-Saadany and E. F. Albadi , "Wind Turbine Capacity Factor Modeling - A Novel Approach," *IEEE Transactions on Power Systems,* vol. 24, no. 3, pp. 1637-1638, 2009.

[81] Z. Guiping , D. Xiaowei and Z. Chen , "Optimisation of reactive power compensation of HVAC cable in off-shore wind power plant," *IET Journals ,* vol. 9, no. 7, pp. 857-863, 2015.

[82] K. Ilves , S. Norrga, L. Harnefors and H.-P. Nee , "On Energy Storage Requirements in Modular Multilevel Converters," *IEEE Transactiions on Power Electronics ,* vol. 29, no. 1, pp. 77-88, 2014.

[83] Mathematical Tables Project Work Projects Administration of the Federal Works Agency , The Bessel Functions J_0(z) and J_1(z) for Complex Arguments, New York : Columbia University Press , 1943.